# INVESTIGATION OF PHOSPHATIDYLINOSITOLS AND PHOSPHOINOSITIDES USING MATRIX-ASSISTED LASER DESORPTION/IONIZATION MASS SPECTROMETRY IMAGING

LAURENTIU G. DABIJA

A THESIS SUBMITTED TO
THE FACULTY OF GRADUATE STUDIES
IN PARTIAL FULFILLMENT OF THE
REQUIREMENTS
FOR THE DEGREE OF
MASTERS IN SCIENCE

GRADUATE PROGRAM IN CHEMISTRY
YORK UNIVERSITY
TORONTO, ONTARIO

January 2025

# Abstract

Matrix-assisted laser desorption/ionization mass spectrometry imaging (MALDI-MSI) is a powerful analytical technique that captures the spatial distribution of biomolecules directly from tissue surfaces. Widely used in lipidomics, MALDI-MSI provides label-free, high-resolution imaging of lipid species in situ, making it invaluable for studying lipid dynamics in health and disease. This thesis focuses on phosphatidylinositols (PIs) and their phosphorylated forms, phosphoinositides (PIPs), which are critical regulators of cellular signaling, membrane dynamics, and cytoskeletal organization. Dysregulation of PIs and PIPs are implicated in various diseases, including atypical hemolytic uremic syndrome (aHUS), necessitating a deeper understanding of their spatial distribution and abundance.

Given the low concentration of PIs and PIPs, the study aimed to optimize MALDI-MSI for their detection. Thus, various chemical matrices necessary for the desorption and subsequent ionization processes in MALDI, were systematically evaluated to enhance the ionization and improve the detectability of these species, identifying 2,5-dihydroxyacetophenone and 1,5-diaminonaphthalene as optimal matrices. Additionally, we explored the limitation of MALDI-MS, specifically investigating the in-source fragmentation (ISF) of phosphatidylinositol triphosphate using the survival yield method, confirming that ISF occurs within the high energy conditions of MALDI.

# Acknowledgements

Firstly, I would like to express my sincere gratitude to my supervisor, Professor Demian R. Ifa, for opening up the world of mass spectrometry imaging to me. Prof. Ifa played a pivotal role in my research and provided mentorship throughout my academic graduate career. The time I spent here in his lab, has contributed to both personal growth and deep passion for research. Despite my struggles during my undergraduate journey, Prof. Ifa made me feel instantly at home in his group. Since then, I have been exposed to new scientific concepts, techniques, and learned how to think creatively. Most importantly, these last two years have taught me that no matter the struggles or challenges I encounter, whether it is with experiments or understanding scientific concepts, to always remain persistent in my work. Without Prof. Ifa's guidance, I truly would not be where I am today. My aspirations and ambitions for research have been shaped from him and the work conducted in his lab. I hope to continue and advance my academic journey. Thank you for your guidance.

In addition, I would like to extend my gratitude to my committee members, Professors Derek Wilson and Philip Johnson, who have provided valuable feedback and suggestions during the annual research evaluations. Both have played important roles in shaping my research and improving the quality of my work. Also, I would like to thank the past and current members of Prof. Ifa's lab: Maryam, Karl, and Leonardo. I have truly had the privilege to work with each and every one of you. Working alongside all of you has really fueled my passion for research. The countless discussions, brainstorming, laughter, and creative experiments we performed, will be something I will never forget. Thank you all for your friendship and support.

Finally, to my family and friends. To both my parents, Marius and Marinela Dabija, who have always supported my dreams. Throughout my ups and downs, they have always provided me with their love and support. Without their guidance, I would not be where I am today. I would like to give a special thanks to my mother, who, ever since I was a child, showed me the true beauty of our world through a scientific lens. My mother has been a role model in shaping my passion and, ultimately, my career. I love you both.

And to my friends, for supporting me throughout this journey. I am especially thankful for their understanding and patience in my absence from social events.

# Table of Contents

# List of Tables

# List of Figures

# List of Abbreviations

API - Atmospheric Pressure Ionization

aHUS - atypical Hemolytic Uremic Syndrome

BOEC - Blood Outgrowth Endothelial Cells

CID - Collision-Induced Dissociation

CMBT - 5-chloro-2-mercaptobenzothiazole

DAG – Diacylglycerol

DESI - Desorption Electrospray Ionization

DHA - 2,5-dihydroxyacetophenone

DGK - Diacylglycerol Kinase

DGKε - Diacylglycerol kinase epsilon

EP - Elevated Pressure

ESI - Electrospray Ionization

FA - Fatty Acyl

GL - Glycolipids

GP – Glycerophospholipids

HCD - Higher Energy Collision Dissociation

HUS - Hemolytic Uremic Syndrome

HPF - High-Pressure Funnel

iHUVEC - Immortalized Human Umbilical Vein Endothelial Cells

ITO - Indium Tin Oxide

IP – Inositol Phosphate

KO - Knockout (Genetically Engineered)

LC-MS - Liquid Chromatography-Mass Spectrometry

LPF - Low-Pressure Funnel

MALDI - Matrix-Assisted Laser Desorption/Ionization

MALDI-TOF - Matrix-Assisted Laser Desorption/Ionization Time-of-Flight

MS - Mass Spectrometry

MSI - Mass Spectrometry Imaging

MS/MS - Tandem Mass Spectrometry

MW - Molecular Weight

ND:YLF- Neodymium-doped Yttrium Lithium Fluoride

NRM – Norharmane

PAs - Phosphatidic Acids

PIs - Phosphatidylinositols

PIPs – Phosphoinositides

PI3P - Phosphatidylinositol-3-Phosphate

PI4P - Phosphatidylinositol-4-Phosphate

PI5P - Phosphatidylinositol-5-Phosphate

PI(4,5)P2 - Phosphatidylinositol-4,5-Bisphosphate

PI(3,5)P2 - Phosphatidylinositol-3,5-Bisphosphate

PI(3,4)P2 - Phosphatidylinositol-3,4-Bisphosphate

PI(3,4,5)P3 - Phosphatidylinositol-3,4,5-Trisphosphate

PIP- Phosphatidylinositol Phosphate

PIP2- Phosphatidylinositol Biphosphate

PIP3- Phosphatidylinositol Triphosphate

PLC - Phospholipase C

PK - Polyketides

PR - Prenol Lipids

S/N - Signal-to-Noise Ratio

SL - Saccharolipids

SP - Sphingolipids

ST - Sterol Lipids

SY - Survival Yield

TMA - Thrombotic Microangiopathy

WT - Wild Type (Non-Genetically Engineered)

9AA – 9-aminoacridine

# Chapter One: General Introduction

## 1.1 History and Principles of Mass Spectrometry

The origins of mass spectrometry (MS) date back to the late 19$^{th}$ century, during the hunt for the electron. [1] In 1897, J.J. Thomson conducted the first experiments and was often credited for the birth of MS. [2] Shortly after, in 1898, Wilhelm Wien had a comparable breakthrough while investigating positive anode rays, using electric and magnetic fields to separate ions based on their mass-to-charge ratios. Furthermore, Thomson, alongside his student Francis Aston, developed the first prototype of what is currently referred to as a mass spectrometer. They employed gas discharge tubes to generate ions and direct them through electric and magnetic fields, whereby the outcomes were recorded on photographic plates. [1][2] Within the next two decades, renowned physicists such as Dempster, Bainbridge, and Nier, made significant contributions to the field of MS, eventually leading to the discovery of new isotopes and achieving accurate mass measurements. [3] By the 1940s, mass spectrometry had emerged as a vital tool, significantly contributing to the Manhattan Project by facilitating the separation of the $^{235}$U isotope required for nuclear fission. [3]

In 1943, the first commercial mass spectrometer became available through the Consolidated Engineering Corporation [3], opening up new avenues of research. Applications to organic chemistry began in the 1950s, when high-resolution mass spectrometers became available, paving the way for accurate mass measurements. During the 1960s, mass spectrometry became a promising analytical tool in the analysis of organic compounds. [3] It has been, and continues to be, widely used to determine the molecular composition of compounds and quantify their components. To make precise measurements, however, molecules must be ionized. Unlike neutral species, the motion and direction of ions are easier to manipulate. [3] As such, three basic steps are involved in the mass spectrometry analysis, as illustrated in Figure 1.1.

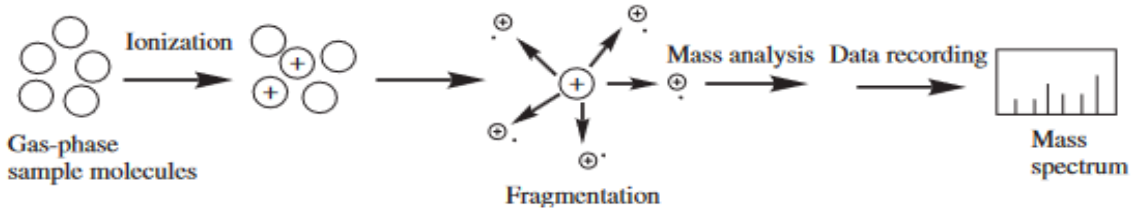


**Figure 1.1** Adapted from Fundamentals of Contemporary Mass Spectrometry; Wiley-Interscience [3]. Steps involved in the mass spectrometry analysis.

The first step is ionization. Molecules and atoms in the gas-phase are converted to their ionic form, by adding or removing an electron or proton(s). Traditionally, gas-phase molecules are bombarded with a high-energy beam of electrons (~ 70 eV). During this process, known as electron ionization (EI), an electron is removed from the highest-occupied molecular orbital (HOMO) of the neutral molecule, producing cationic species. The excess energy transferred during ionization leads to further fragmentation of the molecule, breaking it apart into characteristic fragments. [3] The next step is to separate the ions according to their *m/z* (mass-to-charge) ratios. [3] Finally, the ion current generated by the ions are measured, amplified, and displayed in the form of a mass spectrum, a computer-generated bar-graph plot illustrating the relative abundance of the signals (y-axis) based on their respective *m/z* ratio (x-axis). [3]

Hence, all mass spectrometers require a sample inlet system, ion source, mass analyzer, and detector. The sample inlet system is crucial for transferring the sample into the ion source, which will convert neutral sample molecules into gas-phase ions. [3] Once ionic species are produced by the ion source, they are transferred to the mass analyzer, separating the ions. [4] Among the various types of mass analyzers, common characteristics include resolution, the ability of a mass analyzer to separate ions with similar *m/z*; mass accuracy, the ability to assign the measured mass of an ion near its exact mass; and mass range, defined by the upper and lower limits (*m/z*) of the mass analyzers. [5] The detector is the final part of a mass spectrometer. Detectors play a crucial role in the mass spectrometer for the separated charged ions, which record the induced charges as ions move through the detector. [6] Also, unlike mass analyzers, detectors have important characteristics, including high amplification, fast response time, low noise, and high collection capacity. [4]

Initially, EI was the first ionization method to be developed for mass spectrometry. Consequently, MS and its applications to biological fields were limited, due to the lack of suitable ionization techniques for fragile and non-volatile biological compounds. [3] However, in the last few decades, several unique developments in the modes of ionization have emerged. These are classified as 'soft' ionization techniques due to their ability to produce ions from biological sources with minimal fragmentation. These methods include fast atom bombardment (FAB), electrospray ionization (ESI), and matrix-assisted laser desorption/ionization (MALDI). [3] As a result, mass spectrometry has since expanded its use in biology and the life sciences, emphasizing proteomic

and metabolomic research to facilitate our understanding of protein and metabolite function in biological systems.

Due to the 'soft' nature of such techniques, analytes are transferred into the gas phase without breaking any covalent bonds, thus providing information regarding the compounds' molecular weight (MW). While soft ionization is favourable for detecting biological molecules such as proteins, relying on the MW alone of compounds is insufficient for structure elucidation. As such, fragmentation of the gas-phase ions is necessary for establishing the structure of an unknown analyte. Tandem mass spectrometry (MS/MS) involves subjecting gaseous ions to two or more sequential stages of mass analysis. [7] In an MS/MS experiment, a precursor ion is selected by a mass analyzer (Q1) and focused into a collision cell (q2) to undergo fragmentation, via collision-induced dissociation (CID). CID is among the most commonly employed methods where selected ions collide with a neutral inert gas (i.e. nitrogen, helium, or argon) in the collision cell, leading to the activation of the precursor ion by increasing its internal energy. [7] As a result, this activation leads to the homolytic or heterolytic cleavage of chemical bonds, producing different fragment (product) ions. These product ions are sent to the last mass analyzer (Q3) to generate the product ion mass spectrum. [7]

### 1.2 Mass spectrometry imaging (MSI)

Among the vast number of analytical techniques, mass spectrometry imaging (MSI) remains a promising tool for investigating a wide array of molecules within biological tissues exhibiting spatial heterogeneity. [8] It allows for untargeted investigations into the spatial distribution of molecular species capable of imaging thousands of molecules, such as proteins, lipids, metabolites, and glycans, within a single experiment. [9] MSI is a technique that merges the *m/z* measurement capability of mass spectrometry with a surface sampling process that enables the investigation of the small molecule and proteomic content of tissues. [10][11] As depicted in Figure 1.2, this process involves careful sample preparation and setting a predefined (x, y) grid over the sample surface. [9] The mass spectrometer's ion source ionizes the sample surface using an ion beam, laser, or a charged solvent spray. It then captures a mass spectrum at each grid point (pixel), systematically scanning the sample surface with a moving stage or probe, where the grid's dimensions determine the spatial resolution. [9] Specialized software analyzes these spectra to identify specific ions with a particular *m/z*, extracting intensity values to create a chemical (ion)

image in order to depict the distribution of a specified ion throughout the sample. As previously mentioned, confirmation of chemical identity is typically obtained through MS/MS, providing a spectral profile unique to a molecular compound and allowing for structure elucidation. [9] Alternatively, depending on the mass resolution and within a specified error range, matching the intact mass to known databases allows for tentative identification. [9]

In summary, every ion measured is assigned to a precise location (pixel) on the sample surface, facilitating the creation of ion images for the numerous amounts of ions measured in the mass spectra. [11] The idea of combining the *m/z* measurement functionality of mass spectrometers with imaging capability to produce molecular images goes back several decades, and many techniques have been developed ever since. [11] For instance, widely used MSI techniques include MALDI, a soft ionization laser-based technique where ions are generated from discrete locations on the sample surface using laser irradiation [11], and desorption electrospray ionization (DESI), an ambient ionization technique that utilizes charged droplets to extract and ionize analytes from the sample surface. [12]

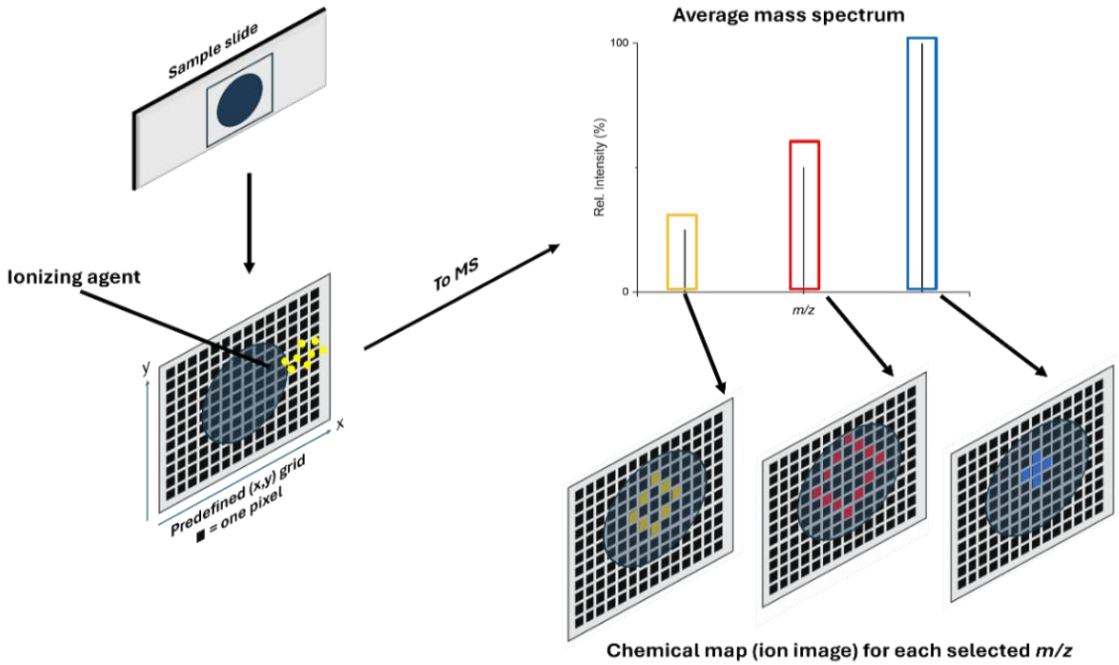


**Figure 1.2** Mass spectrometry imaging (MSI) workflow. A sample is mounted onto a slide and subjected to ionization through laser irradiation, an ion beam, or a charged solvent spray. This process ionizes molecules on the sample surface, and the gas-phase ions are guided through the mass spectrometer (MS) to produce mass spectra. Each spectrum, corresponding to a distinct pixel, captures the unique molecular composition of that spot. Selected ions (*m/z)* are then mapped to display their spatial distribution across the sample surface.

The significance of MSI-based techniques lies within the molecular network of living organisms. More precisely, to encapsulate as much information as possible within a sample and develop a robust understanding of the complex biochemical processes that occur within living organisms, it is critical to not only elucidate the molecular entities involved in these processes, but also to map and determine the distribution of these chemical species. [11] This capability enables both untargeted and targeted analyses, making MSI a prominent analytical technique for biological specimen characterization. Additionally, this versatility aids in identifying and understanding certain diseases by directly comparing diseased and healthy tissues. [9][13]

### 1.2.1 Matrix-Assisted Laser Desorption/Ionization Mass Spectrometry Imaging (MALDI-MSI)

Originating in 1987, matrix-assisted laser desorption/ionization (MALDI) is a rapidly emerging technology initially introduced by F. Hillenkamp and colleagues. [14] In 1988, Koichi Tanaka and colleagues introduced ultra-fine metal plus liquid matrix for laser desorption/ionization. [15] This approach allowed the generation of singly charged analytes of large biomolecules such as proteins. Since MALDI's introduction, much of the interest in this technique has expanded to many scientific fields over the years, particularly used for exploring disease pathology and for pharmaceutical applications. [16] However, it wasn't until the late 1990s that MALDI-MSI started to gain traction among the scientific community. This was primarily driven by the contributions of Richard Caprioli and his team, who demonstrated MALDI's efficacy in imaging large biomolecules such as proteins and peptides on mammalian tissue sections. [17] As a result, MALDI continues to progress in these domains while also expanding into new areas of research, particularly developmental and system biology, emphasizing proteomic and metabolomic-based studies. [11] Currently, MALDI has emerged as the favoured ionization technique for numerous MSI-based applications. Its attractiveness is due to its capacity to manage a diverse array of molecular species and molecular weights, encompassing metabolites, lipids (> 1 kDa), and proteins, with high sensitivity. [18] MALDI-MSI is, therefore, one of the leading techniques for analyzing molecular distributions across various tissues, including the brain, liver, skin, and kidney, and is essential in studying different diseases such as neurodegenerative disorders and cancer. [18]

To truly grasp the essence of MALDI as an analytical technique, it is of valuable interest to understand the fundamental basics of this method, starting from its methodological design, including sample preparation, all the way down to the instrumentation and ionization events that occur at the molecular level.

For analytes in solution, a common sample preparation method involves mixing a small volume of analyte with an excess amount of matrix solution, referred to as the dried droplet method. [19] This mixed solution can be applied onto a metal plate and air-dried. During the drying process, the matrix co-crystallizes with the analyte to form matrix-analyte crystals. [19] This dried spot is then subjected to laser irradiation for MS analysis.

In the context of imaging, a typical protocol for tissue analysis with MALDI-MSI can be broken down into several stages:

Tissue Handling and Storage

Once the tissue has been extracted, it must be kept under frozen conditions (kept at -80 °C or lower) to maintain its morphology and prevent significant molecular degradation. This will allow the tissue to remain in its native state for over a year. [16]

Tissue Sectioning and Mounting

The next process following tissue storage involves sectioning the tissue specimen into very fine and precise slices, commonly performed by a cryostat. For a majority of applications, the tissue is cut into 5-20 μm-thick slices at a temperature of -20 °C. [16] However, both the thickness and the temperature at which the tissue is cut are dependent on the type of tissue. Once sectioning has been performed, tissue sections need to be mounted. This involves applying the sections onto a MALDI target plate at a temperature similar to the cryostat. Next, the sections can be warmed by placing a hand under the target plate, a process known as thaw-mounting. Typically, the target plate in MALDI is electrically conductive, allowing it to maintain a high voltage potential from the ion source. In addition, to prevent charge-build up, indium tin oxide (ITO)-coated glass slides are commonly used as a MALDI target plate for tissue mounting. [16]

Matrices and Matrix Deposition

The most significant feature of MALDI and the effectiveness of this technique is strongly dependent on the chemical matrix used. The matrix compound facilitates the mechanism of ionization by absorbing the laser irradiation and transporting the sample to a gas phase. [16] Thus, as shown in Figure 1.3, matrices must be effective at absorbing photons at the laser's wavelength, capable of converting laser energy into heat, and be able to perform charge transfer reactions from a neutral, or excited state. [10] In addition, matrix compounds are chosen depending on the type of analytes to be ionized and thus detected. This is determined based on their ability to provide adequate ionization for a particular class of analytes. Therefore, their structure, pH, and proton affinities play a critical role and can affect the observed analyte sensitivity. [11] Choosing the right matrix compound for the intended analysis is required to achieve optimal results.

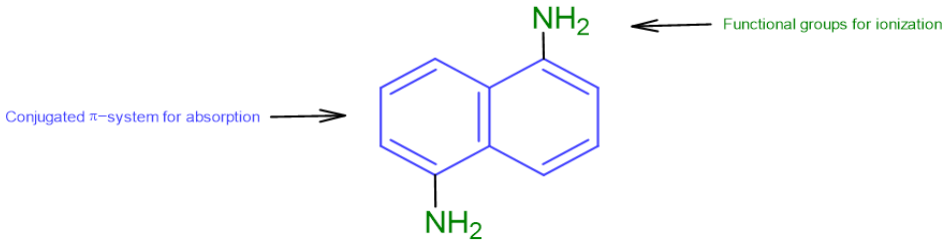


**Figure 1.3** Chemical structure of 1,5-diaminonaphthalene, a common MALDI matrix compound.

Since the birth of MALDI-MSI, numerous compounds have been studied for their ability to function as a MALDI matrix. However, aside from the type of matrix compound used, a key aspect is the application of the matrix to the mounted sections, a critical determinant of spatial resolution and the number of ions to be detected. [11] In addition, how the matrix is applied to the tissue can significantly impact matrix uniformity, crystal size, and localization of analytes. [20] [21] All these factors can affect the image resolution in MALD-MSI. As such, the application of the matrix can be broken down into two matrix deposition techniques: wet and dry depositions. Wet deposition techniques include matrix spraying. Typically, in the context of matrix spraying, wet-interface systems such as automated sprayers provide a dispersion of very fine droplets of matrix solution onto the sample surface, forming a homogenous layer of crystals. [11] This can also be performed with hand-held aerosol sprayers, airbrushes, and micro-spotters. [20][21] Initially, matrix powder is dissolved in a wide range of organic solvents, with their concentration ranges varying depending on the research objective. The following matrix solution is sprayed over the tissue, where the height of the spray nozzle, nozzle velocity, gas flow rate, and temperature can

be adjusted accordingly for optimal deposition. [22] Wet deposition techniques offer more efficient analyte extraction and co-crystallization between the analyte and matrix than dry deposition, which is critical for protein analysis. [23] However, a major concern is the size of the droplet, which typically affects the maximum achievable spatial resolution. Over-spraying the matrix can also lead to further complications, risking the delocalization of analytes from the tissue surface. [20][21]

In contrast, dry deposition techniques, such as sublimation, remain solvent-free. Instead, the matrix compound is exposed to high temperatures within a low-pressure environment. This will facilitate the transfer of the matrix from the solid phase to the vapour phase without decomposition [21], which is favourable for the analysis of lipids. [23] Given the absence of solvents, this technique minimizes the risk of analyte delocalization during matrix application. Moreover, sublimation applies a uniform layer of matrix over a large sample plate, forming microcrystals (smaller than spraying), increasing the matrix purity and the analyte signal. [21] Typically, sublimation experiments are performed using a sublimation apparatus, which consists of two main components: a water-cooled condenser and a sublimation chamber that functions as the matrix holder. [24] Initially, an ITO-slide containing the mounted tissue section is attached to the bottom of the condenser in the sublimation apparatus, attached with copper tape to ensure adequate and uniform thermal contact. Matrix powder (~300 mg) is placed at the bottom of the sublimator chamber, and these components are sealed together with an O-ring seal. The entire system is connected to a cold trap and a vacuum pump. [24] Upon achieving the designated pressure of 30-50 mtorr, the condenser is supplied with cold water. Heat is then supplied to the base of the sublimator chamber using either heated sand or heated oil. During this process, the matrix is heated, sublimated, and deposited onto the sample. Within a designated amount of time, the chamber is returned to room temperature, opened, and the ITO-matrix coated slide is detached from the underside of the condenser [24], ready to be subjected to MALDI-MSI analysis.

Instrumentation and Ionization Mechanisms

As mentioned previously**,** a mass spectrometer has three fundamental components: the ion source, the mass analyzer, and the detector [16]. Given the fundamentals of MALDI, it functions as the ion source. Once the tissue section is cut, thaw-mounted on a conductive slide, and coated with matrix via wet or dry deposition techniques, the slide is introduced into a vacuum for MS

analysis. Spectral data, in terms of the sample's chemical profile, is acquired by moving the sample stage under a fixed laser position. [25] The focused laser, typically Nd;YAG (355 nm), irradiates each x,y position moving across the surface horizontally or vertically, separated by a defined distance. Multiple laser shots are summed to generate a single mass spectrum for each given position. Ultimately, an averaged mass spectrum is computed from the data acquired at each irradiated spot. [25] Specialized proprietary software is used to generate ion images by mapping the ion's abundance at each pixel, revealing the localization of the ion across the scanned area. As a result, by conducting MALDI-MSI, the spatial arrangements of the target analyte and its respective signal intensity can be observed across the tissue surface. [25]

Thus far, it is evident that MALDI utilizes a laser irradiation-absorbing matrix to produce ions from complex mixtures. The emission of a UV laser beam onto the analyte-matrix mixture leads to the absorption, energetic ablation, and desorption of the top layer of material as a hot plume of gaseous molecules. [16][25] It is within the hot gaseous plume where, over the years, researchers have attempted to elucidate the mechanisms of ionization, investigating the question central to MALDI: "How does ionization occur?". Despite the significant efforts that have been made in understanding the mechanisms that take part in ionization, the exact processes are still under study. Nevertheless, various mechanisms are involved.

Charge Separation and Photoionization

Ionization occurs through charge separation or photoionization within matrix-analyte clusters. [26] This mechanism requires that analytes be incorporated in their charged state as defined by the solution pH. Typical MALDI analytes, such as peptides/proteins, are precharged in the matrix crystal. Therefore, an active ionization step via charge transfer to neutral species is not required. [26] Mechanistically, charge separation may occur when charged species within a cluster are formed with either a deficit or excess of ions. The energy to separate ion pairs is provided by the laser-induced cluster explosion, overcoming the coulombic attraction between the opposite charges and, as a result, separating the ions. [26] Hence, within this mechanism, the role of the matrix is substantially reduced since an active contribution to ionization is no longer necessary.

In contrast, photoionization occurs when the laser's photons directly ionize matrix molecules or analytes via excitation to a higher energy state. This can happen within the laser-irradiated cluster or when transported to the gas phase. [26] However, there is a large debate about

whether a UV laser (e.g., 337 nm) employed in MALDI may provide enough energy to achieve ionization. Hence, while initially favoured in earlier MALDI studies, current investigations indicate it may play a less dominant role in MALDI ionization.

Interionic-Proton Transfer

Once clusters are formed and charged, proton transfer events become key in determining the final ions observed in the mass spectra. [26] This process encompasses both protonation and deprotonation events of analytes. Protonation occurs when proton-rich matrix ions transfer protons to the analytes. Conversely, deprotonation involves analytes transferring protons to nearby matrix molecules. [26] These reactions are generally energetically favourable and are particularly relevant to proteins and peptides, which have multiple basic sites that accept protons. In addition, it may also explain why other analytes with basic or acidic functional groups, such as oligonucleotides and lipids, form stable deprotonated or protonated ions in MALDI. [26]

Cluster Ionization

This model suggests the dominant ionization pathway in MALDI, integrating various mechanisms such as charge separation and interionic-proton transfer, all happening within clusters of matrix and analyte molecules. The formation of a cluster containing both matrix and analyte molecules engages in several forms of reactions and is formed due to the explosive disintegration of the matrix after absorbing laser energy. Besides charge separation, ions are generated due to secondary reactions, such as proton transfer, to generate the final ions observed in the mass spectra. Hence, the clusters can be considered a reaction vessel, facilitating secondary reactions and providing a protective environment for the analytes from direct laser impact. [26]

To summarize, the steps involved in MALDI ionization are complex and believed to occur under the influence of several mechanisms occurring simultaneously. However, the matrix proves essential for energy absorption and analyte protection. Specific ionization pathways highly depend on the characteristics of the matrix, the analyte, and the experimental conditions employed.

## 1.3 Instrumentation

This section will highlight the instrumentation used to attain my research goals, including the QExactive™ Quadrupole-Orbitrap hybrid mass spectrometer and Spectroglyph LLC, MALDI/ESI Injector™.

### 1.3.1 QExactive™ Quadrupole-Orbitrap hybrid mass spectrometer

All experiments, as discussed in the subsequent chapters of this thesis, utilized the QExactive™ hybrid mass spectrometer for collecting MS and MSI data. The QExactive series instruments are standalone Orbitrap instruments with an atmospheric pressure ionization (API) source for liquid chromatography-mass spectrometry (LC-MS) applications. [27] This mass spectrometer consists of four main components: the ion source, storage device (C-trap), collision cell for higher energy collision dissociation (HCD) experiments, and an Orbitrap mass analyzer for Fourier transform mass analysis. [27] A schematic of the instrument is shown in Figure 1.4.

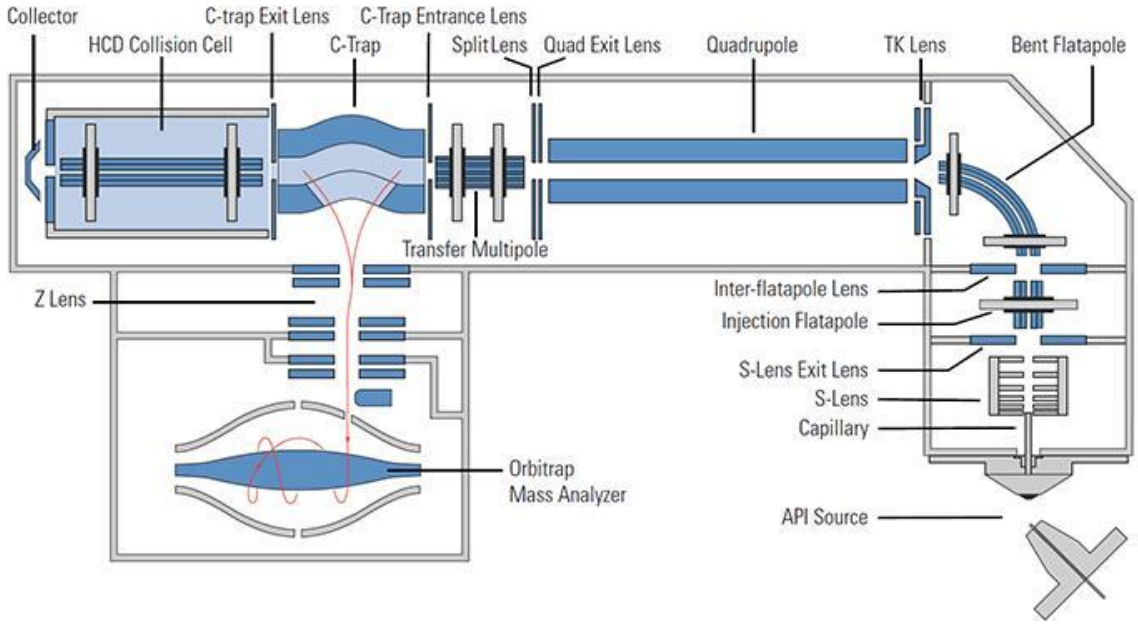


**Figure 1.4** Adapted from Thermo Fisher Scientific Exactive Series operations manual [27]. Schematic of QExactive hybrid mass spectrometer.

Ions can be produced and introduced by several sources, such as ESI. Ions are transmitted through a series of electrodes that act as ion focusing devices, like the injection flatapole. [27] Subsequently, ions are guided by the bent flatapole, transmitting ions through a 90° arc from the injection flatapole to the quadrupole. From the quadrupole, ions are transmitted into the gas-filled curved linear trap (C-Trap). [27] Upon entering, ions lose their kinetic energy due to collision with

nitrogen bath gas. For ion extraction, ions are pushed orthogonally by voltage pulses into the curved axis through a slot in the inner electrode, arriving in the Orbitrap mass analyzer. [27]

### 1.3.2 Spectroglyph LLC, MALDI/ESI Injector™

Coupled with the QExactive™ hybrid mass spectrometer is the Spectroglyph LLC, MALDI/ESI Injector™. The dual MALDI/ESI interface is a programmatically controlled interface designed for performing MSI experiments for biological samples as well as shotgun/top-down proteomics with LC-MS. [28] MALDI-MSI experiments are performed at elevated pressure (EP), in the range of 5 to 8 torr, while ESI can be conducted at atmospheric pressure orthogonally to the interface axis. As illustrated in Figure 1.5, the MALDI injector utilizes a dual ion funnel interface: high-pressure funnel (HPF) and low-pressure funnel (LPF), separated by a pneumatically driven gate valve. [28] The HPF is uniquely designed with rectangular slits to enable laser focusing on a MALDI target slide, mounted on a motorized vacuum translation stage positioned in front of the HPF. [28] The laser, Nd:YLF (349 nm), is focused by a beam expander to a spot size of ~ 20 µm, whereby upon laser irradiance, MALDI-generated ions are accelerated by an electric field and are transmitted through the HPF to the LPF. [28] The following ions are then guided through the rest of the mass spectrometer for mass spectral analysis, as described in section 1.3.1.

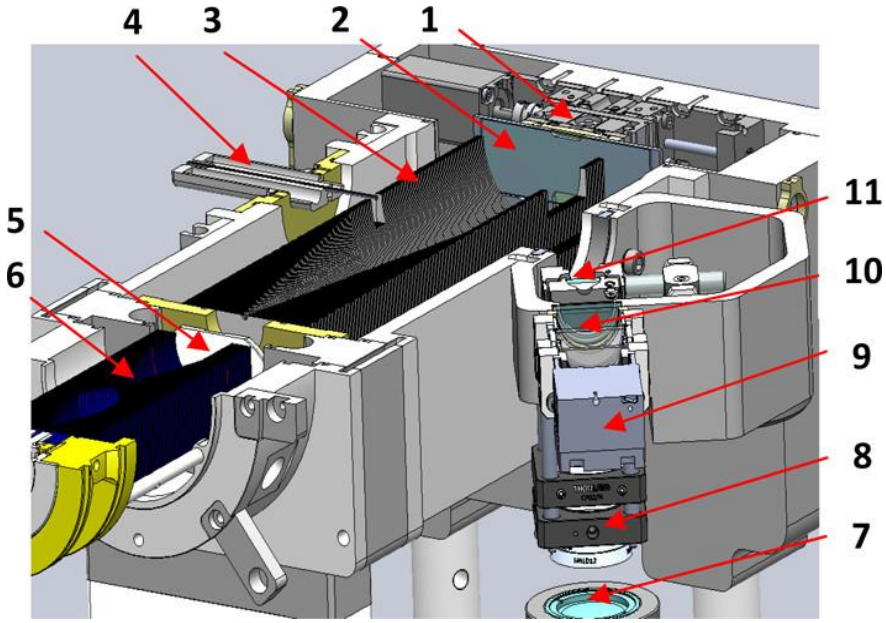


**Figure 1.5** Adapted from Mikhail E. Belov et al [28]. Schematic of the MALDI/ESI interface. The following numbered components are as shown: 1) translation stages, 2) MALDI slide, 3) Higher Pressure Ion (HPF) funnel, 4) MS inlet, 5) slide valve, 6) Low Pressure Ion (LPF) funnel, 7) 20× 355 nm laser beam expander, 8) 200 mm UV-grade fused silica lens, 9) CCD camera, 10) long pass colored filter, and 11) 355 nm 45° laser line mirror.

### 1.4 Phosphatidylinositols (PIs) and Phosphoinositides (PIPs)

Among the different types of biomolecules, lipids play a vital role in many different cellular processes; they are components of the cell membranes, serve as structural barriers, function as energy sources, and participate as intermediates in signalling pathways. [29] Structurally, many lipids typically comprise a glycerol backbone with two non-polar fatty acyl side chains at the sn-1 and sn-2 positions, which may be saturated or mono- and polyunsaturated, along with a distinctive head group. The head group divides lipids into several classes, whereby the classification is according to their polarity. [29] As a result, these biomolecules can be broken down into eight categories: fatty acyl (FA), glycolipids (GL), glycerophospholipids (GP), sphingolipids (SP), sterol lipids (ST), prenol lipids (PR), sachharolipids (SL), and polyketides (PK). Within these lipid classes, contain a wide range of molecules with distinct physiochemical properties and composition of fatty acyl chains. However, even with their unique chemical properties, the homeostasis of lipids contributes to different pathological processes. Thus, the disruption or alterations of lipids can be consequential, leading to a wide array of pathological issues, such as cardiovascular diseases, diabetes, inflammation, and neurological/neurodegenerative diseases. [29]

Across the lipidome, glycerophospholipids, particularly phosphatidylinositols (PIs) and their phosphorylated forms, phosphoinositides (PIPs), are low-abundance phospholipids that are essential regulators of cell signalling reactions in both health and disease. [30] Like most lipids, PIs contain a glycerol backbone linked to a different variety of fatty acid chain pairs, with species containing 1-stearoyl-2-arichaidonyl acyl chains being the most prevalent. What distinguishes PIs and PIPs from other phospholipids, however, is the myo-inositol head group. [31] The cyclic inositol ring of PIs possesses free hydroxyl moieties, which can be selectively phosphorylated at positions 3, 4, and 5 to generate seven distinct species of PIs. This phosphorylation process is facilitated by a group of enzymes called phosphoinositide kinases in the major pathway for the biosynthesis of PIs and PIPs, the phosphatidylinositol cycle (PI-cycle). [31] These include three unique species of phosphatidylinositol monophosphate (PIP): phosphatidylinositol-3-phosphate (PI3P), phosphatidylinositol-4-phosphate (PI4P), and phosphatidylinositol-5-phosphate (PI5P); three species of phosphatidylinositol bisphosphate (PIP2): phosphatidylinositol-4,5-bisphosphate [$PI(4,5)P_2$], phosphatidylinositol-3,5-bisphosphate [$PI(3,5)P_2$], and phosphatidylinositol-3,4-

bisphosphate [PI(3,4)$P_2$]; and a single phosphatidylinositol triphosphate (PIP3): phosphatidylinositol-3,4,5-trisphosphate [PIP3]. [31]

The physiological functions of PIPs are directly linked to their subcellular distributions across different organelles in eukaryotic cells. [32] Generally, PIPs are located in the cytoplasmic leaflet of eukaryotic cell membranes and various studies have revealed they are present in defined proportions. [30][31] Typically, PIs constitute 10-20% of total cellular phospholipids, expressed in mole percentage. In contrast, PIPs are present at lower concentrations, with PI4P and PI(4,5)$P_2$ accounting for 0.2-1% of total phospholipids, whereas PIP3 accounts for < 0.05% of total PIPs. [30][32] It is important to note, however, that these levels fluctuate in a precise and reversible manner in response to cellular changes or external stimuli. [30] Nevertheless, despite the low concentrations, PIPs are crucial in numerous biological processes. Specifically, PI(4,5)P2 and PIP3 are critical signalling lipids involved in different cellular processes, including cytoskeletal dynamics, membrane trafficking, and signal transduction. [33] PIP3, in particular, plays a major role in activating downstream signalling pathways, notably the PI3K/Akt pathway. [34] This pathway controls cell growth, survival, and metabolism, important for physiology and cancer development. As such, dysregulation of PIP3 levels is observed in cancer, with mutations in the Akt pathways contributing to tumour growth and therapy resistance. [34][35]

### 1.4.1 Atypical Hemolytic Uremic Syndrome (aHUS)

Hemolytic uremic syndrome (HUS) is a type of thrombotic microangiopathy (TMA) marked by thrombocytopenia, macroangiopathic hemolytic anemia, and acute kidney injury. [36] This disease is most commonly caused by Shiga toxin-producing *Escherichia coli*, originating from contaminated food or drinks, and accounts for 90-95% of HUS cases. [36] Conversely, a rare form of HUS, known as atypical HUS (aHUS), constitutes 5-10% of all HUS cases and is typically associated with genetic mutations acting on the alternative complement pathway, leading to significant kidney injury and renal failure due to thrombosis in the kidney glomeruli. [36][37] Unlike HUS, patients suffering from aHUS do not regain kidney function without treatment. In fact, without treatment, 50% of aHUS cases progress to dialysis, with a mortality rate of 25%. [36]

Numerous different genetic forms of aHUS have been studied that lead to the overactivation of the complement system. Among these studies, Vincent So and colleagues have shown that loss-of-function mutations in diacylglycerol kinase epsilon (DGKε), a lipid kinase,

causes a novel form of aHUS. [37] This particular isoform of diacylglycerol kinase (DGK) has a central role in the PI-cycle, with high specificity for DAG conjugated with arachidonic acid (AA) at the second carbonyl group, i.e. 1-stearoyl-2-arachidonoyl glycerol. [37][38] As depicted in Figure 1.6, DGKε phosphorylates diacylglycerol (DAG) to phosphatidic acid (PA); DAG is produced when PI(4,5)P2 is hydrolyzed by phospholipase C (PLC). [37] As suggested by Vincent So and colleagues, based on this enzymatic mode of action, it is probable to suggest that DGKE deficiency leads to an increased amount of its substrate, DAG, and depletion in its product, PA. However, MS lipidomic data of DGKε-deficient immortalized umbilical vein endothelial cells (iHUVEC) and blood outgrowth endothelial cells (BOEC), revealed that high levels of DAG were not observed in the two DGKε-deficient models. Rather, a reduction in PI(4,5)P2 was observed, a direct consequence of reduced 38:4-PA, followed by secondary reductions in PIP3. [37] These reductions are crucial to the pro-thrombotic phenotype displayed by patients with aHUS caused by DGKε deficiency. [37]

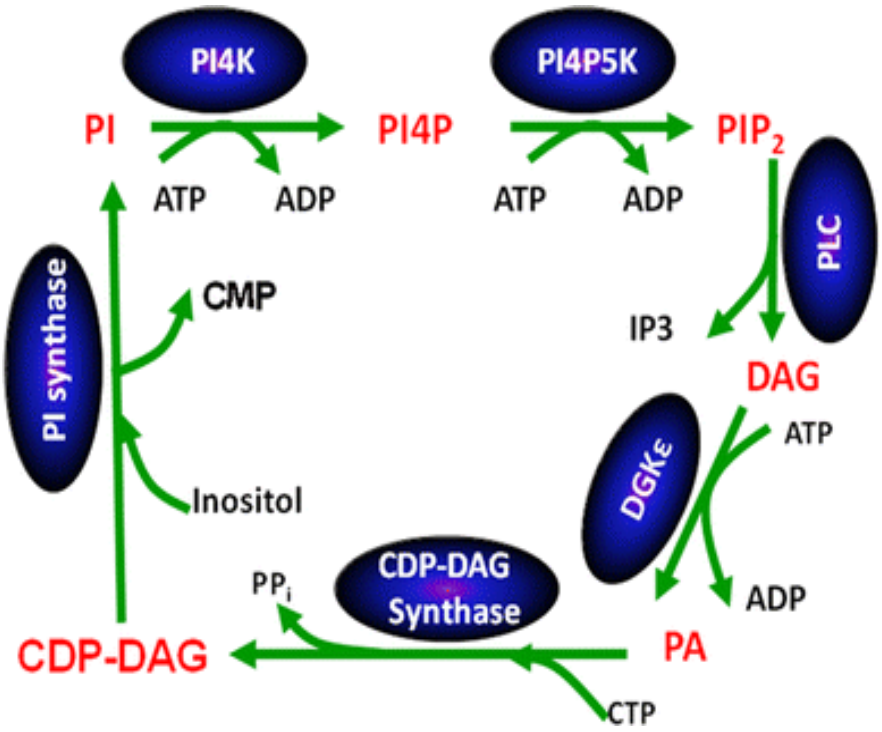


**Figure 1.6** Adapted from Richard M. Epand [38]. The phosphatidylinositol cycle (PI-cycle); the major pathway involved in the synthesis of PIs and their phosphorylated derivatives, PIPs. The enzymes involved in the catalysis of each step are represented by the blue ovals. Lipid intermediates are written in red.

## 1.5 **Research Objectives**

The primary objective of my research was to explore the chemical profiles associated with aHUS. Building on the research by Vincent So and colleagues, my study aimed to explore changes in the omics landscape and examine the potential biomolecular alterations and their effects on cellular activities in aHUS caused by DGKε mutations. The spatial distribution of these alterations would also be obtained with MALDI-MSI. Therefore, two types of mouse kidney models will be investigated: DGKε-deficient (KO) and DGKε-nondeficient mice (WT). However, before investigating this complex disease, various preparation steps were required:

1) Considering the significance of the MALDI matrix (section 1.2.1), it is imperative to select an appropriate matrix for the detection of both PIs and PIPs with high sensitivity. As a consequence, several matrices, notable for the analysis of phospholipids, were assessed, optimizing their coating density to improve the detection of PIs and PIPs. The subsequent section of this thesis will dive deeper into these explorations.

2) Enhancing the detectability and confirming the identity of these lipid species via MS/MS is crucial, as described in section 1.1. Based on our obtained findings from chapter two, my research will extend to not only testing various matrices for their detection capabilities but also examining the internal energy distribution, P(E), of each matrix. This is essential given the physiochemical properties of PIPs, which could be susceptible to in-source fragmentation (ISF) during the MALDI process and, hence, affect the accuracy of the mass spectral results. In doing so, specialized molecules known as thermometer ions, which are instrumental in evaluating the internal energy distribution of gas-phase ions [39], will be used to determine P(E). This approach aims to determine whether or not the detectability of these species is affected by their ISF or, alternatively, their low abundance in biological matrices. These hypotheses are explored in chapter 3 of this thesis.

Below is an outline of the chapters that will be discussed in greater detail, addressing each research objective. The contributions from each author, including myself, and publications, have been noted below.

**Chapter 2:**

Assessment of MALDI matrices for the detection and visualization of phosphatidylinositols and phosphoinositides in mouse kidneys through matrix-assisted laser desorption ionization mass spectrometry imaging (MALDI-MSI). (Laurentiu G. Dabija, Maryam Yousefi-Tameah, Ergi Duli, Mathie Lemaire, Demian R. Ifa).

Both Dr. Maryam Yousefi-Tameah and I contributed equally to the methodology of the experiments and writing (original draft/review and editing). Specifically, Maryam optimized and obtained MSI data for each MALDI matrix at various coating densities and gathered all relevant PI and PIP compounds. I obtained MSI and MS/MS data for the triplicate analyses at the optimal coating density for each matrix, mapped the distributions of each relevant PI and PIP compound, performed the formal analysis of the results (data interpretation), and created/interpreted all figures. Ergi Duli and Dr. Mathieu Lemaire provided the samples and writing contributions (review and editing). Prof. Demian R. Ifa provided supervision (leadership responsibility), technical support, feedback, and writing contributions (review and editing).

**Chapter 3:**

Determination of the internal energy distributions of various MALDI matrices: Implications for the direct analysis of phosphatidylinositol-3,4,5-triphosphate. (Laurentiu G. Dabija, Kai Chi Lau, Alan C. Hopkinson, Demian R. Ifa)

I conducted all MS experiments, SY calculations, and wrote the original manuscript (original draft/review and editing). Density-functional theory (DFT) calculations were conducted and interpreted by Kai Chi Lau and Prof. Alan C. Hopkinson, and they provided feedback and writing contributions (review and editing). Prof. Demian R. Ifa provided supervision (leadership responsibility), technical support, guidance for the experimental outline, and writing contributions (review and editing).

# Chapter Two: Assessment of MALDI Matrices for the Detection and Visualization of Phosphatidylinositols and Phosphoinositides in Mouse Kidneys through Matrix-Assisted Laser Desorption Ionization Mass Spectrometry Imaging

Version of the published manuscript:

**Dabija, L. G**.; Yousefi-Taemeh, M.; Ergi Duli; Lemaire, M.; Ifa, D. R. Assessment of MALDI Matrices for the Detection and Visualization of Phosphatidylinositols and Phosphoinositides in Mouse Kidneys through Matrix-Assisted Laser Desorption Ionization Mass Spectrometry Imaging (MALDI-MSI). *Analytical and bioanalytical chemistry/Analytical & bioanalytical chemistry* **2024**, *416* (8), 1857–1865.

## 2.1 Abstract

Phosphatidylinositols and their phosphorylated derivatives, known as phosphoinositides, are crucial in cellular processes, with their abnormalities linked to various diseases. Thus, identifying and measuring phosphoinositide levels in tissues are crucial for understanding their contributions to cellular processes and disease development. One powerful technique for mapping the spatial distribution of molecules in biological samples is matrix-assisted laser desorption/ionization mass spectrometry imaging (MALDI-MSI). This technique allows for the simultaneous detection and analysis of multiple lipid classes in situ, making it invaluable for unbiased lipidomic studies. However, detecting phosphoinositides with MALDI-MSI is challenging due to their relatively low abundance in tissues and complex matrix effects. Addressing this, our study focused on optimizing matrix selection and thickness for better detection of phosphatidylinositols and their phosphorylated forms in mouse kidney tissues. Various matrices were assessed, including 9AA, DAN, CMBT, and DHA, adjusting their coating to improve ionization efficiency. Our results demonstrate that DAN, DHA, and CMBT matrices produced high-intensity chemical images of phosphatidylinositol distributions within kidney sections. These matrices, particularly DAN, DHA, and CMBT, allowed the identification of even low abundance phosphoinositides, through tentative identifications. Notably, DAN and DHA served as optimal candidates due to their prominent detection and ability to map a majority of phosphatidylinositol species, while CMBT showed potential detection capability for phosphatidylinositol triphosphate compounds. These findings not only provide valuable insights for future research on the involvement of phosphoinositides in kidney pathophysiology, but also propose the use of the identified optimal matrices, particularly DAN and DHA, as the preferred choices for enhanced detection and mapping of these lipid species in future studies.

## 2.2 Introduction

Among various metabolites, lipids are of rising research interest due to their vital structural, signaling, and metabolic roles in living systems. [40] Cellular lipids experience dynamic flux to influence membrane fluidity and permeability, are critical energy storage molecules, serve as metabolites for biochemical processes, and act as docking sites for protein effectors or vesicles. [40] Phospholipids encompass a diverse subgroup of lipids, one of which are low abundance phosphatidylinositols (PIs). PIs are acidic phospholipids linked to a myo-inositol

head group. [41] While the glycerol backbone is linked to a wide variety of fatty acid chain pairs, the cyclic inositol group possesses free hydroxyl moieties that may be phosphorylated at positions 3, 4, and 5. [41] As a result, the partial and full phosphorylation of the inositol ring generates seven distinct species of PIs, collectively known as phosphoinositides or phosphatidylinositol phosphates (PIPs). As such, there are three major subgroups: phosphatidylinositol monophosphate (PIP), phosphatidylinositol bisphosphate (PIP2), and phosphatidylinositol trisphosphate (PIP3). These phospholipids play fundamental roles in various settings, including protein interaction and regulation, membrane transport, cytoskeletal regulation, and plasma membrane signaling. [41-43]

The distribution of phosphoinositides exhibits significant heterogeneity at the cellular level, with each phosphoinositide species being most prominent on specific organelle membranes. [44, 45] Abnormalities in phosphoinositide levels, often associated with altered expression or activity of their relative kinases and phosphatases, have been implicated in a variety of diseases. These include diseases affecting the nervous system, contribute to the development of cancer, and play roles in inflammation, immunity, and thrombotic processes. [42] To gain a comprehensive understanding of the roles of PIPs in cellular processes and disease pathogenesis, accurate determination and tracking of their levels in various tissues are crucial. Traditionally, liquid chromatography-mass spectrometry (LC–MS) has been the preferred method for performing these analyses due to its accuracy and reliability in quantifying lipid species. However, using LC–MS requires the homogenization of organs and precipitation of lipid extracts. These processes are time-consuming and solvent/labor-intensive, posing a risk of degrading sample quality and have the potential to alter lipid profiles during sample preparation. Additionally, these methods do not provide spatial distribution information, which is crucial for a comprehensive analysis [43, 46-50].

Mass spectrometry imaging (MSI) has emerged as a promising and powerful tool for mapping the spatial distribution of molecules on biological sample surfaces. [51, 52] In this technique, numerous chemical compounds can be detected and spatially mass-resolved concurrently based on their mass-to-charge ratio (*m/z*). As a result, data obtained from MSI can unravel the cause of certain diseases by studying the metabolite expression and biomarker

measurements from disease versus healthy tissue comparisons. [52] Recent advancements in MSI, particularly through matrix-assisted laser desorption/ionization (MALDI), have enabled the generation of detailed chemical maps for PIs and other lipid species. MALDI-MSI is an analytical technique offering sensitive, specific, label-free imaging that can simultaneously acquire the spatial distribution, relative abundance, and structural information for numerous biomolecules in cells and tissues. This includes lipids, small drug molecules, peptides, proteins, and other compounds, crucial for understanding the molecular dynamics at the single-cell level. [53, 54] The ability of MALDI-MSI to detect and analyze multiple lipid classes in their natural biological context makes it an invaluable tool for lipidomic studies in preclinical and clinical settings, offering profound insights into the complex biochemistry underlying various diseases. [55-57]

Moreover, MALDI utilizes a matrix, a small organic compound to assist in the desorption and subsequent ionization of analytes from the sample surface. Identifying an effective matrix is crucial for the successful analysis of MALDI-MSI. The characteristics and the amount of matrix compound have a direct influence on the signal intensity of the analytes and ultimately the sensitivity of the analysis. [58] Therefore, the careful selection and optimization of the matrix in MALDI- MSI are essential, as they directly impact the accuracy and effectiveness of this technique in providing detailed and reliable molecular insights.

In the literature, several matrices have been suggested as compatible with lipids or phosphatidylinositols in general. Notably, Müller et al. investigated the detection limits of PIPs with MALDI-TOF. They established that these compounds' chemical and physical properties result in a high detection limit (poor detectability). [59] However, despite this report, a single matrix has not emerged as the definitive choice for achieving optimal results in the untargeted analysis of PIs and PIPs across diverse experimental settings. [60] In this context, we aim to identify, among the most widely employed matrices for phospholipid analysis, 5-chloro- 2-mercaptobenzothiazole (CMBT), 1,5-diaminonaphthalene (DAN), 9-aminoacridine (9-AA), and 2,5-dihydroxyacetophenone (DHA) [47, 58, 61-63], the best matrix applied via sublimation, for the detection of PIs and PIPs in mouse kidney samples. In doing so, we plan to systematically evaluate the matrix performance by exploring the distribution, analyzing the signal intensities, and lipid coverage, as previously proposed by T. B. Angerer et al. [64] Thus, this research focuses

on optimizing the matrix type and thickness to enhance MALDI-MSI sensitivity in detecting phosphatidylinositol and phosphoinositide compounds. Our initial efforts in fine-tuning and determining the optimal matrices for the detection of these species may offer a valuable resource for the MSI community. By laying this foundation, future endeavors can build upon our findings to further refine MALDI's detection capabilities, paving the way for advanced disease pathology research.

## 2.3 Experimental

### Materials and reagents

All matrix compounds, 5-chloro-2-mercaptobenzothiazole (CMBT), 1,5-diaminonaphthalene (DAN), 9-aminoacridine (9-AA), and 2,5-dihydroxyacetophenone (DHA), were purchased from Sigma-Aldrich (St. Louis, MO, USA). Indium tin oxide (ITO) coated slides were purchased from Delta Technologies (Loveland, CO, USA). HPLC-grade reagents were purchased from Sigma-Aldrich (Oakville, ON, Canada). The Omano microscope was purchased from the Omano Scientific store (Roanoke, VA, USA). Kidney samples were provided by the University of Toronto, Ontario, Canada. Female mouse kidneys ($n$ = 3 animals; 16 weeks old) were frozen and stored at a temperature of − 80 °C until required for sectioning and subsequent MALDI experiments.

### Sample preparation

Thin kidney tissue Sects. (20 μm) were sliced transversely using a Shandon Cryotome device (Thermo Fisher Scientific, San Jose, CA, USA) and thaw-mounted onto indium tin oxide slides (100 Ω/m2), for subsequent MALDI imaging analyses. The ITO-coated glass slides containing sample sections were removed from the freezer and subjected to a drying process in a vacuum desiccator for 30 min. Each matrix compound was then applied via sublimation, using a custom-built sublimation apparatus with a sublimation chamber. [21] In brief, the sample glass slide was securely attached to the flat-bottom condenser using copper tape, ensuring consistent heat transfer. A matrix chamber was filled with approximately 300 mg of matrix powder, and the sample holder and chamber were sealed with an O-ring. The system was connected to a vacuum pump, reaching a pressure of 0.05 Torr. The condenser was cooled with ice, while the chamber

was submerged in heated oil. Depending on the matrix type and following a specific time interval, the matrix was heated, sublimed, and deposited onto the sample. The system was then brought to ambient pressure (after 2 additional minutes), and the sample glass slide was carefully detached from the condenser. A range of matrix thicknesses was achieved by varying the sublimation temperature and time periods (Fig. S1).

**MALDI analyses**

MALDI-MSI experiments were performed utilizing a Q-Exactive mass spectrometer (Thermo Fisher Scientific, San Jose, CA, USA) equipped with a Spectroglyph ESI/MALDI ion source (Spectroglyph LLC, Kennewick, WA, USA). Data acquisition parameters included a resolving power ($m/\Delta m$) of 70,000 at *m/z* 200, a maximum injection time of 200 ms, and an *m/z* range between 250 and 1200 in the negative ion polarity. MALDI-MSI experiments were conducted to acquire ion images of different matrix coatings. Triplicate analyses were performed for each optimized matrix, selecting the most promising result within each group of thicknesses. All experiments were carried out at a spatial resolution of 50 μm. The laser (Nd:YLF, 349 nm) employed for analysis operated at different repetition rates, pulse energies, and shot numbers per pixel depending on the matrix type. The laser was operated at a repetition rate of 300 Hz with pulse energies of ~ 7 μJ for DAN, 9AA, and CMBT, as well as ~ 12 μJ at a repetition rate of 500 Hz for DHA. Details on the optimal laser settings can be found in Appendix A. On average, each pixel received 60–100 laser shots with an ablation diameter of approximately 30 μm. On tissue tandem-MS (MS/MS) was performed on 17 lipids (PIs and PIP) with a 1 Da isolation window, and collision-induced dissociation (CID) was executed with collision energies of 20–50%, tailored for each lipid. The matrices used for MS/MS applications were DAN, DHA, and CMBT. By utilizing both the Human Metabolome Database (HMDB) and LIPIDMAPS [65, 66], lipids were tentatively identified based on the following selection criteria: mass accuracy ($\leq$ 5 ppm) and, if applicable, characteristic fragment peaks. Also, data was included in the analysis even if the intensity of the signals was below $10^3$ counts. Ion images were generated using Spectroglyph ImageInsight software (version: 0.1.0.1668, Spectroglyph LLC, WA).

**Histochemistry and microscopy**

In order to obtain morphological information, a protocol for removing the MALDI matrix from the tissue surface was employed. [52] As such, to facilitate subsequent tissue staining, each matrix compound was removed from the kidney tissue by immersing the slide in a solution of 95% ethanol for 30–60 s, depending on the matrix type. The tissue section was then subjected to a standard hematoxylin and eosin (H&E) staining protocol, whereby the resulting optical images of H&E-stained tissue were obtained with an Omano microscope (Roanoke, VA, USA). However, challenges were encountered with significant tissue loss and cracking in some samples. Consequently, we present only the H&E images from the samples in optimal condition for each matrix. In addition, while the morphological features (cortex, medulla, pelvis) are not well depicted in the H&E images, it allowed us to identify areas of abnormality and pinpoint areas of tissue loss, which are essential for correlating with the MALDI-MSI data.

**Data analysis**

The average ion intensities for each corresponding PI and PIP compounds were normalized by total ion count (TIC) for each matrix type and extracted with the function of the ImageInsight software (version 0.1.0.1668). The following data was imported to Microsoft Excel, whereby a bar graph was constructed to compare the average of the peak intensities observed by all technical replicates. Herein, a logarithmic scale was used due to the range of intensities. Additionally, donut charts were created to capture the proportion of that species (PIs and PIPs) detected by each matrix.

## 2.4 Results and discussion

This study is comprised of two main parts. The first part focused on assessing the detectability of lipid species using matrices at various thicknesses. We optimized the density (coating) of each matrix on the sample surface through sublimation, considering their unique structures and characteristics. This was done by maintaining constant pressure and temperature while varying the sublimation time. To ensure efficient analysis and representative data, we selected the most promising results from the central region coronal sections of each kidney sample, which includes the renal cortex, medulla, and pelvis. This strategy aimed to provide a thorough

assessment of the targeted area while reducing analysis time, as shown in Fig. S1. The optimal thickness for each matrix was determined based on image quality (intensity and coverage). For instance, the DAN matrix showed the best results with a coating range of 0.10 to 0.26 mg/ $cm^2$, while the DHA matrix performed well within 0.20 to 0.35 mg/$cm^2$. For CMBT and 9AA, the optimal range was found to be 0.15 mg/$cm^2$ and 0.1–0.2 mg/$cm^2$, respectively. These findings are summarized in Table 2.1.

**Table 2.1** Sublimation parameters for optimal matrix thicknesses.

| Chemical matrix | Quantity (mg) | Temperature (°C) | Pressure (mTorr) | Time (sec) | Thickness (mg/$cm^2$) |
|---|---|---|---|---|---|
| DAN | ~300 | 160–165 | 50 | 90 | ~0.20 |
| CMBT | ~300 | 165–170 | 50 | 120 | ~0.15 |
| DHA | ~300 | 115–120 | 50 | 70 | ~0.25 |
| 9AA | ~300 | 180–185 | 50 | 180 | ~0.20 |

After selecting the optimal density for each matrix, the second part of our study focused on conducting triplicate MALDI-MSI analyses on transverse-cut kidney tissues. We then evaluated the performance of each matrix based on the previously mentioned criteria, including lipid coverage, signal intensity, and investigating the distribution of these compounds among the kidney surface. The goal was to ensure clarity and an accurate representation of the underlying molecular distributions. A list of reported PIs, PIP, PIP2, and PIP3 compounds was gathered from the literature and the Avanti Polar Lipids website. [67] Due to the extensive nature of the data collected, details such as exact masses, observed masses, and mass error (ppm) are provided in the supplementary information. The effectiveness of different matrix types and thicknesses in detecting these lipid species was thus thoroughly assessed.

**Molecular distributions of PIs and PIPs in the kidney**

One of the key parameters in our study was the visualization of a diverse array of PI and PIP species. This was essential to not only gauge the performance of each matrix, but also to facilitate a comprehensive mapping of these species, providing insights into the spatial distribution on the kidney surface. As illustrated in Figure 2.1, DAN successfully visualized the distribution of most PIs, exhibiting distinct morphological features of the kidney (cortex, medulla, and renal

pelvis). Alongside DAN, DHA also captured the distribution of most PIs, albeit with the exception of just one compound, PI(44:0)- *m/z* 977.72. Furthermore, when utilizing the CMBT matrix, all but three PIs remained undetected, including PI(40:1)- *m/z* 919.63, PI(36:0)- *m/z* 865.58, and PI(44:0)- *m/z* 977.72. Lastly, when using 9AA as the chemical matrix, the chemical images produced were not as favorable as those achieved with the DAN, DHA, and CMBT matrices. Nevertheless, discernible morphological aspects of the kidney were still observed. More precisely, the diacyl PI molecular species containing FA 20:2, FA 22:6, and FA 22:5, were found to be more abundant around the cortex and medulla regions of the kidney (Fig 2.1, columns O–R). In contrast, PI diacyl chains corresponding to FA 16:0, FA 18:0, FA 18:1, and FA 20:4, were found to be diversely distributed across all regions of the kidney (Fig 2.1, columns D, E, G, L, M, N). Notably, PI(16:0_18:0) in column F showed a pronounced distribution within the medulla, distinct from the surrounding kidney cortex. These observations were consistent among all tested matrices.

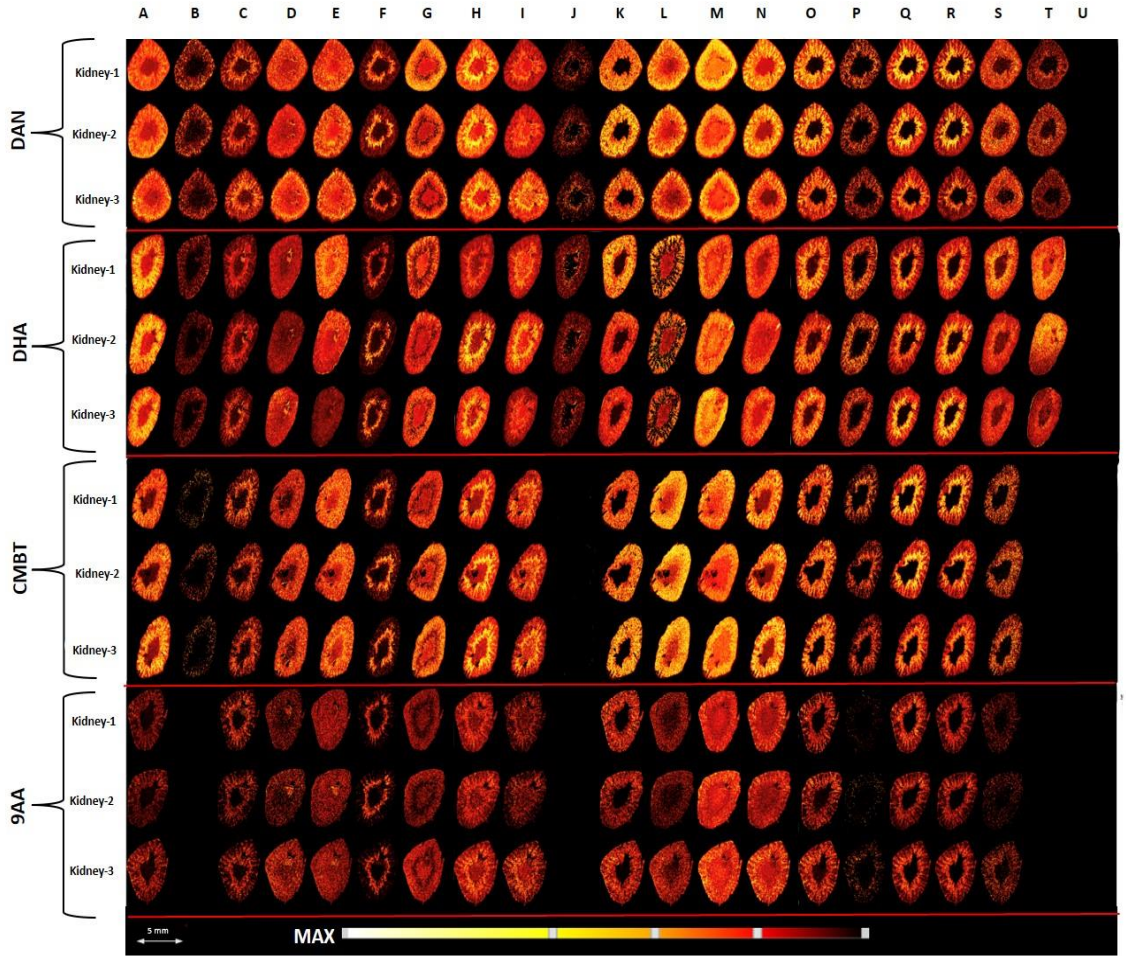


**Figure 2.1** MALDI imaging of transverse kidney section in negative ion polarity (spatial resolution, 50 µm) with 1,5-diaminonaphthalene (DAN), 2,5-dihydroxyacetophenone (DHA), 5-chloro-2-mercaptobenzothiazole (CMBT), and 9-

aminoacridine (9AA), each serving as the unique chemical matrix to detect and visualize phosphatidylinositol species. All technical replicates (ion images) show the detection and spatial distribution of phosphatidylinositol compounds among the tissue surface, showcasing the distinct morphological features of the kidney: cortex, medulla, and pelvis. The PIs from left to right are as follows: **A**, PI(18:0) *m/z* 599.32; **B**, PI(32:1) *m/z* 807.50; **C**, PI(32:0) *m/z* 809.52; **D**, PI(34:2) *m/z* 833.52; **E**, PI(34:1) *m/z* 835.53; **F**, PI(34:0) *m/z* 837.55; **G**, PI(36:4) *m/z* 857.52; **H**, PI(36:2) *m/z* 861.55; **I**, PI(36:1) *m/z* 863.56; **J**, PI(36:0) *m/z* 865.58; **K**, PI(38:6) *m/z* 881.52; **L**, PI(38:5) *m/z* 883.53; **M**, PI(38:4) *m/z* 885.55; **N**, PI(38:3) *m/z* 887.56; **O**, PI(38:2) *m/z* 889.58; **P**, PI(40:7) *m/z* 907.53; **Q**, PI(40:6) *m/z* 909.55; **R**, PI(40:5) *m/z* 911.56; **S**, PI(40:4) *m/z* 913.58; **T**, PI(40:1) *m/z* 919.63; **U**, PI(44:0) *m/z* 977.71. PIs from columns A–O and Q–S, with the exception of PI(36:0) from column J and PI(32:1) from column B, were validated by MS/MS. In contrast, PI(32:1), PI(36:0), PI(40:7), PI(40:1), and PI(44:0) were tentatively identified based solely on mass accuracy. Scale bar, 5 mm.

After evaluating the detection capabilities of the matrices for phosphatidylinositol compounds, the *m/z* distribution of some phosphoinositides was also mapped. PIPs are known to be present in low abundance in tissue, posing a great analytical challenge for their detection using MSI. Thus, the choice of matrix and instrument tuning will have a substantial impact on the results of studies when the molecules of interest are present in low relative abundance. [68] As shown in Figure 2.2, all matrices were able to detect and map the distribution of several PIP compounds, with the exception of 9AA. Notably, the most distinguished mapping corresponds to PIP(18:0_20:4)- *m/z* 965.52, distributed across all regions of the kidney surface. In contrast, the results revealed that the CMBT matrix was able to detect and map two PIP3s: PIP3(38:4)- *m/z* 1125.45 and PIP3(38:3)- *m/z* 1127.46.

While the subcellular distributions of these lipid species have been previously explored [45], the comprehensive distribution of all PIs within the kidney has not been thoroughly addressed in the context of MSI-related literature. This gap presents a unique opportunity for subsequent research specializing in PIs and PIPs. By employing MALDI-MSI, we have mapped a large number of these lipid species within the kidney, providing an unprecedented and detailed molecular map of these compounds.

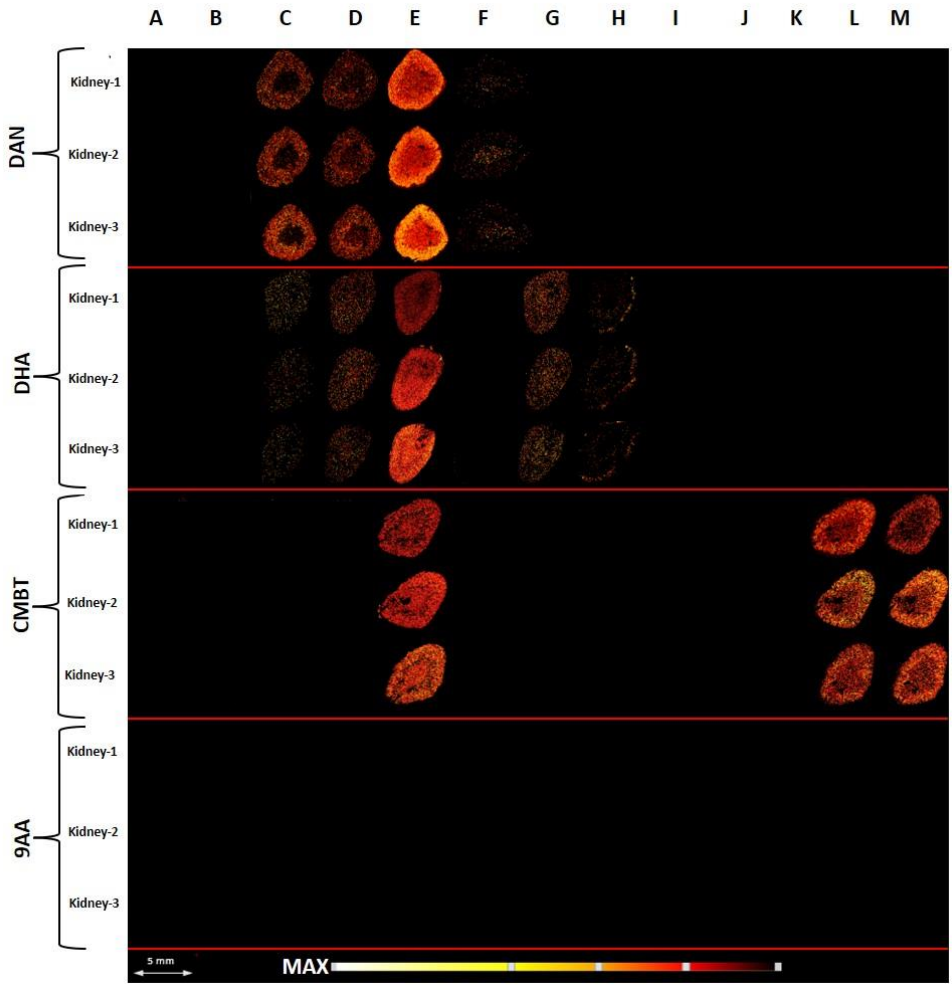


**Figure 2.2** MALDI imaging of transverse kidney section in negative ion polarity (spatial resolution, 50 µm) with 1,5-diaminonaphthalene (DAN), 2,5-dihydroxyacetophenone (DHA), 5-chloro-2-mercaptobenzothiazole (CMBT), and 9-aminoacridine (9AA), each serving as the unique chemical matrix to detect and visualize phosphoinositide species, including PIP, PIP2, and PIP3. All technical replicates (ion images) show the detection and the spatial distribution of PIPs among the tissue surface, showcasing the distinct morphological features of the kidney: cortex, medulla, and pelvis. The PIPs from left to right are as follows: **A**, PIP(34:1) *m/z* 887.47; **B**, PIP(34:2) *m/z* 913.48; **C**, PIP(34:1) *m/z* 915.50; **D**, PIP(36:2) *m/z* 941.52; **E**, PIP(18:0_20:4) *m/z* 965.52; **F**, PIP2(36:2) *m/z* 1021.48; **G**, PIP2(36:1) *m/z* 1023.50; **H**, PIP2(38:4) *m/z* 1045.48; **I**, PIP2(34:1) *m/z* 1075.43; **J**, PIP3(36:2) *m/z* 1101.44; **K**, PIP3(36:1) *m/z* 1103.46; **L**, PIP3(38:4) *m/z* 1125.45; **M**, PIP3(38:3) *m/z* 1127.46. Of all detected PIPs, PIP(18:0_20:4) was validated with MS/MS, whereas all other phosphoinositide species were tentatively identified by mass accuracy. Scale bar, 5 mm.

## Signal intensity and lipid coverage

Parallel to analyzing the distributions of both PIs and PIPs, the signal intensities and lipid coverage for each matrix were evaluated. Spectra for all datasets (full scan; Fig. S4, and product ion scan modes) and signal-to-noise ratios (S/N) for the observed signals are contained in Appendix A (Table S1). As demonstrated in Figure 2.3a, both DAN and DHA matrices exhibited

intense signals for PIs. While both matrices performed well, DHA exhibited a notably higher average intensity of 9.2E5 for PIs, compared to 7.9E5 for DAN, indicating a significant edge in detection capability. Nonetheless, both chemical matrices of DAN and DHA at their given thicknesses are suitable for the analysis of PIs, producing the strongest signals for these compounds, as exemplified in the chemical images. Moreover, among all detected PIPs, DAN was capable of producing high-intensity peaks for PIP compounds, outperforming all other matrices. Additionally, DHA provided the highest intensity for PIP2 compounds, while CMBT was unique in providing signals from PIP3, a feature not observed in DAN, DHA, and 9AA. However, due to the faint signal from these peaks, from both PIP2 and PIP3, conducting on tissue tandem-MS was problematic. As a consequence, we could not assert with confidence that these particular compounds are genuine and not artifacts. The sole criterion met for identification in this instance was mass accuracy, thus making the identification of these compounds tentative. Alternatively, a variety of the PIs and a single PIP compound were identified based on both mass accuracy and their characteristic fragmentation pattern, as reported in Appendix A, highlighting their fatty acyl chains and inositol phosphate head group.

Regarding lipid coverage (Figure 2.3b), four donut charts were generated, each representing the distribution of captured phosphatidylinositol species—PI, PIP, PIP2, and PIP3—by each chemical matrix. Each chart corresponds to one particular species and the segments within the chart represent the proportion (amount) of that species detected by the different matrices. As a result, both DAN and DHA matrices stood out prominently. They exhibited superior detection capabilities, identifying an impressive range of phosphatidylinositol species. Specifically, they both detected an equal amount of the listed phosphatidylinositol compounds, when compared to the other matrices. Moreover, DAN and DHA were proficient in recognizing 4 and 5 PIPs, respectively. In comparison, while CMBT also showcased exceptional performance by identifying an impressive range of PIs, it particularly shone in detecting 2 PIP3 compounds. Lastly, 9AA detected the fewest of both PIs and PIPs, with 17 and 0 compounds detected, respectively. Given these results, each matrix has unique lipid coverage. It is evident that DAN and DHA serve as strong candidates for broad lipid detection capability, especially for PIs. Conversely, CMBT demonstrates a notable potential for the targeted detection of PIP3 compounds. However, taking into account the total heterogeneity in PIs and PIPs detected by

these matrices, DHA had a slight edge in encompassing a more comprehensive range of phosphatidylinositol species, with a total of 25 lipids, followed by DAN (24 lipids), CMBT (21 lipids), and lastly 9AA (17 lipids).

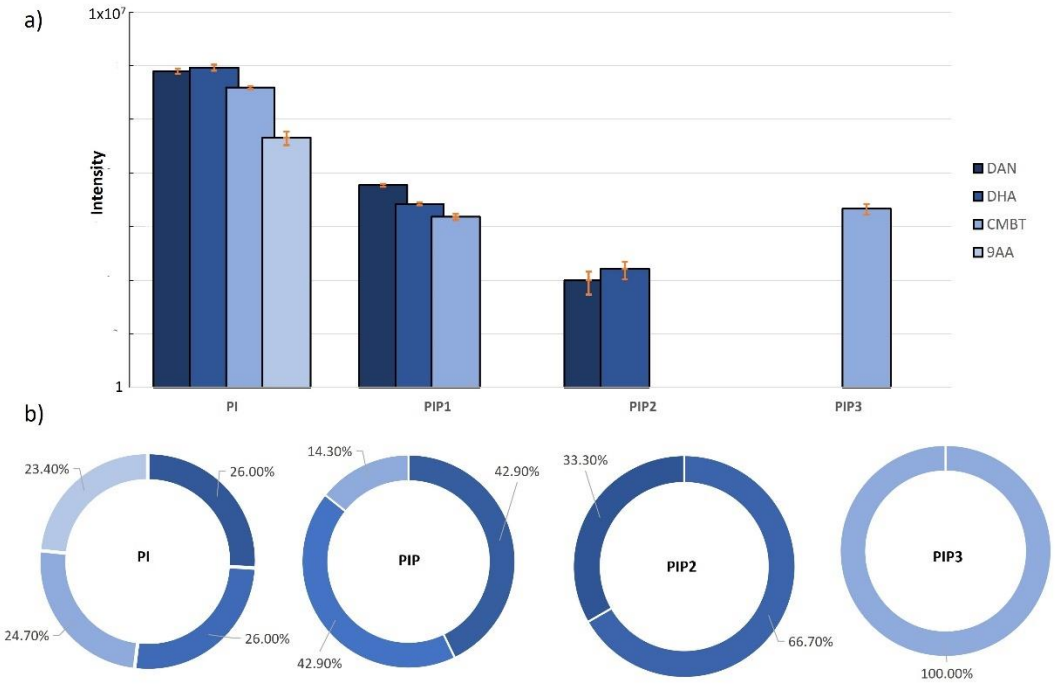


**Figure 2.3** Signal intensities and lipid coverage of phosphatidylinositols (PIs) and phosphoinositides (PIP, PIP2, PIP3) generated as a result of MALDI-MSI from the following matrices: DAN, DHA, CMBT, and 9AA. **a** Bar graph illustrating the average signal intensities of PIs and PIPs acquired with various matrices (error bars represent the standard deviation of triplicates). **b** Donut charts illustrating the percentage (amount) of lipid species captured by each chemical matrix.

Based on these findings, DHA and DAN demonstrate greater sensitivity for PI, PIP, and PIP2 compounds, showing potential for achieving comprehensive phosphatidylinositol mapping. However, depending on the goal and depth of the analysis, an important consideration is the spatial resolution of which the acquisition is performed. DHA is well-known for its instability and rapid sublimation under vacuum conditions, presenting challenges to operate with this matrix. Previous studies have reported that using DHA as the MALDI matrix for long-duration MSI applications, such as high-resolution MSI analysis, was unsuccessful due to matrix evaporation during the analysis, resulting in inadequate matrix compounds remaining on the sample for effective analyte desorption and ionization. [56, 68] Hence, DAN emerges as a more suitable fit for the analysis of these compounds when employing high spatial resolution experiments

**PI and PIP detectability in MALDI-MS**

While the matrix type does play a fundamental role in the degree of ionization, the chemical structure of certain analytes greatly influences its detectability by MALDI-MS. Hence, an additional factor to consider in this context is the detectability of these lipid species. As previously established in literature, the detection limits of phosphoinositides increase based on three factors: (1) the detectability of these lipid species decreases as their molecular weight increases; (2) it decreases with the charge states; and (3) it is further reduced in complex biological matrices containing lipid mixtures, which cause ion suppression, particularly by phosphatidylcholine. [59] The poor ionization efficiency of high molecular weight compounds (PIPs) could be attributed to their difficulty in desorbing from the sample surface. Furthermore, one could argue with the charge state of these compounds, as the production of higher charged molecular ions may lead to observed molecular weights that are half or a third of the anticipated values. Typically, at physiological pH levels (pH = 7.4), phosphatidylinositols bear one negative charge, but additional phosphates at the inositol ring lead to higher negative charges for PIP ($z = -3$), PIP2 ($z = -5$), and PIP3 ($z = -7$). [59] Although it seems possible to observe these compounds in the lower *m/z* range, given their possibility of being doubly or even triply charged, the formation of singly charged ions is still highly favored. This is attributed to the weaker intensity of the higher charged state species, with singly charged ions predominating. Alternatively, charge compensation of the corresponding negative charges found on phosphoinositides results in singly charged species. [59] Nevertheless, given these points, achieving reliable and sensitive detection of phosphoinositides in complex biological contexts, such as tissues, presents a significant challenge.

**2.4 Conclusions**

In conclusion, this study demonstrates the selection of different matrices for the enhanced detection of PIs and PIPs in mouse kidney tissues using MALDI-MSI. Among the matrices evaluated, DAN, DHA, and CMBT were notable for producing high-intensity peaks of PIs in kidney sections, whereas 9AA generated lower-intensity peaks. Although detecting some low-abundant phosphoinositides posed challenges, it was achievable with DAN, DHA, and CMBT. The fine-tuning of these chemical matrices, particularly DHA and DAN, provides valuable insights for future phosphoinositide research, facilitating pathology studies and providing a comprehensive detection of PIs and their phosphorylated forms. In addition, the detailed molecular map of these species obtained

in this study not only sheds light on the normal physiological state of the kidney but also serves as a foundational reference for identifying pathological alterations. Such insights are invaluable for advancing our understanding of kidney-related diseases, where elevated concentrations of PIs could serve as a biochemical indicator for malignant transformation. This is particularly relevant in the context of renal pathology, where the high complexity and heterogeneity associated with glomerular diseases present challenges, such as in human papillary renal cell carcinoma (RCC). [70, 71]

While our research underscores the importance of matrix optimization, we found that this alone is insufficient for a comprehensive analysis of PIPs. Further specialized methods or protocols are required to significantly enrich the selectivity and sensitivity of MALDI-MSI. As such, in addition to other types of organic matrices, metallic and carbon-based nanoparticles should be investigated as a MALDI matrix. [72] Sample derivatization may also offer new paths to overcome current analytical challenges and enhance the capabilities of phosphoinositide research.

# Chapter three: Determination of the internal energy distributions of various MALDI matrices: Implications for the direct analysis of phosphatidylinositol-3,4,5-triphosphate

Laurentiu G. Dabija, Rai Xi Chen, Alan C. Hopkinson, Demian R. Ifa

## 3.1 Abstract

Phosphoinositides, derivates of phosphatidylinositols, are a subclass of phospholipids essential for various cellular processes in both healthy and diseased states. Among the types of phosphoinositides, phosphatidylinositol-3,4,5-triphosphate with arachidonic and stearoyl fatty acyl side chains functions as a key lipid intermediate for cellular processes. Currently, there is a lack of literature regarding the reliable detection and validation of phosphatidylinositol triphosphate on tissue surfaces with matrix-assisted laser desorption/ionization mass spectrometry imaging techniques. Consequently, our study aims to investigate the potential cause(s) behind the poor analytical characterization of this phospholipid, hypothesizing that in-source fragmentation and the sparse abundance contribute to undesirable identification and, thus, validation. Addressing this, we employed the survival yield method to determine the internal energy distribution of each assessed matrix and inquire into the complex matrix-analyte interplay. In addition, we revisited the limit-of-detection, identifying unique detectability limits tailored to each matrix. Ultimately, our results indicate that the poor detectability (high detection limits) of phosphatidylinositol triphosphate is due to in-source fragmentation processes that occur within the MALDI environment. We investigated the fragmentation energies of both multiply-charged and singly charged multi-phosphorylated head groups using density functional theory calculations.

## 3.2 Introduction

Phosphoinositides (PIPs), also known as phosphatidylinositol phosphates, are a family of phospholipids that are obtained through the phosphorylation at positions 3, 4, or 5, of the inositol ring headgroup of phosphatidylinositol (PIs) species. [72] The partial or full phosphorylation generates three major subgroups of PIPs: phosphatidylinositol monophosphate (PIP), phosphatidylinositol biphosphate (PIP2), and phosphatidylinositol triphosphate (PIP3). Among the PIPs, PIP3 plays a critical role in cellular functions. [73] It serves as a secondary messenger that interacts with a diverse array of proteins. The localization and activation of these effector proteins regulate a wide range of cellular processes, including cell survival, proliferation, cytoskeletal rearrangement, and gene expression. [72][73] As such, given its central role in cellular signaling and its implications in numerous diseases [73], the study of PIP3 metabolism and function remains an important area of investigation in biological research.

Among the various analytical techniques employed for the analysis of PIPs, mass spectrometry (MS), particularly liquid chromatography-mass spectrometry (LC-MS), is recognized as the gold standard for the precise detection and quantification of this lipid class. [74] Currently, numerous studies utilize LC-MS in the exploration of PIPs in both cells and biological tissues. A pivotal contribution by Clark et al. pioneered the utilization of a methylation reaction involving (trimethylsilyl (TMS))diazomethane [75], effectively enhancing the detectability of PIPs. Their methodology was subsequently adopted by various studies. [76-78]

Despite LC-MS and its efficacy in detecting and quantifying PIP3 and its respective counterparts, mass spectrometry imaging (MSI) could offer several advantages over this traditional method. As mentioned, most studies utilize TMS-diazomethane to derivatize the PIPs in LC-MS. However, this can introduce complexities such as side reactions and sample degradation and poses major health risks due to its high toxicity. [79] Conversely, MSI, particularly matrix-assisted laser desorption/ionization mass spectrometry imaging (MALDI-MSI), has emerged as a robust technique among various MSI methods. MALDI-MSI has the ability to detect hundreds to thousands of ions simultaneously in a single experiment in situ, including proteins, peptides, lipids, metabolites, and pharmaceuticals. [80] However, challenges persist in analyzing PIPs, particularly PIP3. To our knowledge, no reports in the literature have addressed the detection and validation of PIP3 via tandem-MS (MS/MS) in biological tissues using MALDI-MS. In our previous publication, we investigated different chemical matrices to enhance the detectability of PIPs, identifying 2,5-dihydroxyacetophenone and 1,5-diaminonapthalene as promising candidates. [81] However, as noted in Chapter 2 of this thesis, issues arise as the phosphorylation state of these compounds increases, leading to insufficient signal intensity and low signal-to-noise ratio (S/N) of these species.

These challenges suggest two possible explanations. Firstly, the negatively charged phosphate groups of PIP3 could contribute to in-source fragmentation (ISF), a phenomenon that may be exacerbated by the high-energy conditions of MALDI. The internal energy of ions generally dictates their propensity to fragment, indicating that the full scan mass spectrum reflects the internal energy acquired during the ionization process. [39] Thus, to explore this hypothesis, we will employ the ‘survival yield’ (SY) method, a modified version of the thermometer ion method, based on the work of De Pauw et al. [82]. This method utilizes compounds with simple

and well-known dissociation patterns, known as thermometer ions, to investigate the energy uptake during the activation process. [39] This has been extensively used to establish the internal energy of ions generated by a wide range of mass spectral techniques, such as MALDI and its variant forms [83-86], desorption electrospray ionization (DESI) [39, 87], and electrospray ionization (ESI) [39, 88-92]. The assumption of this approach is that ions with an internal energy above their critical energy ($E_o$) will undergo dissociation. Conversely, ions with an internal energy below their critical energy will not dissociate. [92] Thus, the survival yield measures the proportion of ions that have an internal energy below the critical energy threshold. This can be determined using equation (1), where I(M - ) and I(F - ) represent the intensities of the molecular ions and fragment ions observed in the mass spectra, respectively. [92] The function SY(E) is defined as the integral of the internal energy distribution function, P(E), throughout the range from $E = 0$ to $E_o$. [86] Hence, the internal energy distribution can be obtained by calculating the first derivative of SY(E). In doing so, a class of negative thermometer ions: phenyl sulfate derivatives, with a well-established fragmentation pattern and well-characterized critical energy values [93], will be used to evaluate the internal energy deposition stemming from this process.

$$\mathrm{SY(E)} = \frac{\mathrm{I(M\text{-})}}{[\mathrm{I(M\text{-})} + \sum I(F-)]} = \int_0^{Eo} \mathrm{P(E)}\, dE \qquad \textbf{(1)}$$

The second consideration pertains to the low concentration of these molecular species. Typically, PIs and PIPs are less prevalent than other phospholipids within cells, as specified in section 1.4 of this thesis, where PIP3 accounts for < 0.05% of total PIPs. [32] However, it is important to note that these levels fluctuate between different organs, in response to external stimuli, as well as the state of the organism (i.e. diseased vs healthy). [32] Nonetheless, this suggests that MALDI may lack the required sensitivity for the direct analysis of PIP3 from biological tissues, accounting for matrix effects and ion suppression. In fact, a study by Muller et al. explored the detection limits of PIP species using MALDI-TOF, establishing a detection limit (LOD) of ~243.6 pmol for PIP3. [59]

Given these considerations, this study aims to determine whether the inability to detect and validate PIP3 in tissue samples is due to the molecule's inherent chemical instability within the MALDI environment, the lack of sensitivity of the technique itself, or a combination of both factors. Therefore, to address both matters, the energetics of the MALDI process will be assessed

by employing the SY method, and in an extension of Muller et al.'s research, the LOD will be revisited using modern and well-established MALDI matrices for the analysis of lipids, particularly phospholipids: 5-chloro-2-mercaptobenzothiazole (CMBT) [48, 61], 1,5-diaminonaphthalene (DAN) [62], 9-aminoacridine (9AA) [94], 2,5-dihydroxyacetophenone (DHA) [95], and Norharmane (NRM) [96].

### 3.3 Experimental

#### Materials and Reagents

All MALDI matrix compounds, including 5-chloro-2-mercaptobenzothiazole (CMBT), 1,5-diaminonaphthalene (DAN), 9-aminoacridine (9AA), 2,5-dihydroxyacetophenone (DHA), Norharmane (NRM), and potassium salts of phenyl sulfate (H-Ph-$OSO_3^-$), 4-nitrophenyl sulfate ($NO_2$-Ph-OSO3$^-$), and 4-methylphenyl sulfate ($CH_3$-Ph-$OSO_3^-$), were acquired from Sigma Aldrich (St. Louis, MO, USA). Additionally, the potassium salt of 7-hydroxycoumarin sulfate (CMR-$OSO_3^-$) was obtained from Toronto Research Chemicals (Toronto, ON, Canada). The ammonium salt of PIP3(18:0/20:4) was purchased from Avanti Polar Lipids. HPLC-grade reagents, including chloroform ($CHCL_3$), methanol (MeOH), and water ($H_2O$), were purchased from Sigma-Aldrich (Oakville, ON, Canada).

#### Sample Preparation

For the SY experiments, pooled solutions of phenyl sulfate (100 µM) were prepared by diluting aqueous stock solutions (250 µM) with a 1:1 (v/v) mixture of MeOH/$H_2O$. These solutions were subsequently combined with each saturated matrix solution—DAN, 9AA, CMBT, NRM, and DHA—in 50% MeOH at a 1:1 ratio, resulting in a final concentration of approximately 50 µM for the phenyl sulfates. The mixed solution was applied as a 2 µL droplet directly onto the target plate and allowed to air dry, aided by a gentle stream of warm air to enhance the homogeneity of crystallization. For the LOD experiments, PIP3 delivered as a powder (100 µg) was dissolved in $CHCl_3$/MeOH (2:1) at a stock solution of 100 µM. Appropriate amounts of lipid stock solution and each saturated matrix solution in pure methanol were mixed in a small glass vial and 2 µL of the resulting mixture was applied onto the target plate and allowed to air dry, with similar conditions as was employed for the SY experiments.

**MALDI-MS analyses**

MALDI-MS experiments were conducted using a QExactive hybrid mass spectrometer (Thermo Fisher Scientific, San Jose, CA, USA) coupled with the Spectroglyph, ESI/MALDI injector (Spectroglyph LLC, Kennewick, WA, USA). Acquisition parameters include a resolving power of 70,000 at *m/z* 200, a maximum injection time of 200 ms; and the *m/z* range was set to 50-300 for the SY experiments and 100-1200 for the LOD experiments, both utilizing negative ion polarity. For all experiments, a laser (Nd:YLF, 349 nm), systematically scanned across a predefined area on the sample surface for each replicate measurement, containing ~ 100 laser pixels. MALDI-MS/MS (Tandem-MS) experiments of PIP3 were conducted using collision-induced dissociation (CID), where ultra-high purity nitrogen (99.999%) served as the collision gas and normalized collision energies (NCE) of 20% were applied.

**SY and density-functional theory (DFT) calculations**

Survival yields (SY) of the phenyl sulfate ions were calculated at each considered laser pulse energy for each matrix, using equation 1. Their mass spectral features, including intact and fragment *m/z*, as well as the dissociation threshold energies, can be found in Table 3.1. Further information regarding their characterization and suitability as thermometer ions, and quantum chemistry calculations, can be found from reference [93]. OriginPro (OriginLab Co., Northampton, MA, USA) was used to fit the sigmoidal curves and differentiate the sigmoidal curves to determine the internal energy distribution and calculate the mean internal energies ($<E_{int}>$), as described by M. Flanigan IV et al [23]. Briefly, the SY values calculated were plotted as a function of laser fluence ($\mu J/mm^2$) to reveal variations of the SY. The data points that were the most dispersed for the four phenyl sulfate ions at a particular laser pulse energy were plotted as a function of their respective critical energies, $E_o$ (Table 3.1). Sigmoidal curves were fit using a Boltzmann function as seen in equation 2, where E represents the center of U, x is $E_o$, and $A_1$ and $A_2$ are the initial and final SY values, respectively. [16]

$$SY(x) = A_2 + \frac{A_1 - A_2}{1 + e^{E - x/dx}} \quad \textbf{(2)}$$

All DFT calculations were carried out using the Gaussian16 software package. Structural parameters (bond lengths, bond angles, and dihedral angles) of the inositol molecules were optimized using the M06-2X functional and a standard Pople Gaussian-type basis set, i.e. at the M06-2X/6-311++G(d,p) level. These structures were further characterized by vibrational analysis to ensure they were at minima (not transition states) on the potential energy surface. All the structures reported here are for the lowest-energy structure (global minimum) of the respective inositol isomers.

**Table 3.1.** Critical dissociation energies and key mass spectral characteristics of phenyl sulfate thermometer ions. The predominant fragmentation pathway is characterized by the loss of $SO_3$.

| Phenyl sulfate ion | Intact mass (*m/z*) | Fragment mass (*m/z*) | $E_o$ (eV)[a] |
|---|---|---|---|
| **H-Ph-$OSO_3^-$** | 172.99 | 93.03 | 2.66 |
| **$CH_3$-Ph-$OSO_3^-$** | 187.00 | 107.04 | 2.68 |
| **$NO_2$-Ph-$OSO_3^-$** | 217.97 | 138.01 | 2.12 |
| **CMR-$OSO_3^-$** | 240.98 | 161.02 | 2.17 |

[a]Taken from reference [93].

### 3.4 Results and Discussion

To investigate the potential for in-source fragmentation, the energetics of several matrices—specifically, DAN, 9AA, CMBT, NRM, and DHA—were analyzed. To ensure the matrix contributes to the ionization process, the effects of laser energy without matrix and just the pooled thermometer ion solution, were first studied. To do so, 2 µL of the thermometer ion solution (250 µM) was spotted and air-dried on the MALDI target plate. Upon laser irradiance, no signals corresponding to the *m/z* of each phenyl sulfate ion were present. Increasing the laser pulse energy did not assist in the desorption and ionization of these compounds. These observations are important, as it shows that the phenyl sulfates lack the ability to absorb UV light, and the incorporation of the matrix facilitates the desorption and ionization in the SY experiments. Therefore, as the generation of ions is indeed assisted by the matrix, initial experiments, as depicted in Figure 3.1, determined the minimum laser pulse energies required to achieve a matrix signal exceeding $1x10^3$ counts while ensuring the detection of intact phenyl sulfate ions. As such, for optimal ionization of both the matrix and thermometer ions with minimal fragmentation, laser pulse energies were determined as 10-11 µJ for 9AA, 5-6 µJ for DHA, DAN, CMBT, and NRM.

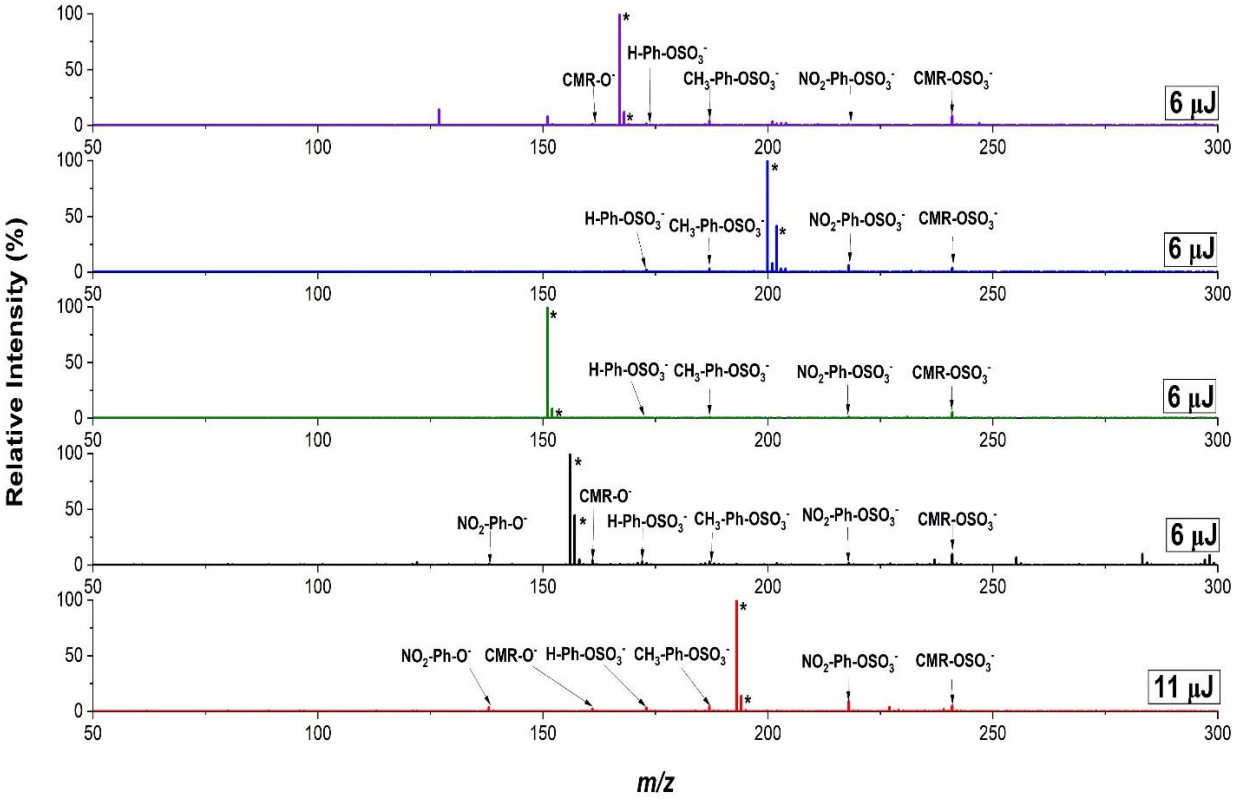


**Figure 3.1.** Representative MALDI mass spectra depicting the optimal ionization conditions for matrices, DAN (black), 9AA (red), DHA (green), CMBT (blue), and NRM (violet), and analytes with minimal fragmentation. Peaks marked with an asterisk (*) denote those originating from the matrix.

We then considered the effects of the matrix at different laser pulse energies, to determine the SY of the thermometer ions (analytes). These measurements allow us to elucidate the energy transfer between the matrix and analyte under varying laser energies, by observing the extent of thermometer ion fragmentation. As expected, incremental increases in laser pulse energy for each matrix revealed notable fragmentation of analytes. Hence, for all matrices, different MALDI thresholds were identified that lead to the greatest fragmentation caused by laser irradiance. As visualized in Figure 3.2, DAN, 9AA, and NRM, have distinct energetic properties and seem to transfer higher amounts of energy to the analytes, even as the laser pulse energy increases. This is particularly evident from the wide range of SY values observed even at the lowest laser pulse energy for phenyl sulfate ion variants, CMR-Ph-$OSO_3^-$ and $NO_2$-Ph-$OSO_3^-$. In contrast, CMBT and DHA, even with increased energy deposition into the matrix, do not transfer extreme amounts of energy to the thermometer ions to exceed their critical energies, and so only minimal fragmentation is observed.

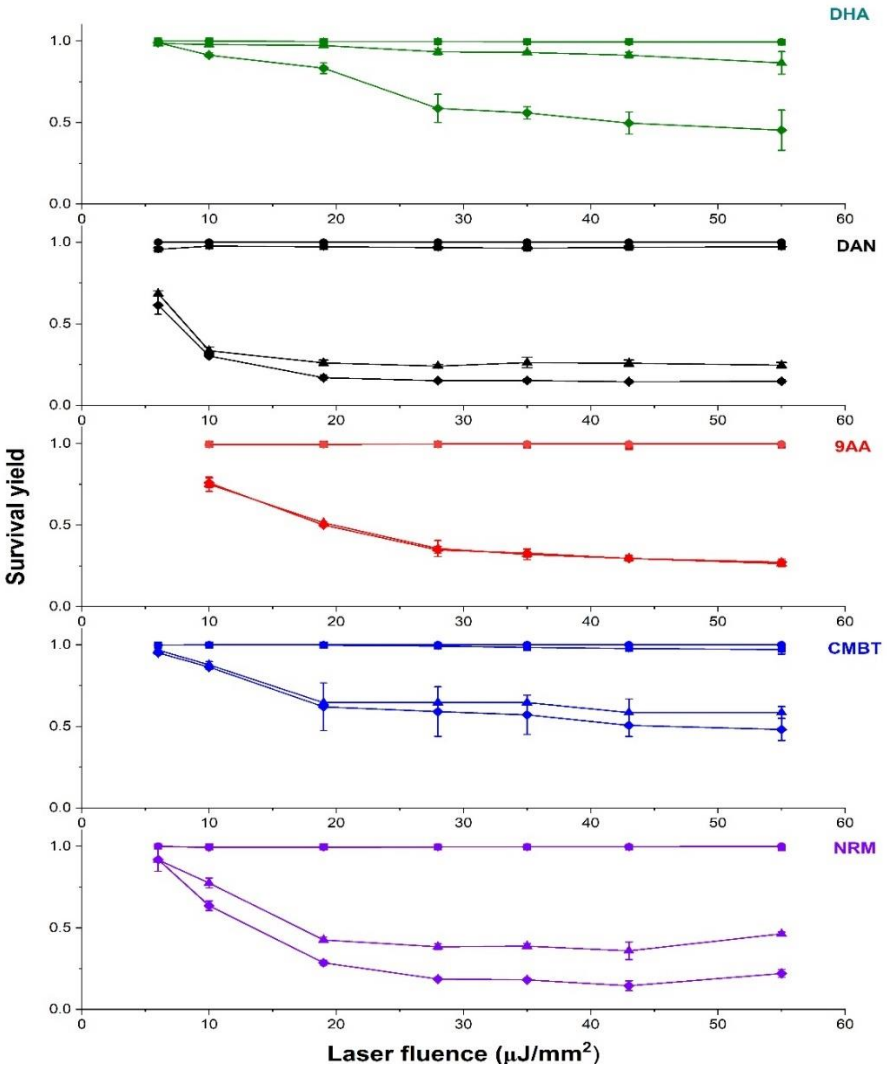


**Figure 3.2.** Variations of the survival yield (SY) of phenyl sulfate ions as a function of laser fluence (μJ/mm$^2$) for each tested MALDI matrix, color-coded as follows: DHA (green), DAN (black), 9AA (red), CMBT (blue), and NRM (violet). Symbols represent different thermometer ions: H-Ph-$OSO_3^-$ (●), $CH_3$-Ph-$OSO_3^-$(■), CMR-$OSO_3^-$ (▲), and $NO_2$-Ph-$OSO_3^-$ (♦). Error bars represent the standard deviation of the triplicates. Note, for clarity purposes, not all error bars are drawn**.**

To determine the internal energy distribution, P(E), the SY values that were spread out the most across each matrix were plotted against the critical energy, $E_o$, for each phenyl sulfate ion (Figure 3.3. a). Applying a laser pulse energy between 20-60 μJ to most matrices produced a well-spread series of survival yields, with each thermometer ion correctly ranked based on their respective critical energies. Hence, for a relevant comparison, the SY values that initially provided the most spread distribution for the phenyl sulfate ions across all matrices were used, which was at ~ 20 μJ. By applying the first derivative to these sigmoidal curves, the internal energy profiles

for each matrix were elucidated (Figure 3.3. b). Notably, both CMBT and DHA had calculated mean internal energies of 2.05 ± 0.182 eV and 2.08 ± 0.020 eV, respectively. In comparison, DAN, 9AA, and NRM, demonstrated slightly higher energy transfer capabilities, relative to CMBT and DHA, with mean internal energies found as 2.26 ± 0.019 eV, 2.14 ± 0.008 eV, and 2.18 ± 0.0169 eV, respectively. As such, with the current conditions employed, the matrices ranked from 'hot' to 'cold' are as shown: DAN, NRM, 9AA, DHA, and CMBT.

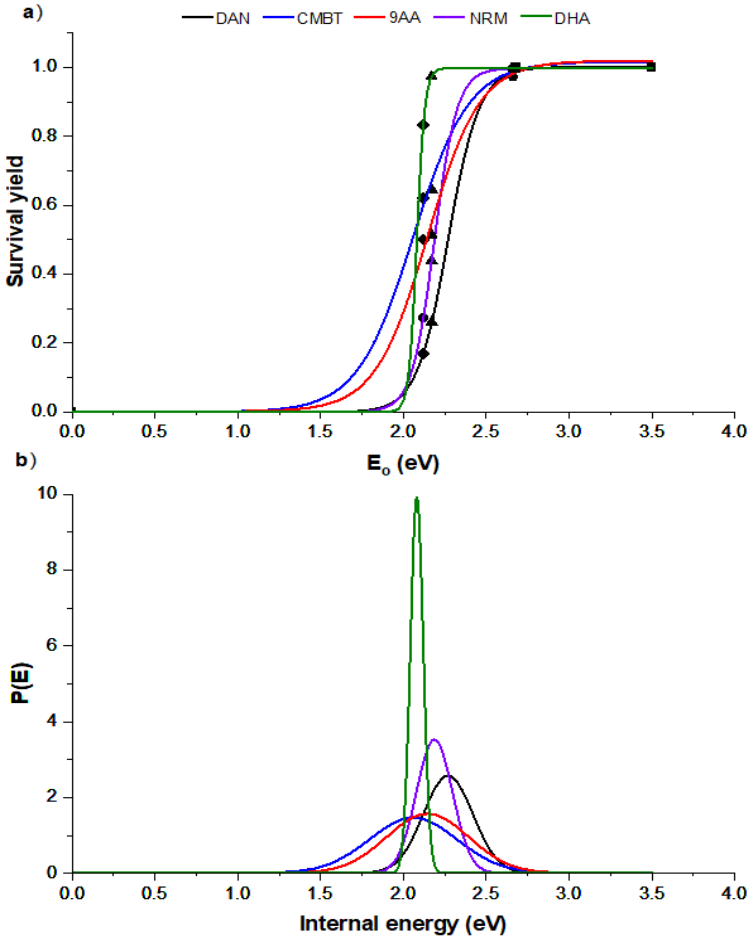


**Figure 3.3.** Internal energy deposition of MALDI in the negative ion polarity across various chemical matrices. (a) Calculated breakdown curves representing the SY values of each thermometer ion (H-Ph-$OSO_3^-$ (●), $CH_3$-Ph-$OSO_3^-$ (■), CMR-$OSO_3^-$ (▲), and $NO_2$-Ph-$OSO_3^-$ (♦)) at ~ 20 µJ for each matrix and plotted as a function of their respective critical energy, $E_o$. The derivatives of the sigmoidal curves produced the (b) internal energy distributions, P(E), for each matrix.

With this determination, we evaluated the ability to analyze PIP3 with each matrix, determining the LOD. The amount of laser energy applied for the LOD experiments was the same laser energy required to produce intact thermometer ions: ~ 6 uJ for DAN, DHA, NRM, and

CMBT, and ~ 11 uJ for 9AA. Of all the five tested matrices, DAN, CMBT, 9AA, and NRM detected PIP3. DHA failed to provide any signal corresponding to PIP3. Attempts were made by increasing the laser pulse energy, however, no signal corresponding to $[PIP3\text{-}H]^-$ at *m/z* 1125.45, was observed. Nevertheless, Figure 3.4 shows that DAN produced the best S/N of PIP3, outperforming all other tested matrices. As summarized in Table 3.2, the LOD was determined based on a set threshold of S/N = 5. The LOD for PIP3 using DAN was approximately 26.84 pmol, compared to NRM and CMBT, which had LODs of around 40.54 pmol and 38.67 pmol, respectively. The lowest being 9AA at 49.72 pmol. DAN, while not by much, demonstrated itself as the most efficient in the ionization of PIP3, with a slightly lower detection limit (better detectability).

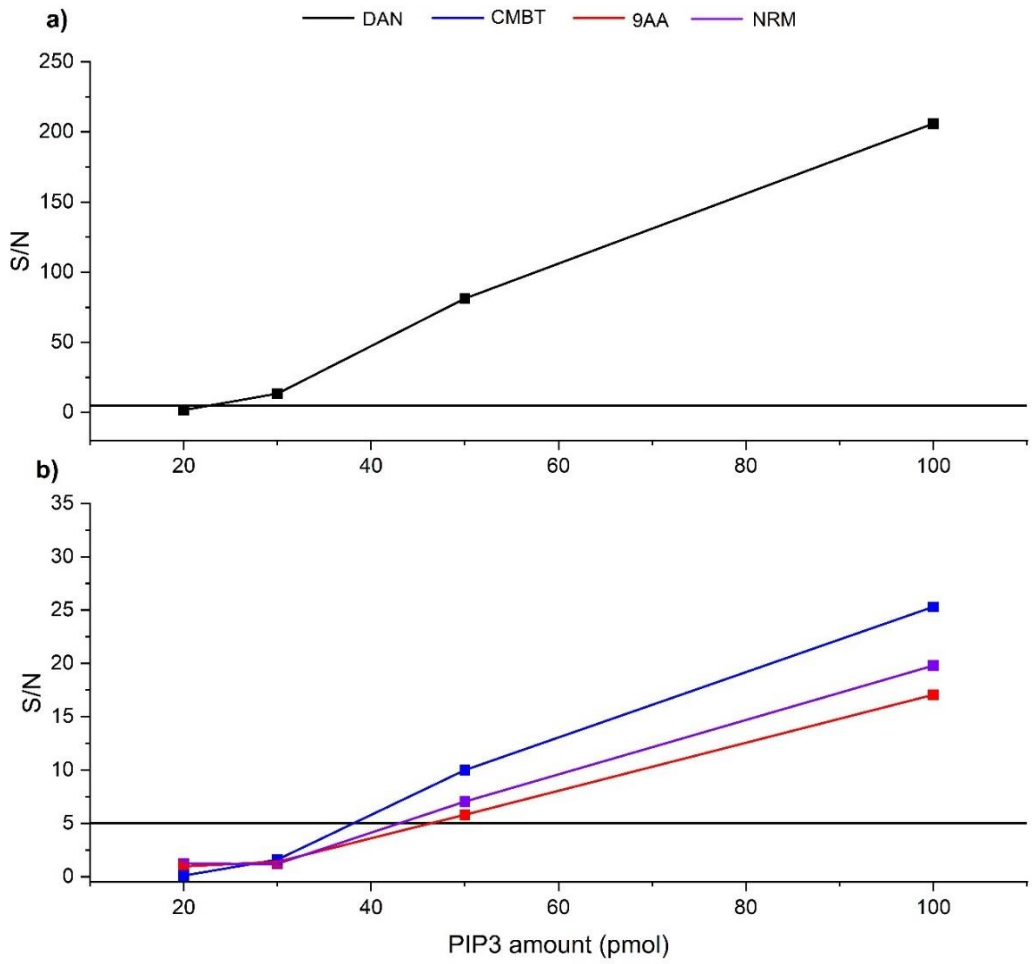


**Figure 3.4.** Signal-to-noise ratio (S/N) as a function of PIP3(18:0/20:4) amount (pmol) on the target plate for MALDI-MS, using the following matrices: (A) DAN, (B) CMBT, 9AA, and NRM.

**Table 3.2**. Detection thresholds and survival yields (SY) for PIP3(18:0/20:4).

| MALDI matrix | Detection limit, threshold (S/N = 5) | SY (%) |
|---|---|---|
| **DAN** | 26.84 pmol | 84 |
| **CMBT** | 38.67 pmol | 70 |
| **9AA** | 49.72 pmol | 35 |
| **NRM** | 40.54 pmol | 100 |

We then turned our attention to examining if there is a correlation between the previously assessed energetics of each matrix and the poor detectability of this lipid species. Notably, ISF of PIP3 was observed by all matrices, with the exception of NRM. Full scan mass spectra indicated three key fragment ions that have the same *m/z* values as $[PIP2\text{-}H]^-$ at *m/z* 1045.48, $[PIP\text{-}H]^-$ at *m/z* 965.51, and $[PIP3\text{-}H\text{-}HPO_3\text{-}H_2O]^-$ at *m/z* 1027.47, all within a mass accuracy of ≤ 3 ppm, featuring arachidonoyl and stearoyl fatty acid chain pairs (Figure 3.5). These fragment ions were confirmed via MALDI-MS/MS at NCE 20% (Figure B.1). The identified fragments arise primarily from the loss of $HPO_3$, which, following intramolecular dehydration, leads to a subsequent loss of 98 Da, likely corresponding to a loss of $HPO_3 + H_2O$. Given the nature of ISF, we focused on observing the peaks representing PIP3's fragments postulated to arise from the loss of $HPO_3$ and the combined loss of $HPO_3$ and water. Using this approach, we measured the percentage of intact PIP3 by calculating the SY. The intensity of the parent ion, $[PIP3\text{-}H]^-$, was used along with the sum of the intensities of the fragment ions, $[PIP\text{-}H]^-$, $[PIP2\text{-}H]^-$, and $[PIP3\text{-}H\text{-}HPO_3\text{-}H_2O]^-$ in equation (1). To our surprise, the SY of $[PIP3\text{-}H]^-$ with DAN was higher than with 'colder' matrices such as CMBT (Table 3.2), suggesting the intact form of PIP3 was preserved more, even though the SY data indicated that DAN was the most energetic ($\langle E_{int} \rangle$ 2.26 eV). In this context, it was actually 'softer'. However, it is important to note that values of the internal energy may differ from the absolute values as the influence of kinetic factors was not taken into consideration.

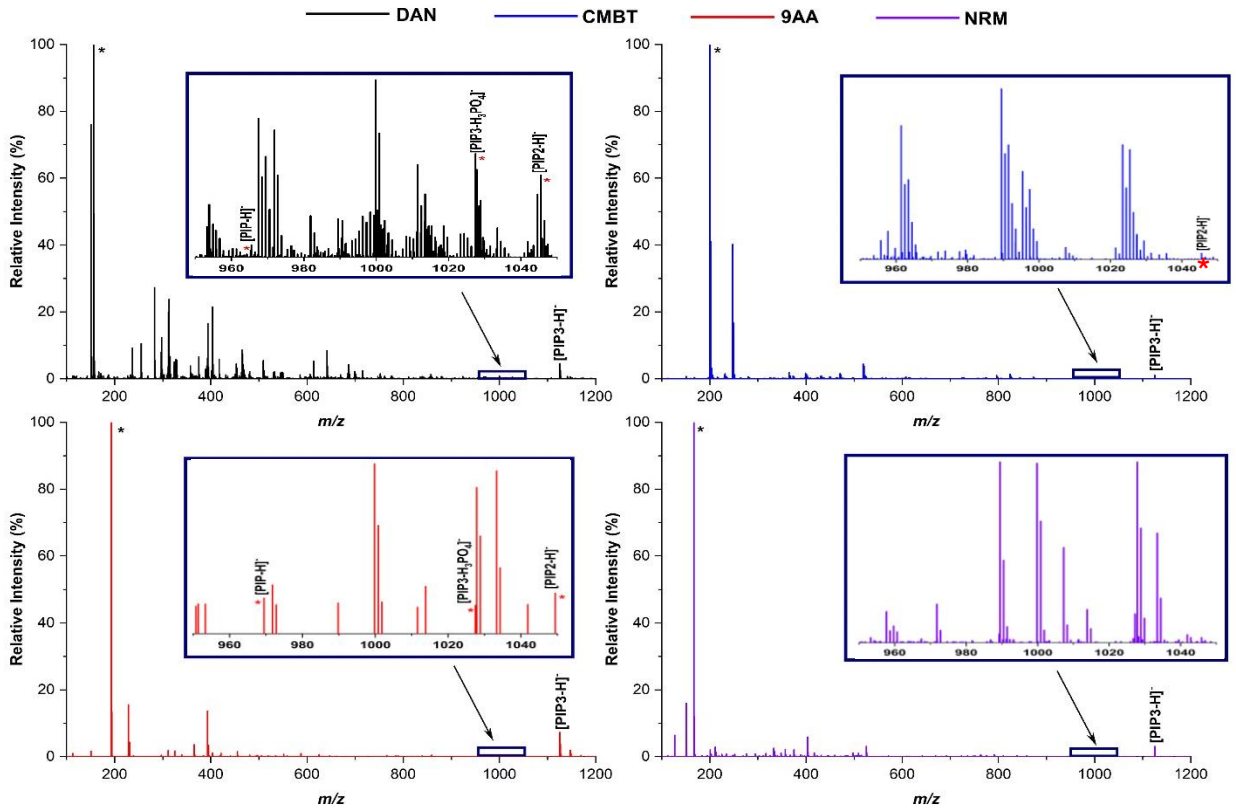


**Figure 3.5.** MALDI mass spectra of $[PIP3-H]^-$ and its respective fragments, $[PIP2-H]^-$ and [PIP-H]; due to the primary loss of $HPO_3$. Peaks marked with an asterisk (*) denote those originating from the matrix, while peaks with a red asterisk represent the fragment ions.

The high detection limit could be attributed to the poor crystallization and subsequent desorption/ionization of PIP3. Additionally, 9AA seemed to induce a higher degree of fragmentation, likely due to the higher pulse energy used. While there is no direct correlation between the energetics of the matrix, as determined by the SY method, and the extent of energy transferred to the analyte, it is evident that each chemical matrix transfers a notable amount of energy to induce fragmentation. This may very well be a contributing factor for the poor detectability of this lipid, with the ISF causing a decline in signal intensity of the parent ion. Nevertheless, the overall LOD and S/N of DAN were superior to those of the other three tested matrices. This improvement may not only be attributed to the SY of (PIP3) but also to external factors, possibly due to the co-crystallization between PIP3 and the matrix. DAN is characterized by fast crystallization kinetics [97], which, with higher evaporation rates, leads to the formation of smaller crystals. Smaller crystals of the matrix typically result in better co-crystallization with the analyte and, thus, better desorption and subsequent ionization.

Moreover, to facilitate an understanding of the energetics required to induce such fragmentation—based on the observed trend with the primary loss of $HPO_3$—the fragmentation mechanism of the inositol(1,3,4,5)tetraphosphate system (IP4), the headgroup of PIP3, was investigated using DFT calculations. To economise on the computational time, a methyl group was used to mimic the long fatty acyl chains. Figures 3.6 and 3.7 display the mechanism leading to the loss of $PO_3^-$ and $HPO_3$ from the multiple-charged and singly-charged inositol anions, respectively. IP4 bears four phosphoric acid residues located at positions 1, 3, 4, and 5, where each phosphoric acid monoester possesses a strongly acidic proton. MALDI typically generates singly charged species, and no observable peaks corresponding to the doubly or triply charged form of PIP3 were found in the mass spectra. This absence of more highly-charged anions can be understood by examining the energetics for the loss of phosphate anion from the multiply charged anions. Thus, calculations reveal that each phosphate group bears a single negative charge in the minimum energy conformation of $[IP_4\text{-}4H]^{4-}$ (Figure 3.6). The loss of $PO_3^-$ from the quadruply charged IP4 is calculated to be exothermic by 450.7 kJ $mol^{-1}$ when the loss is from the 4-position. Loss of a second phosphate anion, this time from the 3-position, gives PIP2 with the 1,5-biphosphate structure; likewise, the phosphate anion loss is exothermic by 213.9 kJ $mol^{-1}$. Removal of the third phosphate anion requires only 34.4 kJ $mol^{-1}$, and the product, PIP, is analogous to the monoanions seen in our MALDI experiments. As a result, the products of $[IP4\text{-}4H]^{-4}$ are energetically more favourable, with each system moving to a lower energy state and becoming increasingly more stable than the original, intact ion. These relative stabilities illustrate why the isolation of a highly charged multi-phosphorylated anion is often difficult to achieve.

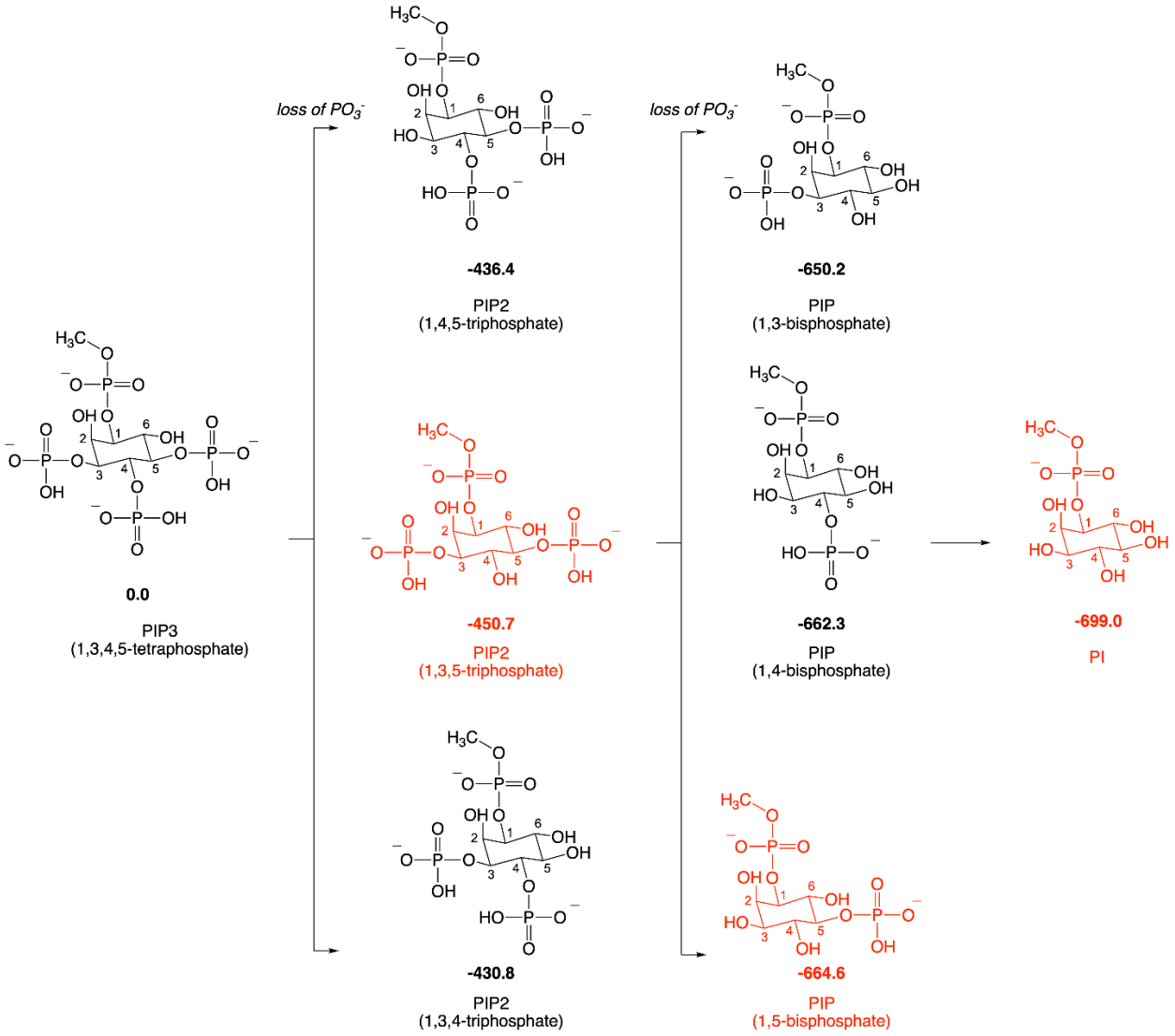


**Figure 3.6**. Fragmentation processes of $[IP4\text{-}4H]^{4-}$. Energies are in kJ/mol.

In the experimental multi-phosphorylated anions, none were observed, and these are stable to the loss of $HPO_3$. Hence, parallel to studying the dissociation energies of $[IP4\text{-}4H]^{-4}$, calculations also reveal a mono-charged system of IP4, represented as $[IP4\text{-}H]^-$ (Figure 3.7). The loss of neutral $HPO_3$ molecule from the mono-negatively charged PIP3 is endothermic. Upon fragmentation, the first loss of $HPO_3$ results in PIP2 structures which possess comparable energies (250.1 – 256.4 kJ $mol^{-1}$), regardless of the position of the $HPO_3$ molecule being lost. It is worth noting that the energy difference for further loss of $HPO_3$ molecules to produce mono-negative PIP and PI are also in a similar range (~250 kJ $mol^{-1}$) in each dissociation reaction. As such, depending on the energetics of the system and conditions employed, this can lead to consecutive losses of $HPO_3$ to yield $[IP2\text{-}H]^-$, headgroup of PIP, and $[IP\text{-}H]^-$, headgroup of PI. Therefore, careful consideration should be

taken when interpreting the mass spectral results for the analysis of PIPs. As the fatty acyl chains remain the same, it is evident that fragmentation of $[PIP3\text{-}H]^-$ generates fragment ions that correspond to the same *m/z* values of $[PIP2\text{-}H]^-$ and $[PIP\text{-}H]^-$, contributing to the misinterpretation of the mass spectra.

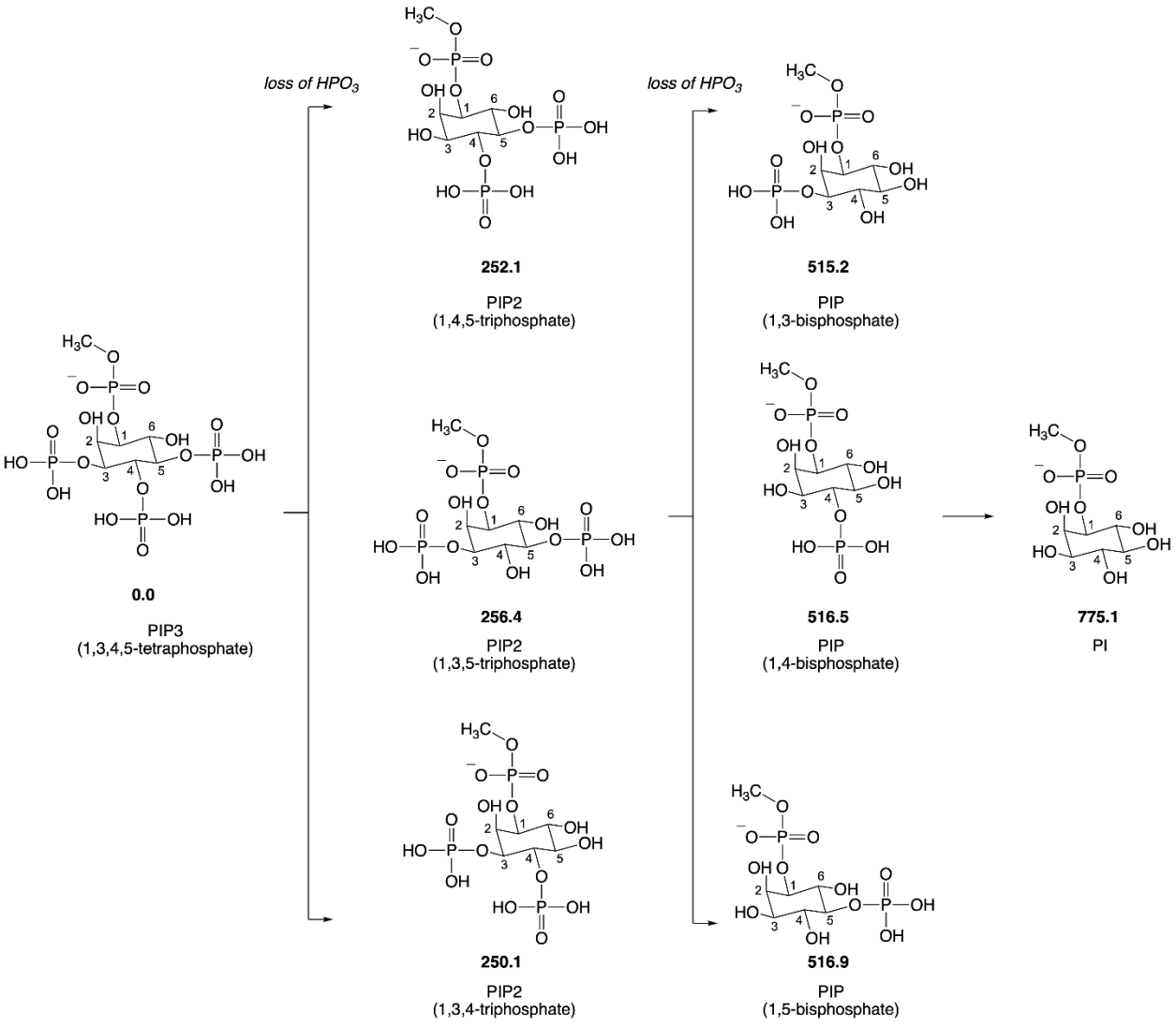


**Figure 3.7**. Fragmentation processes of $[IP4\text{-}H]^-$. Energies are in kJ/mol.

Given the energy differences for the loss of $HPO_3$ from that of PIP3, we focused on comparing this with the IE values calculated by the SY method. On average, the mean IE distribution of each of the assessed matrix corresponds to 145 - 219 kJ/mol, whereas the energies of the dissociation reactions were calculated to be 250.1 – 256.4 kJ/mol, depending on the position of the phosphate. In theory, no fragmentation should have occurred via cleavage of the phosphate

ester bond. However, peaks attributed to the fragment ions are observed in the mass spectra. A possible explanation for this is the underestimation of the mean internal energy values. Previous studies have indicated that analyte ions generated by MALDI, using benzylpyridinium thermometer ions to probe the activation process, exhibited internal energy values around 300 kJ/mol [13]. Hence, other approaches, utilizing the SY method and calculations via the Rice-Ramsperger-Kassel-Marcus (RRKM) theory, which accounts for kinetic factors, could provide a more quantitative measure of the internal energy of MALDI-generated ions.

Furthermore, the underestimation of internal energy could also be due to unaccounted phenomena. For instance, in our experiments, we attributed ISF to the matrix-analyte interplay, specifically the degree of energy transferred from the matrix to the analyte upon laser irradiation. However, collision activation may also occur when ions generated at atmospheric pressure are transferred to a vacuum. [93] This process, known as in-source CID [92, 93], can significantly increase the internal energy of ions. In this context, the Spectroglyph ESI/MALDI injector utilizes a dual ion funnel interface for ion transmission: a high-pressure funnel (HPF) operating at 6-7 torr (on our system), and a low-pressure funnel (LPF) operating at ~ 1 torr. MALDI performed at elevated pressure helps to dampen the internal energy of the ions, preserving the intact form of biologically relevant compounds. Nevertheless, while the pressure difference is small, MALDI-generated ions are accelerated by an electric field at elevated pressure and can collide with residual gas molecules when transported from the HPF to the LPF, causing additional energy transfer beyond that imparted by the matrix. Additionally, depending on the experimental setup, ion dissociation could also occur from collisions with residual gases in the quadrupole, contributing to in-source CID. [93] These factors were unaccounted for and potentially resulted in an underestimation of the mean internal energy values. Therefore, by monitoring the in-source CID, we would be able to measure the internal energy of the ions post-laser irradiation, measuring the impact of both energy transfer from the matrix and collisions occurring with residual gases. However, given the observed fragmentation of $[PIP3-H]^-$, it is probable that the internal energy values for MALDI-generated ions are significantly higher, as previously reported.

### 3.5 Conclusions

In conclusion, this study explored two potential challenges in the detection and validation of PIP3: the higher-energy environment of MALDI, which may lead to ISF and the limited

sensitivity offered by MALDI. In doing so, we monitored the energetic properties of each matrix using the SY method, employing negative thermometer ions to probe the energy transferred from the matrix to the analyte. Additionally, we determined the LOD of PIP3 using the previously assessed matrices. Our findings suggest that the challenges encountered are due to a combination of these two factors. As discussed, depending on the matrix used and experimental conditions set, it is likely the internal energy is higher than the energy required for the loss of phosphate anion ($PO_3^-$) from multiple-charged IP4 and the loss of $HPO_3$ from singly charged IP4.

Finally, the total LOD found among each matrix, ranging from 26-49 pmoles, is approximately 5-10-fold better than the results achieved by Muller et al., who utilized MALDI-TOF and 2,5-dihydroxybenzoic acid as the MALDI matrix. This demonstrates that significant improvements have been made with better technology and well-established matrices. Regardless, the overall LOD still remains high with all MALDI matrices, given that no biological matrices were incorporated. When biological samples, such as tissue are introduced, a significant reduction in the S/N and detectability is expected. Due to the already low abundance of PIP3 and the risk of ISF, the likelihood of reliably detecting and mapping PIP3 on biological tissue surfaces using MALDI-MSI is slim. Potential strategies to overcome these challenges include removing the negative charges from the phosphate moieties, through in situ chemical derivatization, to enhance both detectability and analytical characterization of this lipid. Alternatively, exploring other organic matrices, such as N-(1-naphthyl)ethylenediamine dihydrochloride (NEDC) [98], may also offer improvement.

# Chapter Four: Conclusion and Future Work

This thesis provided a comprehensive exploration of PIs and PIPs using MALDI-MSI. Given the complexity and low abundance of these lipid species, optimizing analytical methods was crucial. As such, Chapter 2 focused on the systematic assessment and optimization of different MALDI matrices for detecting PIs and PIPs in mouse kidney tissue. Through extensive testing of four matrices (DAN, DHA, CMBT, and 9AA), the study identified DAN and DHA as the most effective for achieving high signal intensity and comprehensive coverage of PIs and PIPs, while CMBT showed potential capabilities for detecting specific PIP3 compounds. This chapter established key methodologies for matrix selection and deposition, demonstrating the critical role of optimized parameters in enhancing the sensitivity and accuracy of lipidomic analyses. These findings lay a solid foundation for future MSI research and provide a valuable resource for the MSI community.

While this work underscores the importance of matrix optimization, Chapter 3 explored the energy uptake process in MALDI and examined the internal energy distributions of the previously assessed matrices. By characterizing survival yields, this chapter provided new insights into the behaviour of PIP3 under various ionization conditions. The use of internal energy measurements allowed for a deeper understanding of ISF.

Overall, the findings establish a robust framework for future lipidomic MSI-studies, emphasizing the importance of matrix selection and deposition techniques in enhancing the detection of PIs and PIPs. By optimizing matrix selection and assessing the limitations of MALDI, future protocols can be refined and developed to facilitate more detailed investigations into the spatial distribution and abundance of PIs and PIPs, central to the pathology of aHUS. In addition, the methods developed here can be extended to other diseases characterized by lipid dysregulation, such as neurodegenerative disorders, cardiovascular diseases, and cancers.

# References


1. Griffiths, J. A Brief History of Mass Spectrometry. *Analytical Chemistry* **2008**, *80* (15), 5678–5683.
2. G. Münzenberg, "Development of mass spectrometers from Thomson and Aston to present," International Journal of Mass Spectrometry, Vols. 349-350, pp. 9-18, 2013.
3. Chhabil Dass. *Fundamentals of Contemporary Mass Spectrometry*; Wiley-Interscience: Hoboken, N.J., 2007.
4. Wu, Jiawen, et al. “Imaging Method by Matrix-Assisted Laser Desorption/Ionization Mass Spectrometry (MALDI-MS) for Tissue or Tumor: A Mini Review.” *Processes*, vol. 10, no. 2, 2022, p. 388.,
5. Agarwal, Princy. “Mass Spectrometry.” *Share and Discover Knowledge on SlideShare*, 22 Oct. 2017.
6. Sharad Medhe. Mass Spectrometry: Detectors Review. Chemical and Biomolecular Engineering. Vol. 3, No. 4, 2018, pp. 51-58.
7. Banerjee, S.; Mazumdar, S. Electrospray Ionization Mass Spectrometry: A Technique to Access the Information beyond the Molecular Weight of the Analyte. *International Journal of Analytical Chemistry* **2012**, *2012*, 1–40.
8. Piehowski, Paul D., et al. “Automated Mass Spectrometry Imaging of over 2000 Proteins from Tissue Sections at 100-Mm Spatial Resolution.” *Nature Communications*, vol. 11, no. 1, 2020.
9. Buchberger, Amanda Rae, et al. “Mass Spectrometry Imaging: A Review of Emerging Advancements and Future Insights.” *Analytical Chemistry*, vol. 90, no. 1, 2017, pp. 240–265.
10. Hoffmann, Edmond De, and Vincent Stroobant. *Mass Spectrometry: Principles and Applications*. J. Wiley, 2007
11. Cornett, Dale S, et al. “MALDI Imaging Mass Spectrometry: Molecular Snapshots of Biochemical Systems.” *Nature Methods*, vol. 4, no. 10, 2007, pp. 828–833., https://doi.org/10.1038/nmeth1094.
12. M.-Z. Huang, S.-C. Cheng, Y.-T. Cho and J. Shiea, "Ambient ionization mass spectrometry: A tutorial," *Analytica Chimica Acta,* vol. 702, no. 1, pp. 1-15, 2011
13. D. Gode and D. A. Volmer, "Lipid imaging by mass spectrometry – a review," *Analyst,* vol. 138, pp. 1289-1315, 2013.
14. Karas, M., et al. “Matrix-Assisted Ultraviolet Laser Desorption of Non-Volatile Compounds.” *International Journal of Mass Spectrometry and Ion Processes*, vol. 78, 1987, pp. 53–68.
15. Tanaka, Koichi, et al. “Protein and Polymer Analyses up To*m/z* 100 000 by Laser Ionization Time-of-Flight Mass Spectrometry.” *Rapid Communications in Mass Spectrometry*, vol. 2, no. 8, 1988, pp. 151–153.
16. Wu, Jiawen, et al. “Imaging Method by Matrix-Assisted Laser Desorption/Ionization Mass Spectrometry (MALDI-MS) for Tissue or Tumor: A Mini Review.” *Processes*, vol. 10, no. 2, 2022, p. 388.

17. Caprioli, R. M.; Farmer, T. B.; Gile, J. Molecular Imaging of Biological Samples: Localization of Peptides and Proteins Using MALDI-TOF MS. *Analytical Chemistry* **1997**, *69* (23), 4751–4760.
18. Moore, J. L.; Charkoftaki, G. A Guide to MALDI Imaging Mass Spectrometry for Tissues. *Journal of proteome research* **2023**, *22* (11), 3401–3417.
19. Patil, A. A.; Chiang, C.-K.; Wen, C.-H.; Peng, W.-P. Forced Dried Droplet Method for MALDI Sample Preparation. *Analytica Chimica Acta* **2018**, *1031,* 128–133. https://doi.org/10.1016/j.aca.2018.05.056.
20. R. Fernández, J. Garate, L. Martín-Saiz, I. Galetich and J. A. Fernández, "Matrix Sublimation Device for MALDI Mass Spectrometry Imaging," Analytical Chemistry, vol. 91, pp. 803-807, 2019.
21. J. A. Hankin, R. M. Barkley and R. C. Murphy, "Sublimation as a Method of Matrix Application for Mass Spectrometric Imaging," Journal of the American Society for Mass Spectrometry, vol. 18, no. 9, pp. 1646-1652, 2007.
22. Mielczarek, P.; Suder, P.; Kret, P.; Tymoteusz Słowik; Ewa Ewa Gibuła-Tarłowska; Jolanta Kotlinska; Igor Kotsan; Bodzoń-Kułakowska, A. MALDI Mass Spectrometry Imaging Sample Preparation with Wet-Interface Matrix Deposition for Lipid Analysis. *Authorea (Authorea)* **2023**.
23. Bodzoń-Kułakowska, A.; Wiesława Młodawska; Mielczarek, P.; Lachowicz, D.; Suder, P.; Marek Smoluch. Mammalian Oocyte Analysis by MALDI MSI with Wet-Interface Matrix Deposition Technique. *Materials* **2023**, *16* (4), 1479–1479.
24. Yousefi-Taemeh, M. *Exploring Selected Modern Mass Spectrometry Techniques in Applied Sciences*; Ph.D. Dissertation, York University, Toronto, Ontario, 2023.
25. Schwamborn, K.; Caprioli, R. M. MALDI Imaging Mass Spectrometry - Painting Molecular Pictures. *Molecular Oncology* **2010**, *4* (6), 529–538.
26. Karas, M.; Krueger, R. Ion Formation in MALDI: The Cluster Ionization Mechanism. *ChemInform* **2003**, *34* (18).
27. Thermo Fisher Scientific. *Exactive Series Operating Manual*; Thermo Fisher Scientific: Bremen, Germany, 2010
28. Belov, M. E.; Ellis, S. R.; Dilillo, M.; Paine, M. R. L.; Danielson, W. F.; Anderson, G. A.; de Graaf, E. L.; Eijkel, G. B.; Heeren, R. M. A.; McDonnell, L. A. Design and Performance of a Novel Interface for Combined Matrix-Assisted Laser Desorption Ionization at Elevated Pressure and Electrospray Ionization with Orbitrap Mass Spectrometry. *Analytical Chemistry* **2017**, *89* (14), 7493–7501.
29. Gerhardtova, I.; Timotej Jankech; Majerova, P.; Juraj Piestansky; Dominika Olesova; Kovac, A.; Jampilek, J. Recent Analytical Methodologies in Lipid Analysis. *International journal of molecular sciences* **2024**, *25* (4), 2249–2249.
30. Dickson, E. J.; Hille, B. Understanding Phosphoinositides: Rare, Dynamic, and Essential Membrane Phospholipids. *Biochemical Journal* **2019**, *476* (1), 1–23.
31. Raghu, P.; Joseph, A.; Krishnan, H.; Singh, P.; Saha, S. Phosphoinositides: Regulators of Nervous System Function in Health and Disease. *Frontiers in Molecular Neuroscience* **2019**, *12*.

32. Lolicato, F.; Nickel, W.; Haucke, V.; Ebner, M. Phosphoinositide Switches in Cell Physiology - from Molecular Mechanisms to Disease. *Journal of Biological Chemistry* **2024**, *300* (3), 105757.
33. Mandal, K. Review of PIP2 in Cellular Signaling, Functions and Diseases. *International Journal of Molecular Sciences* **2020**, *21* (21).
34. Toker, A. Phospholipids | Phosphatidylinositol Bisphosphate and Trisphosphate. *Elsevier eBooks* **2013**, 552–556.
35. Carrera, A. C.; Anderson, R. The Cell Biology behind the Oncogenic PIP3 Lipids. *Journal of Cell Science* **2019**, *132* (1).
36. Bhandari, J.; Sedhai, Y. R. *Hemolytic Uremic Syndrome*. PubMed.
37. So, V.; Wu, J.; Traynor-Kaplan, A.; Choy, C.; Epand, R.; Botelho, R.; Lemaire, M. Phosphatidylinositol Cycle Disruption Is Central to Atypical Hemolytic-Uremic Syndrome Caused by Diacylglycerol Kinase Epsilon Deficiency. *bioRxiv (Cold Spring Harbor Laboratory)* **2019**.
38. Epand, R. M. Features of the Phosphatidylinositol Cycle and Its Role in Signal Transduction. *The Journal of Membrane Biology* **2017**, *250* (4), 353–366.
39. Nefliu, M.; Smith, J. N.; Venter, A.; R. Graham Cooks. Internal energy Distributions in Desorption Electrospray Ionization (DESI). *Journal of the American Society for Mass Spectrometry* **2008**, *19* (3), 420–427.
40. Zhao C, Xie P, Yong T, Wang H, Chung ACK, Cai Z. MALDI- MS imaging reveals asymmetric spatial distribution of lipid metabolites from bisphenol S-induced nephrotoxicity. Anal Chem. 2018;90(5):3196–204.
41. Falkenburger BH, Jensen JB, Dickson EJ, Suh BC, Hille B. Phosphoinositides: lipid regulators of membrane proteins. J Physiol. 2010;3179–3185.
42. Ragh internal energyP, Joseph A, Krishnan H, Singh P, Saha S. Phosphoinositides: regulators of nervous system function in health and disease. Front Mol Neurosci. 2019;12:1–26.
43. Traynor-Kaplan A, Kruse M, Dickson EJ, Dai G, Vivas O, Y internal energyH, Whittington D, Hille B. Fatty-acyl chain profiles of cellular phosphoinositides. Biochim Biophys Acta Mol Cell Biol Lipids. 2017;1862(5):513–22.
44. Idevall-Hagren O, De Camilli P. Detection and manipulation of phosphoinositides. Biochim Biophys Acta. 2015;1851(6):736–45.
45. Staiano L, De Matteis MA. Phosphoinositides in the kidney. J Lipid Res. 2019;60(2):287–98.
46. Szlasa W, Zendran I, Zalesińska A, Tarek M, Kulbacka J. Lipid composition of the cancer cell membrane. J Bioenerg Biomembr. 2020;52:321–42.
47. Kong D, Yamori T. ZSTK474 is an ATP-competitive inhibitor of class I phosphatidylinositol 3 kinase isoforms. Cancer Sci. 2007;98(10):1638–42.
48. Enomoto H, Takeda S, Hatta H. Spatial analysis of phosphatidylinositol molecular species in pork chop tissues using matrix- assisted laser desorption/ionization-mass spectrometry imaging. J Oleo Sci. 2021;70(7):979–87.
49. Kawashima M, Tokiwa M, Nishimura T, Kawata Y, Sugimoto M, Kataoka TR, Sakurai T, Iwaisako K, Suzuki E, Hagiwara M, Harris AL, Toi M. High-resolution imaging mass spectrometry combined with transcriptomic analysis identified a link between fatty acid

composition of phosphatidylinositols and the immune checkpoint pathway at the primary tumour site of breast cancer. Br J Cancer. 2020;122:245–57.
50. Epand RM, So V, Jennings W, Khadka B, Gupta RS, Lemaire M. Diacylglycerol kinase-ε: properties and biological roles. Front Cell Dev Biol. 2016;4(112):1–18.
51. Gode D, Volmer DA. Lipid imaging by mass spectrometry – a review. Analyst. 2013;138:1289–315.
52. Eberlin LS, Li internal energyX, Ferreira CR, Santagata S, Agar NY, Cooks GR. Desorption electrospray ionization then MALDI mass spectrometry imaging of lipid and protein distributions in single tissue sections. Anal Chem. 2011;83(22):8366–71.
53. Bowman AP, et al. Evaluation of lipid coverage and high spatial resolution MALDI-imaging capabilities of over-sampling combined with laser post-ionisation. Anal Bioanal Chem. 2019;412(10):2277–89.
54. Li internal energyJ, et al. Recent advances in mass spectrometry imaging of single cells. Anal Bioanal Chem. 2023;415(18):4093–110.
55. Zemski Berry KA, Hankin JA, Barkley RM, Spraggins JM, Caprioli RM, Murphy RC. MALDI imaging of lipid biochemistry in tis- sues by mass spectrometry. Chem Rev. 2011;111(10):6491–512.
56. Shrivas K, Hayasaka T, Goto-Inoue N, Sugiura Y, Zaima N, Seto internal energyM. Ionic matrix for enhanced MALDI imaging mass spectrometry for identification of phospholipids in mouse liver and cerebellum tissue sections. Anal Chem. 2010;82(21):8800–6.
57. Murphy RC, Hankin JA, Barkley RM. Imaging of lipid species by MALDI mass spectrometry. J Lipid Res. 2009;50:317–22.
58. Perry WJ, Patterson NH, Prentice BM, Neumann EK, Caprioli RM, Spraggins JM. Uncovering matrix effects on lipid analyses in MALDI imaging mass spectrometry experiments. J Mass Spectrom. 2019;55:1–11.
59. Müller M, et al. Limits for the detection of (poly-)phosphoinositides by matrix-assisted laser desorption and ionization time-of-flight mass spectrometry (MALDI-TOF MS). Chem Phys Lipid. 2001;110(2):151–64.
60. Leopold J, et al. A five-year update on matrix compounds for MALDI-MS analysis of lipids. Biomolecules. 2023;13(3):546.
61. Yousefi-Taemeh M, Duli E, Dabija LG, Lemaire M, Ifa DR. Sublimation application of 5-chloro-2-mercaptobenzothiazole matrix for matrix-assisted laser desorption/ionization mass spectrometry imaging of mouse kidney. Rapid Commun Mass Spectrom. 2023;37(16):e9594.
62. Thomas A, et al. Sublimation of new matrix candidates for high spatial resolution imaging mass spectrometry of lipids: enhanced information in both positive and negative polarities after 1,5-diaminonapthalene deposition. Anal Chem. 2012;84(4):2048–54.
63. X internal energyN, Huang Z-H, Watson JT, Gagecor DA. Mercaptobenzothiazoles: a new class of matrices for laser desorption ionization mass spectrometry. J Am Soc Mass Spectrom. 1997;8(2):116–24.
64. Angerer TB, et al. Evaluation of 6 MALDI-matrices for 10 μm lipid imaging and on-tissue MSN with AP-MALDI-orbitrap. J Am Soc Mass Spectrom. 2022;33(5):760–71.
65. Liebisch G, Fahy E, Aoki J, Dennis EA, Durand T, Ejsing CS, et al. Update on LIPID MAPS classification, nomenclature, and shorthand notation for MS-derived lipid structures. J Lipid Res. 2020;61:1539–55.
66. Wishart DS, Tzur D, Knox C et al. HMDB: the Human Metabolome Database. Nucleic

Acids Res. 2007;35(Database issue):D521–6.
67. "Avanti Polar Lipids," [Online]. https://avantilipids.com/. [Accessed 10 August2022].
68. Wang H-YJ, Jackson SN, Woods AS. Direct MALDI-MS analysis of cardiolipin from rat organs sections. J Am Soc Mass Spectrom. 2007;18(3):567–77.
69. Dill AL, et al. Multivariate statistical differentiation of renal cell carcinomas based on lipidomic analysis by ambient ionization imaging mass spectrometry. Anal Bioanal Chem. 2010;398(7–8):2969–78.
70. Smith A, L'Imperio V, Denti V, Mazza M, Ivanova M, Stella M, et al. High Spatial Resolution MALDI-MS Imaging in the Study of Membranous Nephropathy. Proteomics Clin Appl. 2019;13:1800016.
71. Khajavinia A, El-Aneed A. Carbon-based nanoparticles and their surface-modified counterparts as MALDI matrices. Anal Chem. 2023;95(1):100–14.
72. Paratore, T. A.; Schmidt, G. E.; Ross, A. H.; Gericke, A. Thermal Stability of Bivalent Cation/Phosphoinositide Domains in Model Membranes. *Chemistry and Physics of Lipids* **2024**, *264*, 105424–105424.
73. Manna, P.; Jain, S. K. Phosphatidylinositol-3,4,5-Triphosphate and Cellular Signaling: Implications for Obesity and Diabetes. *Cellular Physiology and Biochemistry* **2015**, *35* (4), 1253–1275.
74. Iwata, T., Ishino, Y., Aoki, J., & Kono, N. (2022). Advances in phosphoinositide profiling by mass spectrometry. *Medical Mass Spectrometry: Lipidomics*, *6*(2), 93-100.
75. Clark J, Anderson KE, Juvin V, Smith TS, Karpe F, et al: Quantification of PtdInsP3 molecular species in cells and tissues by mass spectrometry. Nat Methods 8: 267–272, 2011.
76. Morioka, S.; Nakanishi, H.; Yamamoto, T.; Hasegawa, J.; Tokuda, E.; Tomoya Hikita; Sakihara, T.; Yuuki Kugii; Chitose Oneyama; Yamazaki, M.; Suzuki, A.; Sasaki, J.; Sasaki, T. A Mass Spectrometric Method for In-Depth Profiling of Phosphoinositide Regioisomers and Their Disease-Associated Regulation. *Nature Communications* **2022**, *13* (1).
77. Yuta Shimanaka; Matsumoto, K.; Tanaka, Y.; Ishino, Y.; Ni, S.; Guan, J.-L.; Arai, H.; Kono, N. Supercritical Fluid Chromatography-Mass Spectrometry Enables Simultaneous Measurement of All Phosphoinositide Regioisomers. *Communications chemistry* **2022**, *5* (1).
78. Li P, Lämmerhofer M: Isomer selective comprehensive lipidomics analysis of phosphoinositides in biological samples by liquid chromatography with data independent acquisition tandem mass spectrometry. Anal Chem 93:9583–9592, 2021.
79. NTP Technical Report on the Toxicity Studies of Trimethylsilyldiazomethane (CASRN 18107-18-1) Administered by Nose-Only Inhalation to Sprague Dawley (Hsd:Sprague Dawley® SD®) Rats and B6C3F1/N Mice. **2021**.
80. Aichler, M.; Walch, A. MALDI Imaging Mass Spectrometry: Current Frontiers and Perspectives in Pathology Research and Practice. *Laboratory Investigation* **2015**, *95* (4), 422–431.
81. Dabija, L. G.; Yousefi-Taemeh, M.; Ergi Duli; Lemaire, M.; Ifa, D. R. Assessment of MALDI Matrices for the Detection and Visualization of Phosphatidylinositols and Phosphoinositides in Mouse Kidneys through Matrix-Assisted Laser Desorption Ionization Mass Spectrometry Imaging (MALDI-MSI). *Analytical and bioanalytical chemistry/Analytical & bioanalytical chemistry* **2024**, *416* (8), 1857–1865.

82. F. Derwa; E. de Pauw; P. Natalis. New Basis for a Method for the Estimation For Secondary Ion Internal energy Distribution in “Soft” Ionization Techniques. *Organic Mass Spectrometry* **1991**, *26* (2), 117–118.
83. Luo, G.; Marginean, I.; Akos Vertes. Internal energy of Ions Generated by Matrix-Assisted Laser Desorption/Ionization. *Analytical chemistry* **2002**, *74* (24), 6185–6190.
84. Schulz, E.; Karas, M.; Rosu, F.; Gabelica, V. Influence of the Matrix on Analyte Fragmentation in Atmospheric Pressure MALDI. *Journal of the American Society for Mass Spectrometry* **2006**, *17* (7), 1005–1013.
85. Valérie Gabelica; Schulz, E.; Karas, M. Internal energy Build-up in Matrix-Assisted Laser Desorption/Ionization. *Journal of Mass Spectrometry* **2004**, *39* (6), 579–593.
86. Tu, A.; Muddiman, D. C. Internal energy Deposition in Infrared Matrix-Assisted Laser Desorption Electrospray Ionization with and without the Use of Ice as a Matrix. *Journal of the American Society for Mass Spectrometry* **2019**, *30* (11), 2380–2391.
87. Badu-Tawiah, A.; Bland, C.; Campbell, D. I.; Cooks, R. G. Non-Aqueous Spray Solvents and Solubility Effects in Desorption Electrospray Ionization. *Journal of the American Society for Mass Spectrometry* **2010**, *21* (4), 572–579.
88. Valérie Gabelica; Edwin De Pauw. Internal energy and Fragmentation of Ions Produced in Electrospray Sources. **2005**, *24* (4), 566–587.
89. Collette, C.; Drahos, L.; E. De Pauw; K. Vékey. Comparison of the Internal energy Distributions of Ions Produced by Different Electrospray Sources. *Rapid Communications in Mass Spectrometry* **1998**, *12* (22), 1673–1678.
90. Drahos. Thermal Energy Distribution Observed in Electrospray Ionization. *Journal of mass spectrometry : JMS* **2023**, *34* (12).
91. Zins, E.; Rondeau, D.; Philippe Karoyan; Fosse, C.; Rochut, S.; Pepe, C. Investigations of the Fragmentation Pathways of Benzylpyridinium Ions under ESI/MS Conditions. *Journal of Mass Spectrometry* **2009**, *44* (12), 1668–1675.
92. Flanigan, P. M.; Shi, F.; Perez, J. J.; Karki, S.; Pfeiffer, C.; Schafmeister, C.; Levis, R. J. Determination of Internal energy Distributions of Laser Electrospray Mass Spectrometry Using Thermometer Ions and Other Biomolecules. *Journal of the American Society for Mass Spectrometry* **2014**, *25* (9), 1572–1582.
93. Asakawa, D. Phenyl Sulfate Derivatives: New Thermometer Ions for Characterization of Internal energy of Negative Ions Produced by Electrospray Ionization. *Journal of the American Society for Mass Spectrometry* **2023**, *34* (3), 435–440.
94. Vaidyanathan S, Goodacre R (2007) Quantitative detection of metabolites using matrix-assisted laser desorption/ionization mass spectrometry with 9-aminoacridine as the matrix. Rapid Commun Mass Spectrom 21:2072–2078.
95. Jackson, S. N.; Muller, L.; Roux, A.; Berk Oktem; Moskovets, E.; Doroshenko, V. M.; Woods, A. S. AP-MALDI Mass Spectrometry Imaging of Gangliosides Using 2,6-Dihydroxyacetophenone. *Journal of the American Society for Mass Spectrometry* **2018**, *29* (7), 1463–1472.
96. Yang, H.; Jackson, S.N.; Woods, A.S.; Goodlett, D.R.; Ernst, R.K.; Scott, A.J. Streamlined analysis of cardiolipins in prokaryotic and eukaryotic samples using a norharmane matrix by MALDI-MSI. J. Am. Soc. Mass Spectrom. **2020**, 31, 2495–2502.
97. Lemaire, P.; Debois, D.; Smargiasso, N.; Quinton, L.; Gabelica, V.; De Pauw, E. A. Use of 1,5-Diaminonaphthalene to Combine Matrix-Assisted Laser Desorption/Ionization In-Source Decay Fragmentation with Hydrogen/Deuterium Exchange. *Rapid*

*Communications in Mass Spectrometry* **2013**, *27* (16), 1837–1846.
98. Wang, J.; Qiu, S.; Chen, S.; Xiong, C.; Liu, H.; Wang, J.; Zhang, N.; Hou, J.; He, Q.; Nie, Z. MALDI-TOF MS Imaging of Metabolites with a *N*-(1-Naphthyl) Ethylenediamine Dihydrochloride Matrix and Its Application to Colorectal Cancer Liver Metastasis. *Analytical Chemistry* **2014**, *87* (1), 422–430.

# APPENDICES

Appendix A. Supplementary materials for Chapter 2.

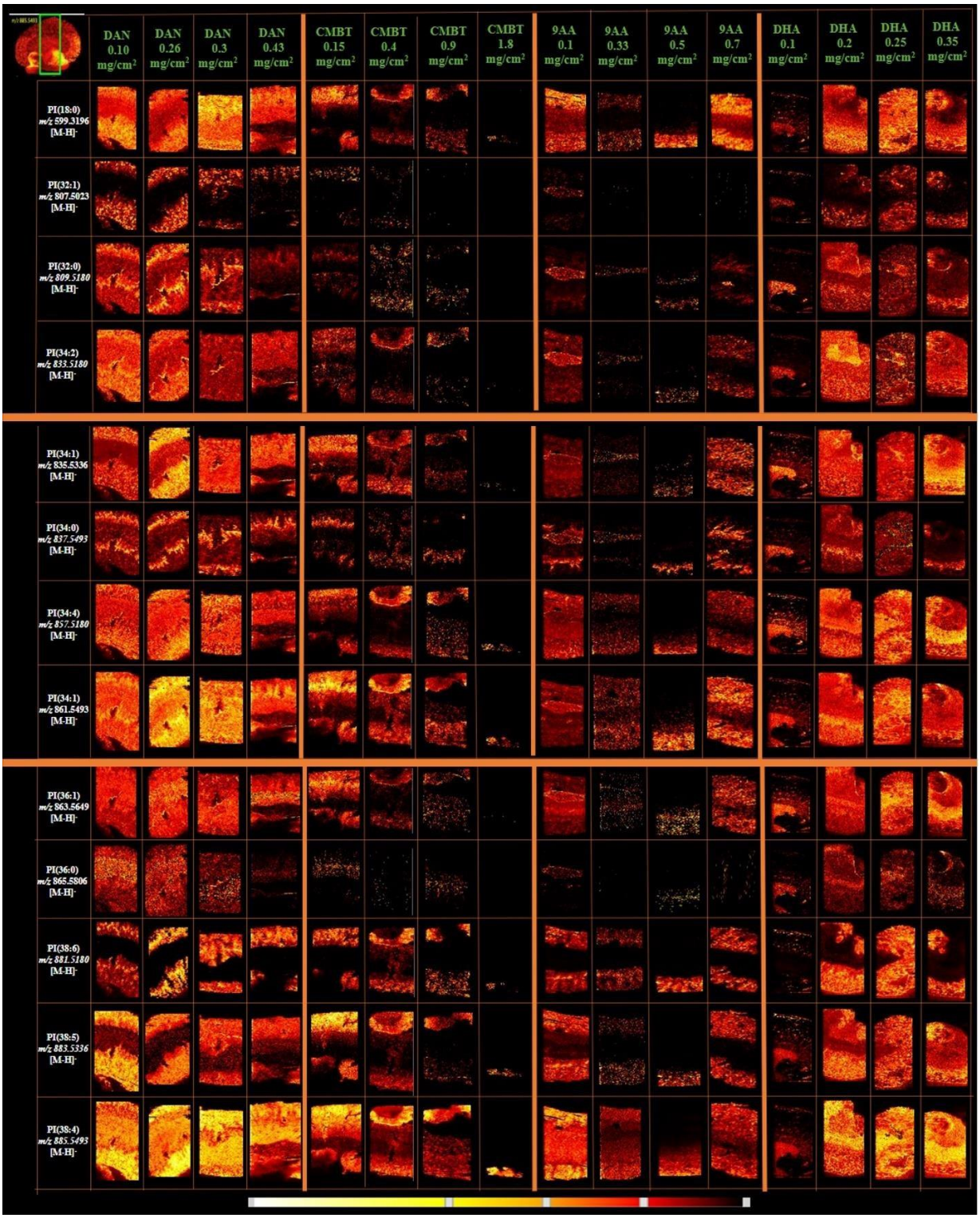

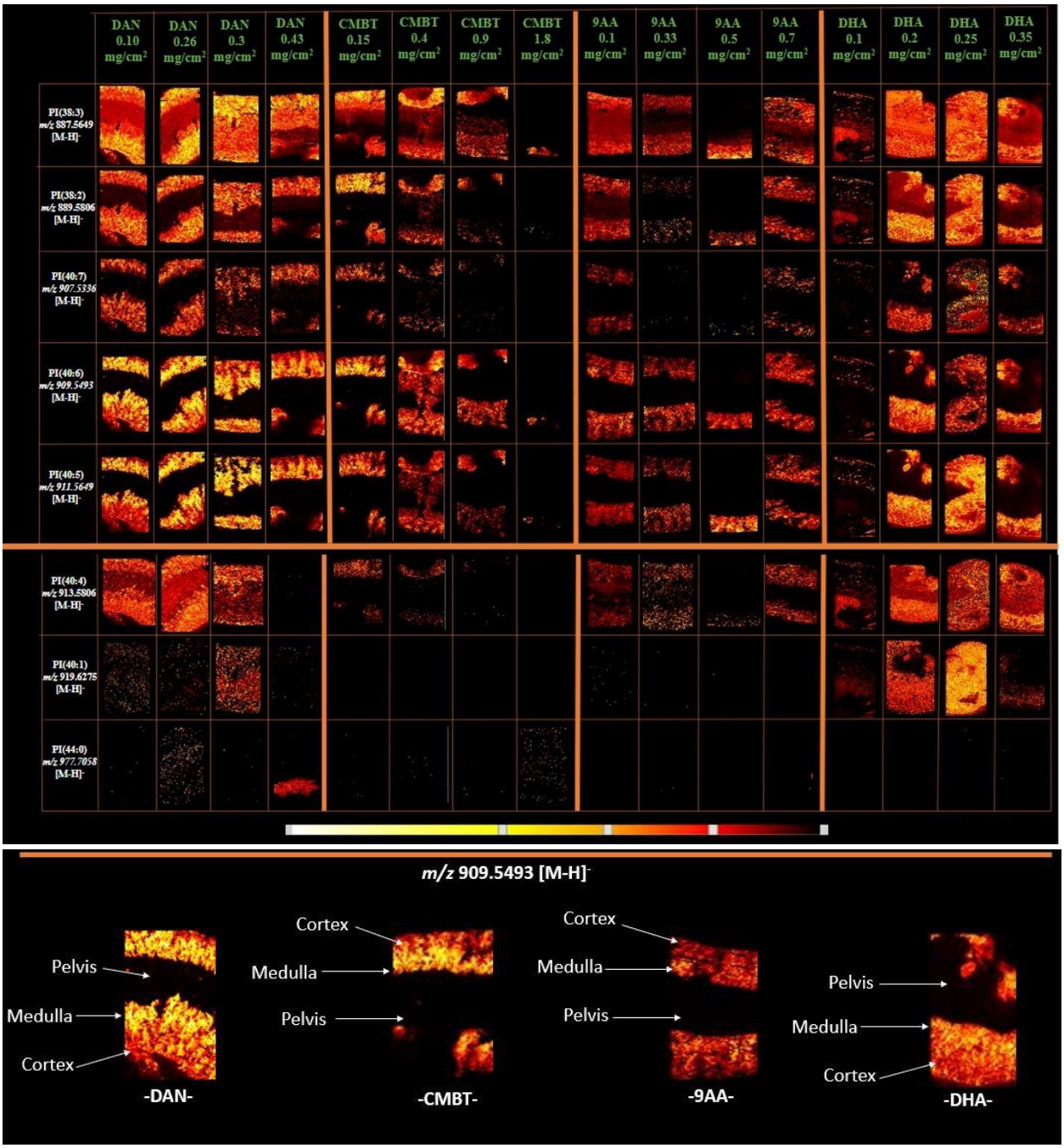


**Figure A.1**: Chemical matrices of 1,5-diaminonaphthalene (DAN), 5-chloro-2-mercaptobenzothiazole (CMBT), 9-aminoacridine (9AA), and 2,5-dihydroxyacetophenone (DHA) at varying thicknesses, showcasing the distribution of phosphatidylinositol species. For this analysis, coronal sections from the central region of each kidney sample, encompassing the renal cortex, medulla, and pelvis, were selected to expedite the analysis time.

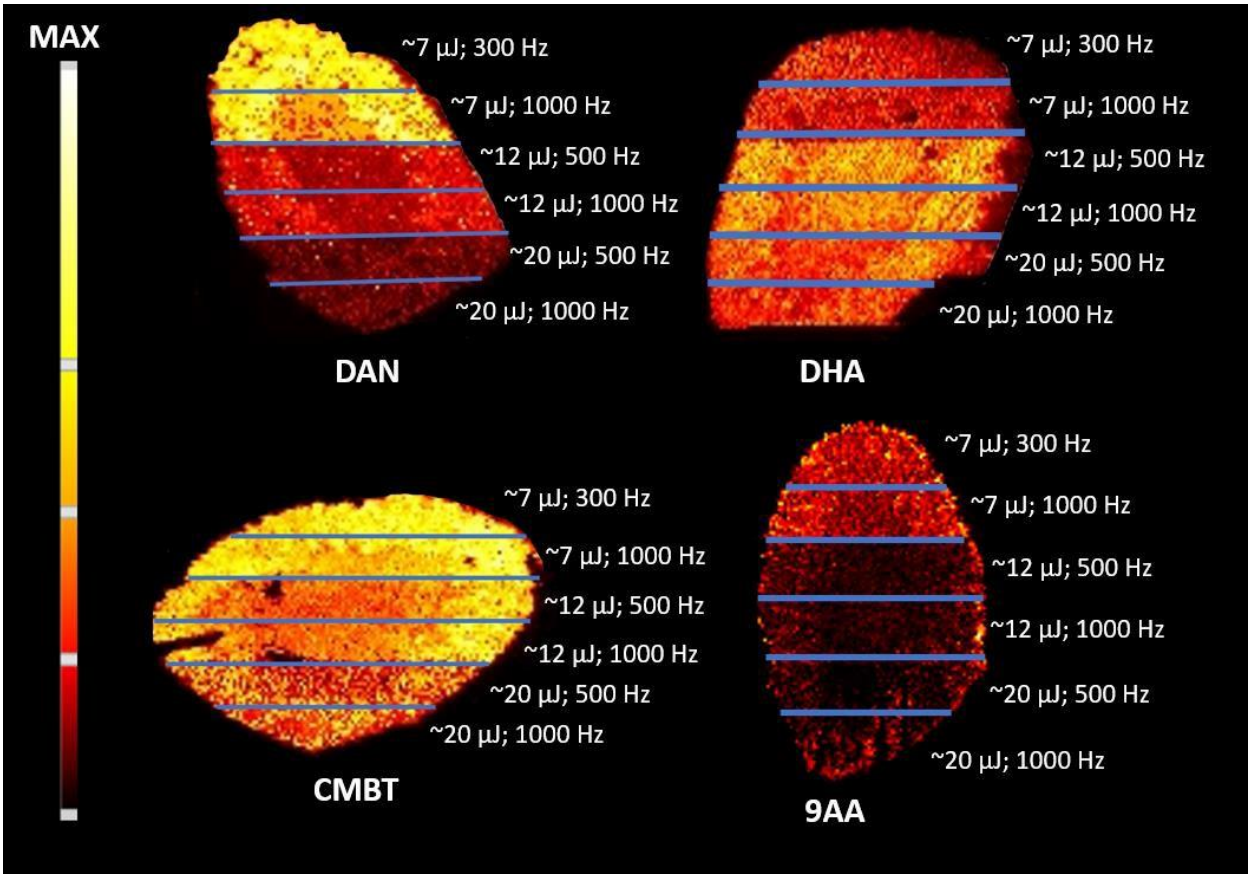


**Figure A.2:** Optimization of laser parameters (laser energy (µJ); repetition rate (Hz)) for each respective matrix: 1,5-diaminonaphthalene (DAN); 2,5-dihydroxyacetophenone (DHA); 5-chloro-2-mercaptobenzothiazole (CMBT); and 9-aminoacridine (9AA). During the imaging experiments, laser settings were adjusted every 16% interval to determine the optimal combination that yields the highest ionization for PI(18:0_20:4)- *m/z* 885.55. The settings that generated the most intense signal were then used for subsequent analyses.

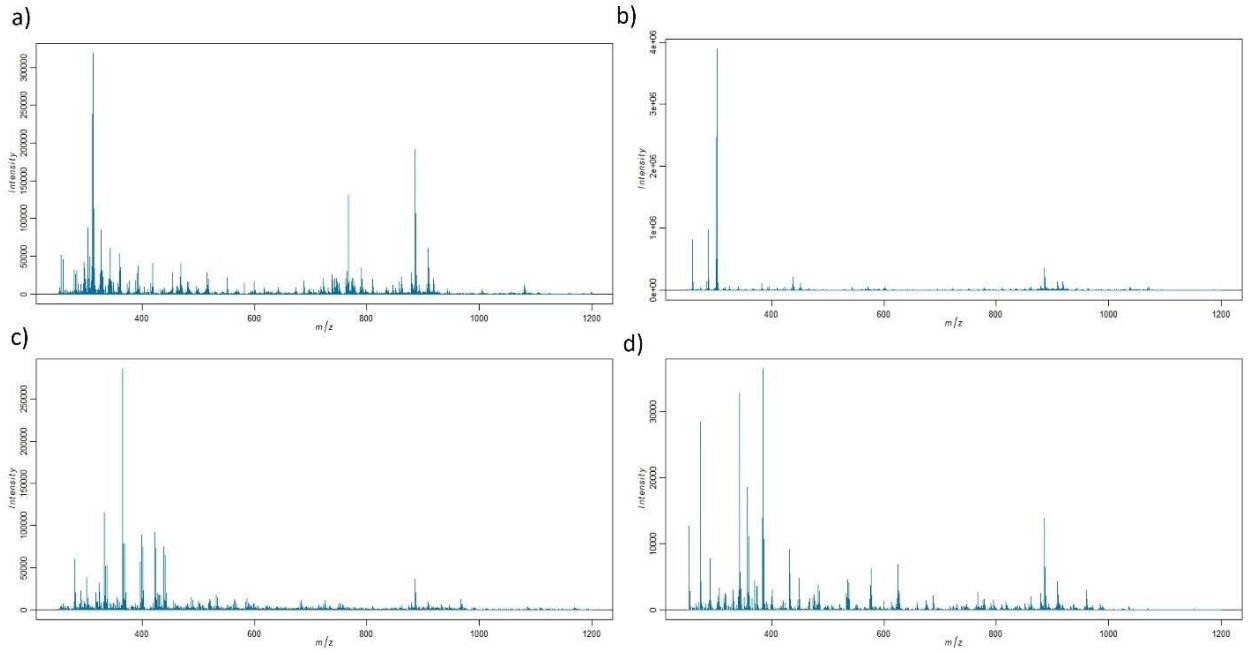


**Figure A.3**: Average mass spectra (*m/z* 250-1200) of the first technical replicate for each respective matrix compound; (A) 1,5-diaminonaphthalene; (B) 2,5-dihydroxyacetophenone; (C) 5-chloro-2-mercaptobenzothiazole; and (D) 9-aminoacridine.

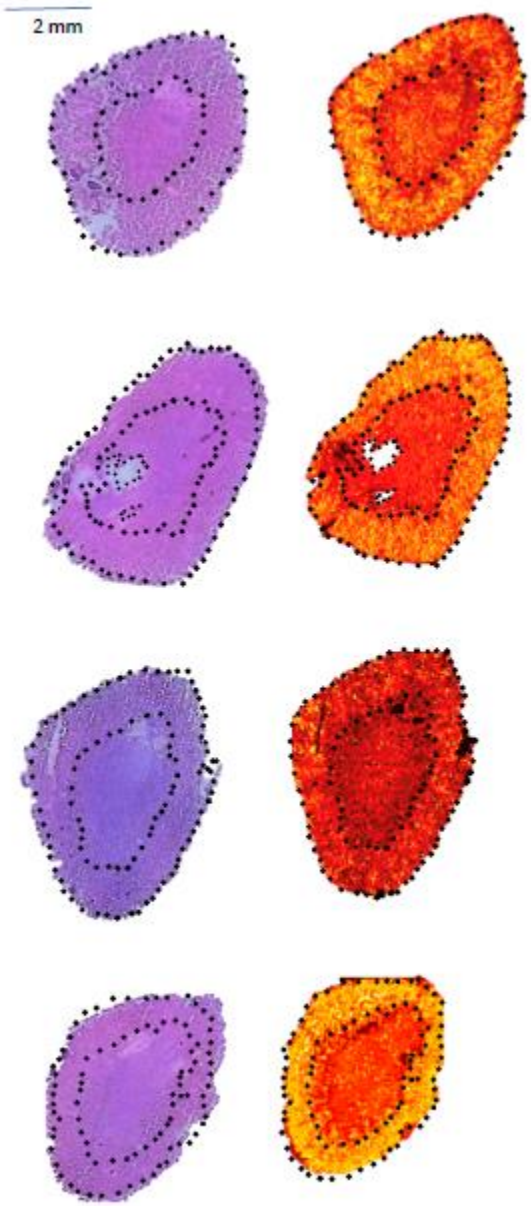


**Figure A.4**: Optical H&E images presented alongside their corresponding ion image. On the left, the H&E- stained kidney tissue is shown post-MALDI-MSI analysis, with the adjacent ion image on the right showing the distribution of PI(18:0_20:4)- *m/z* 885.55.

**Table A.1**. Signal-to-noise ratios (S/N) of phosphatidylinositol species from the first technical replicate captured by various chemical matrices: DAN, CMBT, DHA, and 9AA.

| Species | DAN-1 | DHA-1 | CMBT-1 | 9AA-1 |
|---|---|---|---|---|
| 18:0/OH PI | 841.2507074 | 1366.66476 | 84.31069959 | 230.3960396 |
| 16:0/16:1 PI | 35.94230769 | 54.02713317 | 3.31744868 | 0.4315960912 |
| 16:0/16:0 PI | 115.9554873 | 199.9786401 | 7.378427788 | 46.9724026 |
| 16:0/18:2 PI | 187.9020194 | 374.8576329 | 21.90003545 | 34.10700236 |
| 16:0/18:1 PI | 272.220978 | 495.3009576 | 42.57779349 | 50.24313725 |
| 16:0/18:0 PI | 123.735568 | 222.9287419 | 4.532627866 | 81.97965571 |
| 16:0/20:4 PI | 552.1926304 | 789.8660224 | 85.08427933 | 92.91193182 |
| 18:0/18:2 PI | 732.7315656 | 1409.85846 | 100.0821636 | 217.1222475 |
| 18:0/18:1 PI | 171.9434373 | 333.3606826 | 15.74257426 | 57.22937169 |
| 18:0/18:0 PI | 11.43632417 | 37.37565445 | 0 | 0 |
| 16:0/22:6 PI | 548.5907956 | 1099.470475 | 78.87474883 | 82.09509658 |
| 18:0/20:5 PI | 379.1087344 | 759.1410256 | 77.83205085 | 54.7473997 |
| 18:0/20:4 PI | 6417.221233 | 12723.2789 | 994.5120321 | 1271.967335 |
| 18:0/20:3 PI | 2319.366323 | 4188.867562 | 319.5036222 | 440.0519288 |
| 18:0/20:2 PI | 336.1010317 | 571.5020773 | 34.24949967 | 58.91691395 |
| 18:1/22:6 PI | 25.65924355 | 99.63267891 | 4.887566138 | 1.499261448 |
| 18:0/22:6 PI | 1864.132815 | 3749.098387 | 213.7396762 | 415.9188192 |
| 18:0/22:5 PI | 446.8595625 | 918.3628319 | 49.84158416 | 89.22566372 |
| 18:0/22:4 PI | 96.33991537 | 204.2627092 | 5.324760963 | 14.18879056 |
| 18:0/22:1 PI | 9.282195637 | 47.45142156 | 0 | 2.164948454 |
| 22:0/22:0 PI | 0 | 0 | 0 | 0 |
| 16:1/18:0 PIP | 0 | 0 | 0.7946577629 | 0 |
| 18:2/16:0 PIP | 0 | 0 | 0.069238 | 0 |
| 16:0/18:1 PIP | 7.921071177 | 3.711065574 | 0 | 0 |
| 18:1/18:1 PIP | 7.402234637 | 7.2251635 | 0 | 0 |
| 18:0/20:4 PIP | 78.60505365 | 47.38214644 | 8.651890482 | 0 |
| 18:1/18:1 PIP2 | 1.383184 | 0 | 0 | 0 |
| 18:0/18:1 PIP2 | 0.3770380435 | 4.994036971 | 0 | 0 |
| 18:0/20:4 PIP2 | 0.2230009557 | 1.241204066 | 0.316631 | 0 |
| 16:0/16:1 PIP3 | 0.04138809296 | 0 | 0 | 0 |
| 16:0/16:0 PIP3 | 0 | 0 | 0 | 0 |
| 16:0/18:1 PIP3 | 0 | 0 | 0 | 0 |
| 18:1/18:1 PIP3 | 0 | 0 | 0 | 0 |
| 18:0/18:1 PIP3 | 0 | 0 | 1.691395 | 0 |
| 18:0/20:4 PIP3 | 0 | 0 | 14.77738723 | 0 |
| 18:1/20:3 PIP3 | 0 | 0 | 6.612053833 | 0 |

# MS/MS spectra of identified species

# PI(18:0/OH) – *m/z* 599.3196 $[M-H]^-$

# $C_{27}H_{52}O_{12}P$

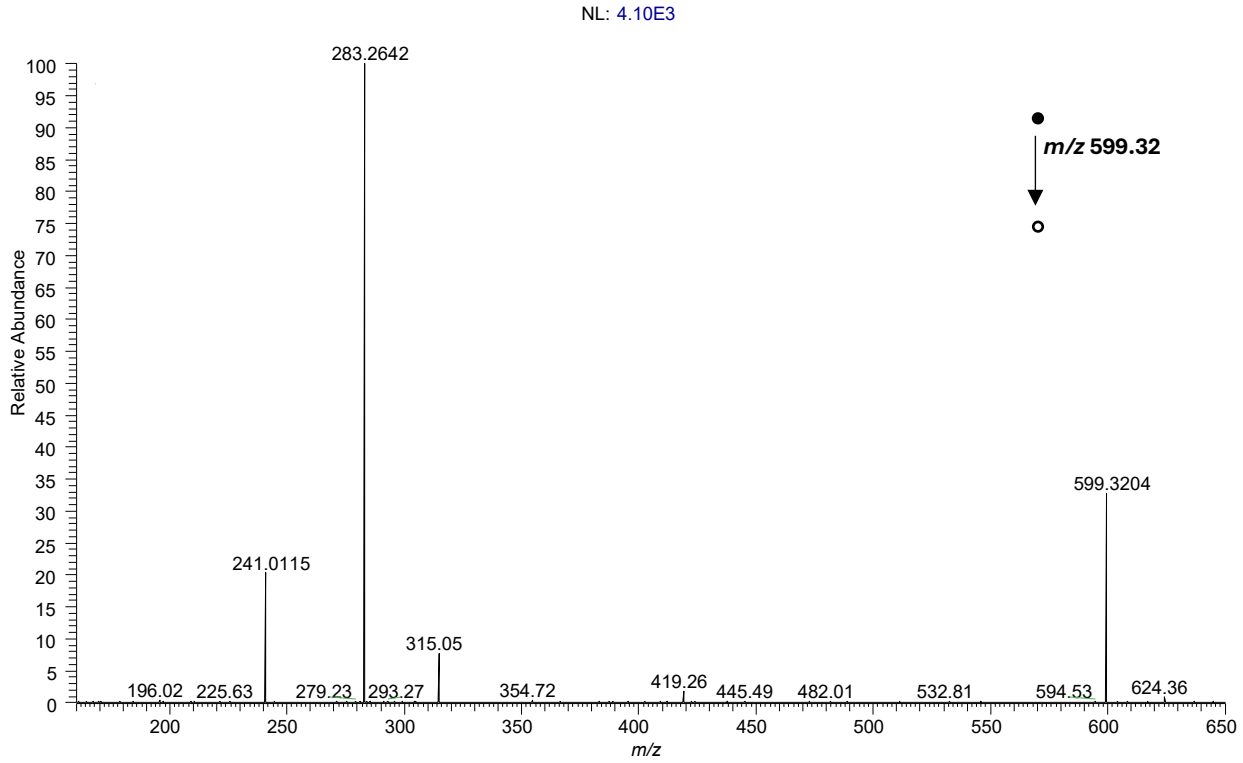


| Product ions (*m/z*) | Exact mass | Species | Formula (-) | Mass error (ppm) |
|---|---|---|---|---|
| 283.2642 | 283.2637 | FA 18:0 | $C_{18}H_{35}O_2$ | 1.76 |
| 241.0115 | 241.0113 | IP -$H_2O$ | $C_6H_{10}O_8P$ | 0.83 |

# PI(16:0_16:0)- *m/z* 809.5180 $[M-H]^-$ $C_{41}H_{78}O_{13}P$

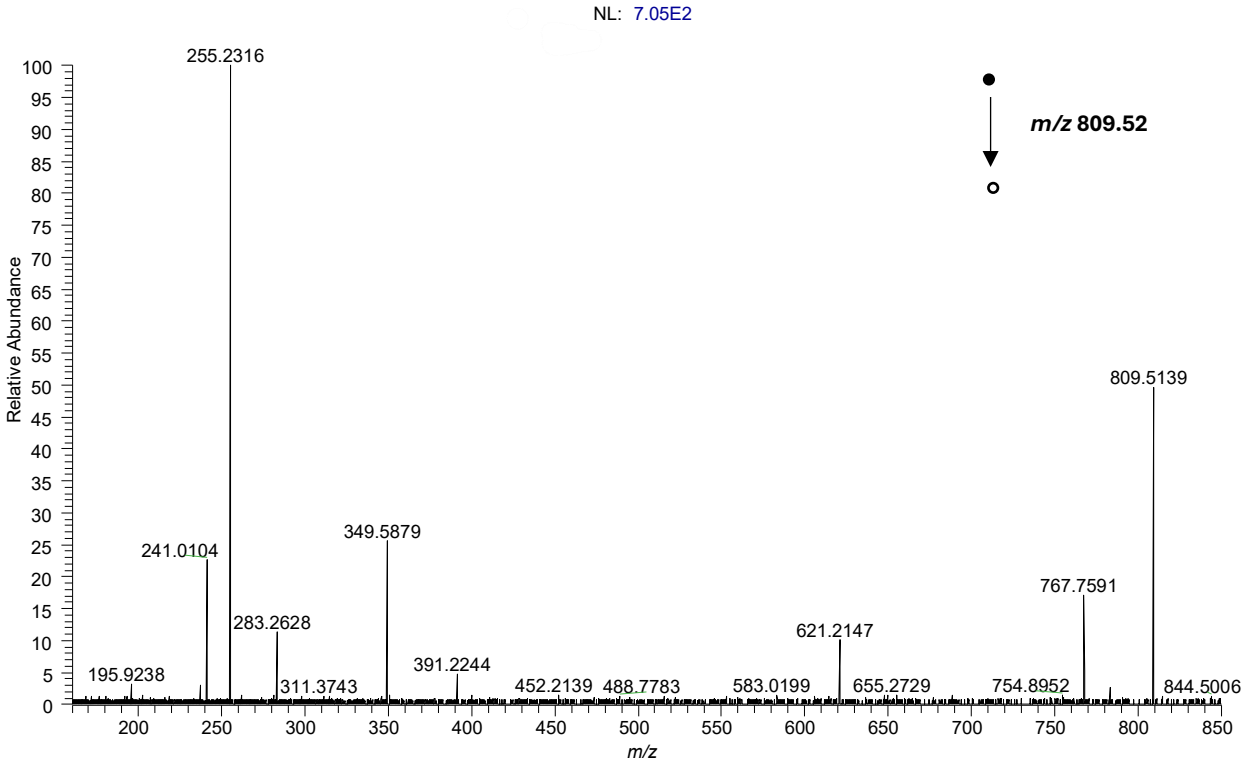


| Product ions (*m/z*) | Exact mass | Species | Formula (-) | Mass error (ppm) |
|---|---|---|---|---|
| 255.2316 | 255.2324 | FA 16:0 | $C_{16}H_{31}O_2$ | -2.74 |
| 241.0104 | 241.0113 | IP -$H_2O$ | $C_6H_{10}O_8P$ | -2.90 |

# PI(16:0_18:2)- *m/z* 833.5180 [M-H]$^-$

## $C_{43}H_{79}O_{13}P$

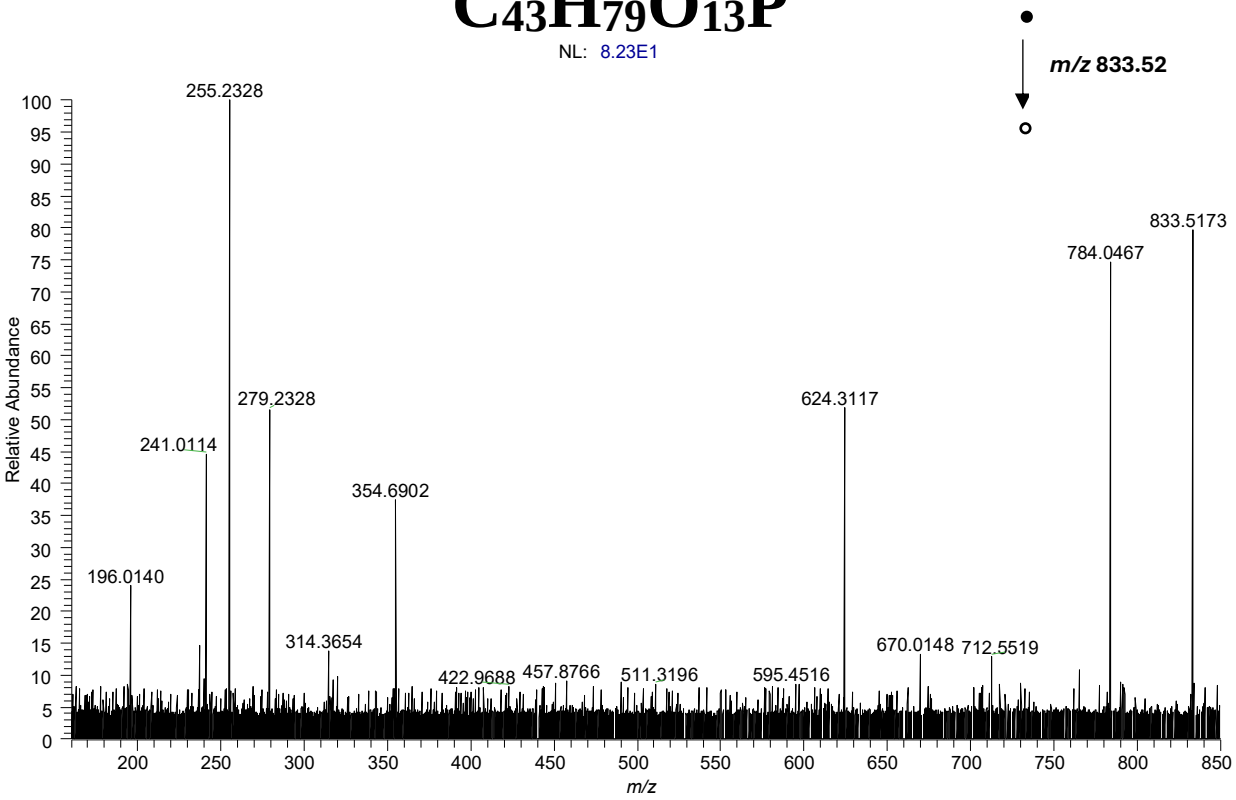


| Product ions (*m/z*) | Exact mass | Species | Formula (-) | Mass error (ppm) |
|---|---|---|---|---|
| 255.2328 | 255.2324 | FA 16:0 | $C_{16}H_{31}O_2$ | 1.56 |
| 241.0114 | 241.0113 | IP -$H_2O$ | $C_6H_{10}O_8P$ | 0.41 |
| 279.2328 | 279.2324 | FA 18:2 | $C_{18}H_{31}O_2$ | 1.43 |

# PI(16:0_18:1)- *m/z* 835.5336 $[M-H]^-$

# $C_{43}H_{80}O_{13}P$

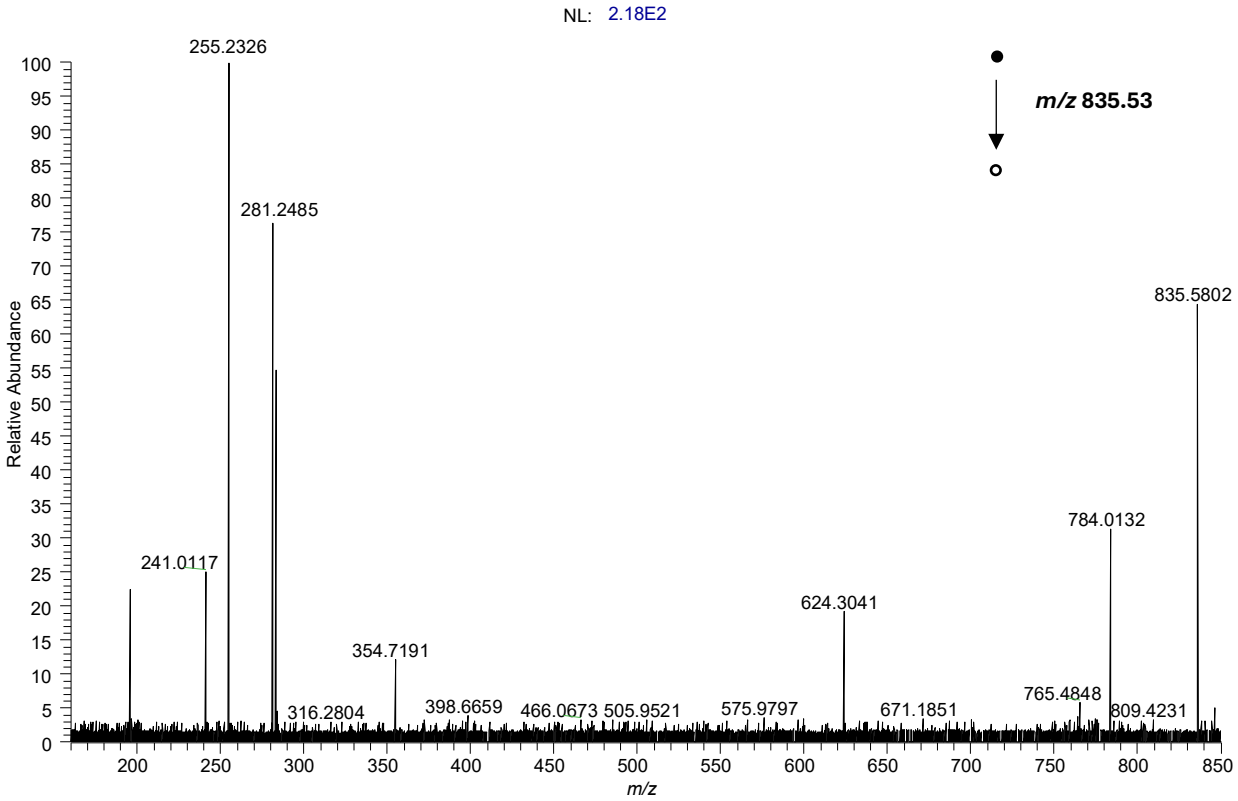


| Product ions (*m/z*) | Exact mass | Species | Formula (-) | Mass error (ppm) |
|---|---|---|---|---|
| 255.2326 | 255.2324 | FA 16:0 | $C_{16}H_{31}O_2$ | 0.78 |
| 241.0117 | 241.0113 | PI $-H_2O$ | $C_6H_{10}O_8P$ | 1.65 |
| 281.2485 | 281.2480 | FA 18:1 | $C_{18}H_{33}O_2$ | 1.77 |

# PI(16:0_18:0)- *m/z* 837.5493 $[M-H]^-$ $C_{43}H_{82}O_{13}P$

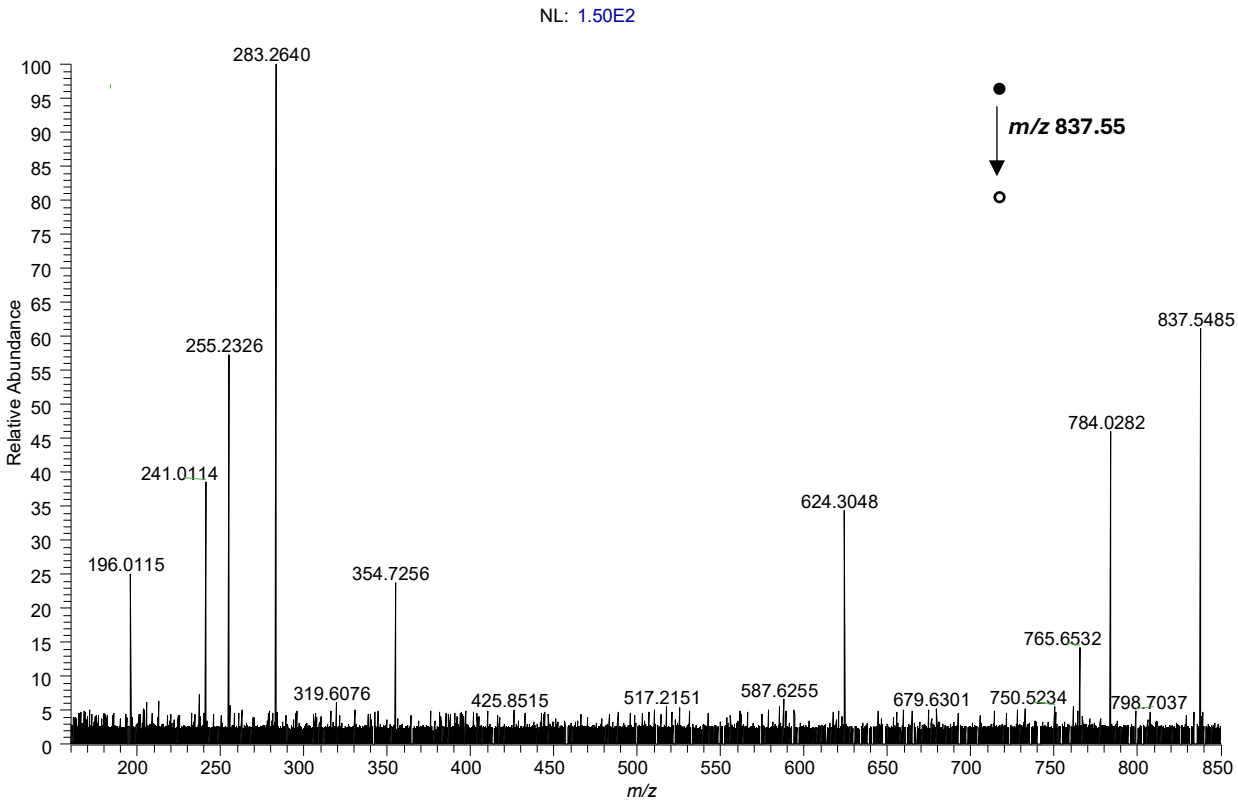


| Product ions (*m/z*) | Exact mass | Species | Formula (-) | Mass error (ppm) |
|---|---|---|---|---|
| 255.2326 | 255.2324 | FA 16:0 | $C_{16}H_{31}O_2$ | 0.78 |
| 241.0114 | 241.0113 | IP -$H_2O$ | $C_6H_{10}O_8P$ | 0.41 |
| 283.2640 | 283.2637 | FA 18:0 | $C_{18}H_{35}O_2$ | 1.06 |

# PI(16:0_20:4)- *m/z* 857.5180 $[M-H]^-$

# $C_{45}H_{78}O_{13}P$

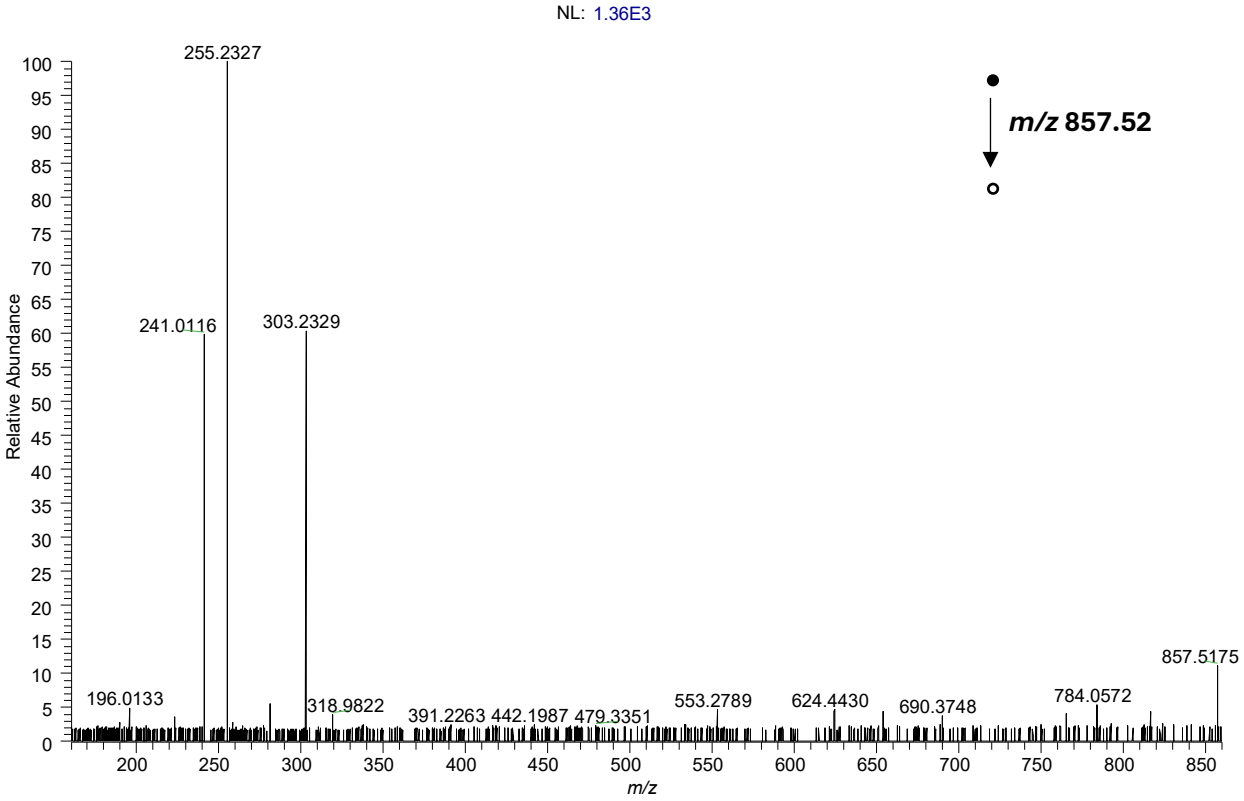


| Product ions (*m/z*) | Exact mass | Species | Formula (-) | Mass error (ppm) |
|---|---|---|---|---|
| 255.2327 | 255.2324 | FA 16:0 | $C_{16}H_{31}O_2$ | 1.17 |
| 241.0116 | 241.0113 | IP -$H_2O$ | $C_6H_{10}O_8P$ | 1.24 |
| 303.2329 | 303.2324 | FA 20:4 | $C_{20}H_{31}O_2$ | 1.64 |

# PI(18:0_18:2)- *m/z* 861.5493 $[M-H]^-$

# $C_{45}H_{82}O_{13}P$

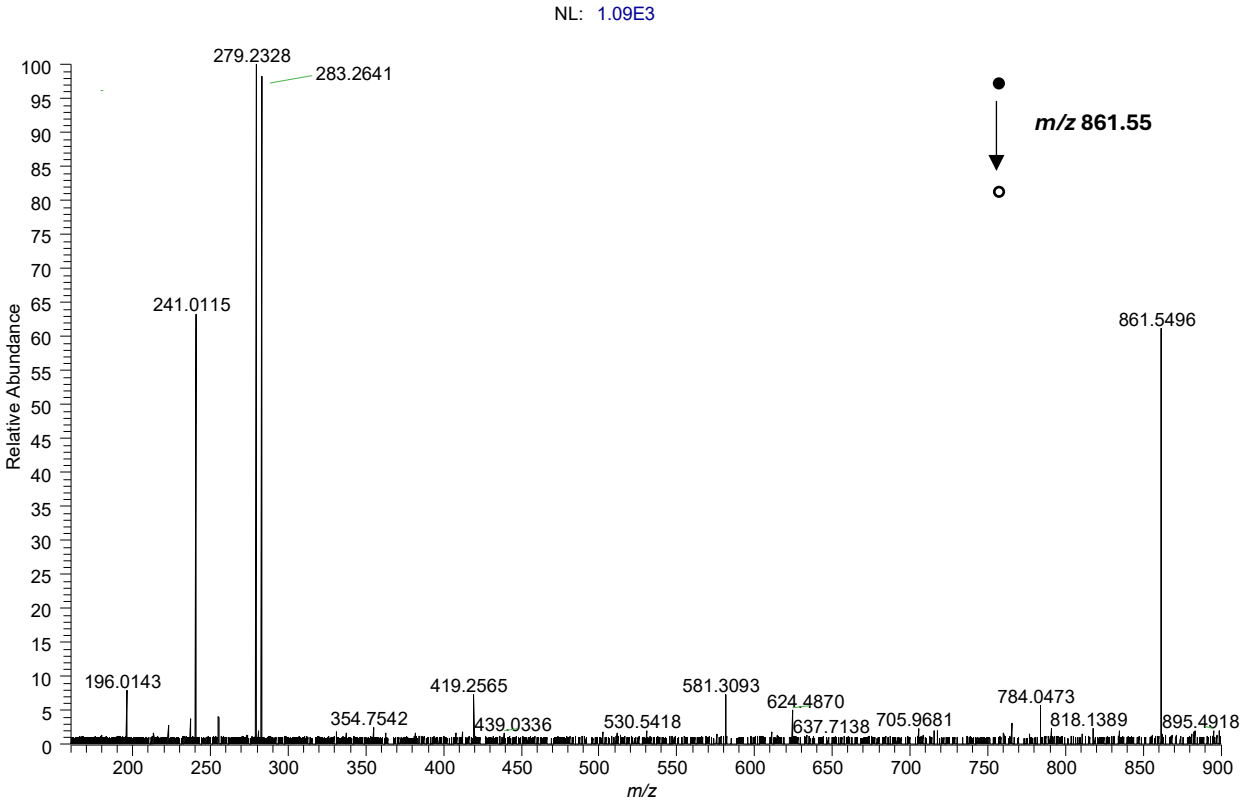


| Product ions (*m/z*) | Exact mass | Species | Formula (-) | Mass error (ppm) |
|---|---|---|---|---|
| 283.2641 | 283.2637 | FA 18:0 | $C_{18}H_{35}O_2$ | 1.41 |
| 279.2328 | 279.2324 | FA 18:2 | $C_{18}H_{31}O_2$ | 1.43 |
| 241.0115 | 241.0113 | IP -$H_2O$ | $C_6H_{10}O_8P$ | 0.82 |

# PI(18:0_18:1)- *m/z* 863.5649 $[M-H]^-$

# $C_{45}H_{85}O_{13}P$

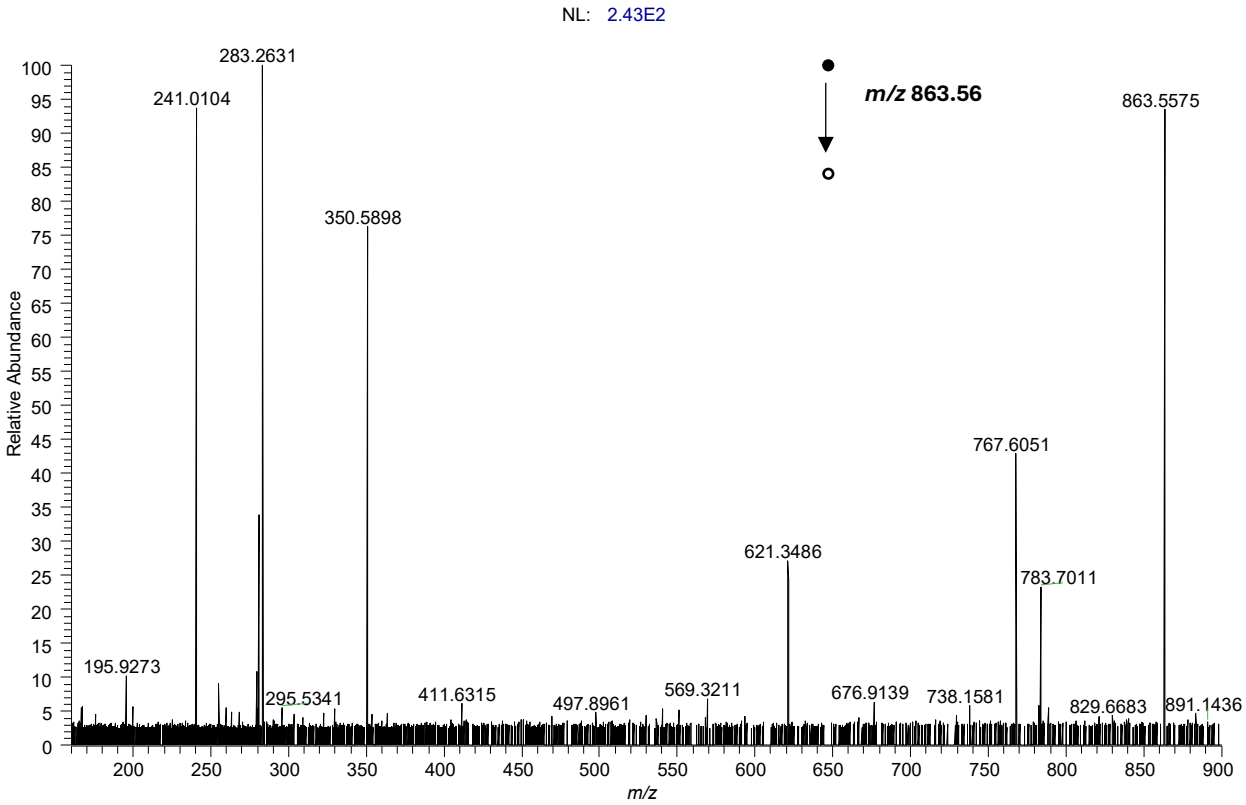


| Product ions (*m/z*) | Exact mass | Species | Formula (-) | Mass error (ppm) |
|---|---|---|---|---|
| 283.2631 | 283.2637 | FA 18:0Stearic acid | $C_{18}H_{35}O_2$ | -2.12 |
| 241.0104 | 241.0113 | IP -$H_2O$ | $C_6H_{10}O_8P$ | -3.73 |

# PI(16:0_22:6)- *m/z* 881.5180 $[M-H]^-$

# $C_{47}H_{78}O_{13}P$

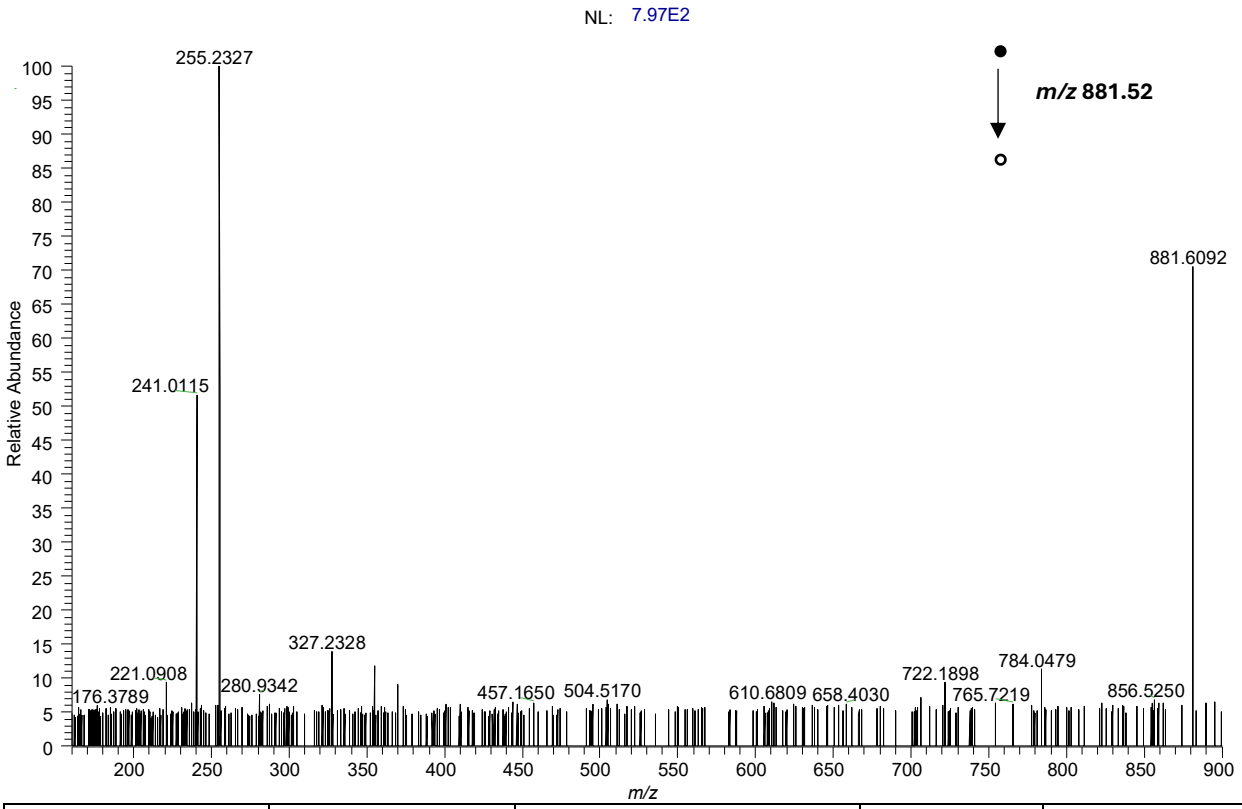


| Product ions (*m/z*) | Exact mass | Species | Formula (-) | Mass error (ppm) |
|---|---|---|---|---|
| 255.2327 | 255.2324 | FA 16:0 | $C_{16}H_{31}O_2$ | 1.17 |
| 241.0115 | 241.0113 | IP -$H_2O$ | $C_6H_{10}O_8P$ | 0.83 |
| 327.2328 | 327.2324 | FA 22:6 | $C_{22}H_{31}O_2$ | 1.22 |

# PI(18:1_20:4)- *m/z* 883.5336 $[M-H]^-$

# $C_{47}H_{80}O_{13}P$

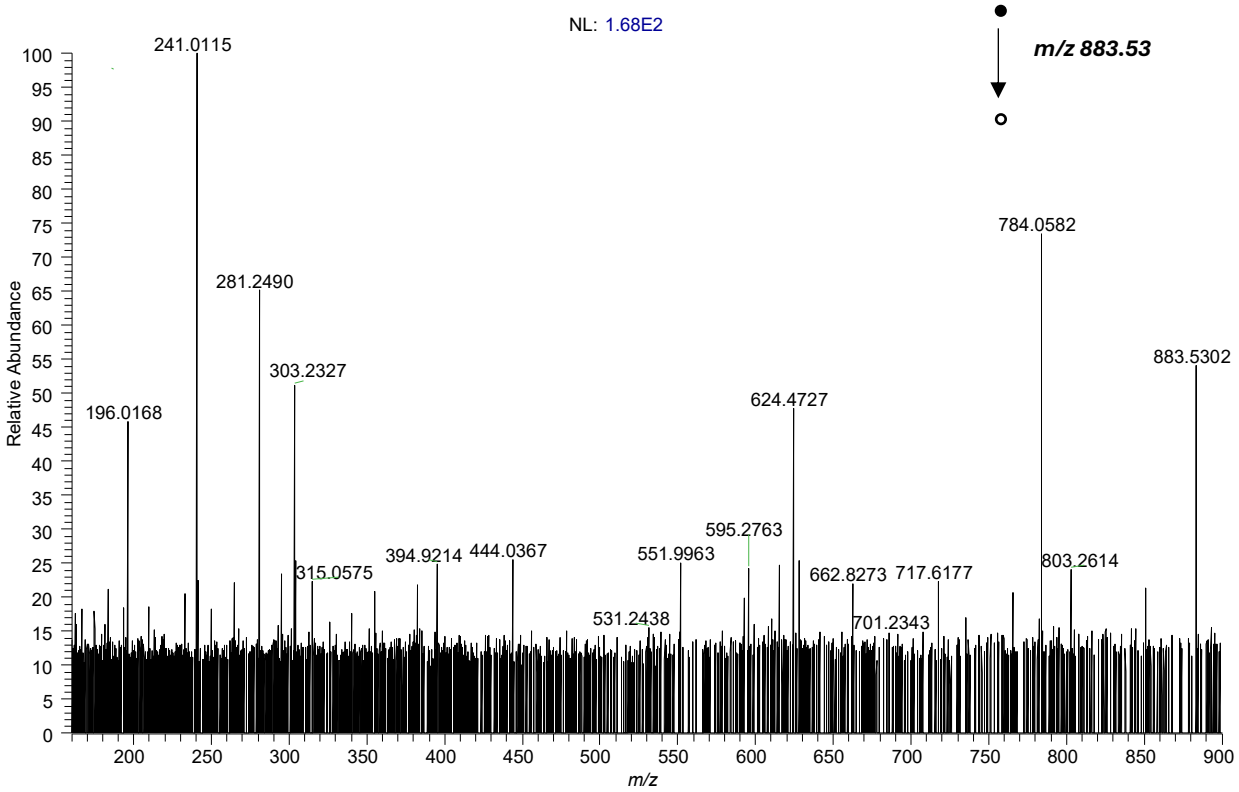


| Product ions (*m/z*) | Exact mass | Species | Formula (-) | Mass error (ppm) |
|---|---|---|---|---|
| 303.2327 | 303.2324 | FA 20:4 | $C_{20}H_{31}O_2$ | 0.98 |
| 281.2490 | 281.2480 | FA 18:1 | $C_{18}H_{33}O_2$ | 3.55 |
| 241.0115 | 241.0113 | IP -$H_2O$ | $C_6H_{10}O_8P$ | 0.82 |

# PI(18:0_20:4)- *m/z* 885.5493 $[M-H]^-$

# $C_{47}H_{82}O_{13}P$

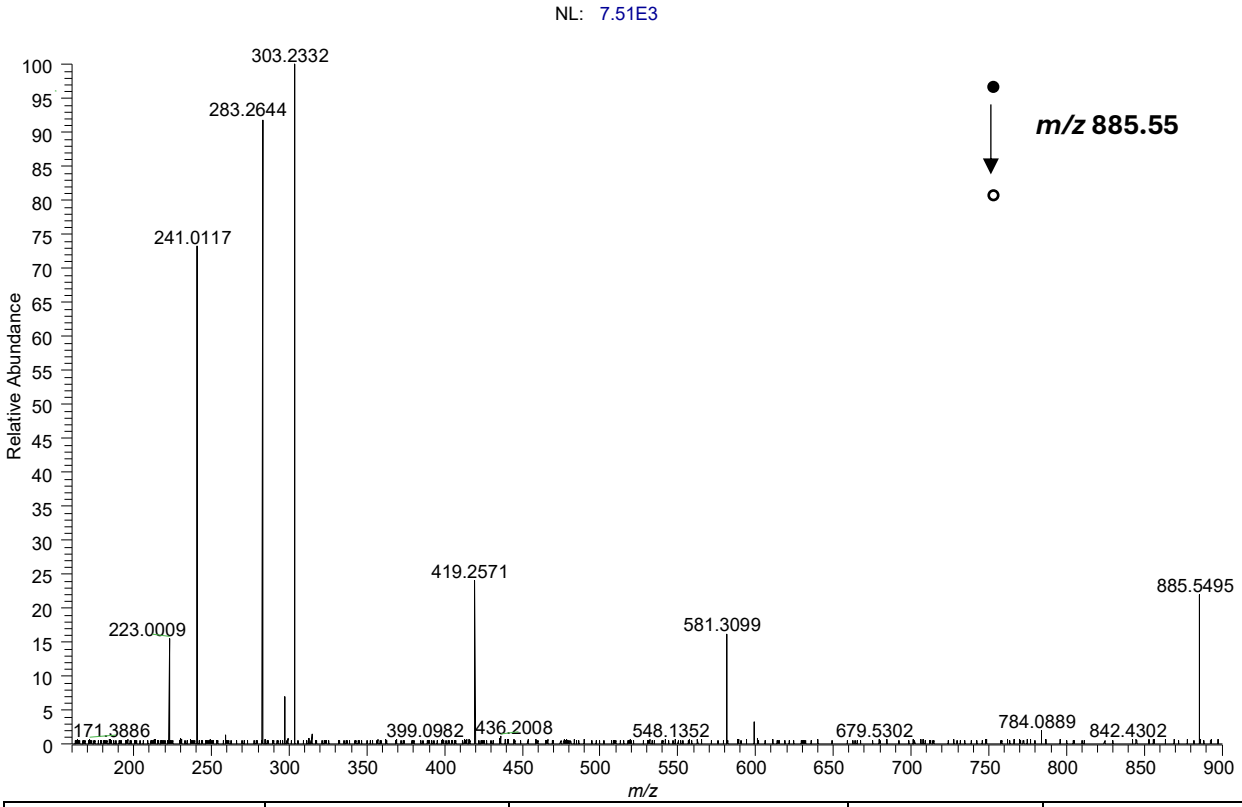


| Product ions (*m/z*) | Exact mass | Species | Formula (-) | Mass error (ppm) |
|---|---|---|---|---|
| 303.2332 | 303.2324 | FA 20:4 | $C_{20}H_{31}O_2$ | 2.64 |
| 283.2644 | 283.2637 | FA 18:0 | $C_{18}H_{35}O_2$ | 2.47 |
| 241.0117 | 241.0113 | IP -$H_2O$ | $C_6H_{10}O_8P$ | 0.83 |
| 581.3099 | 581.3091 | PI 18:0 -$H_2O$ | $C_{27}H_{50}O_{11}P$ | 1.37 |
| 419.2571 | 419.2562 | PA18:0 -$H_2O$ | $C_{21}H_{40}O_6P$ | 2.14 |

# PI(18:0_20:3)- *m/z* 887.5649 $[M-H]^-$

# $C_{47}H_{84}O_{13}P$

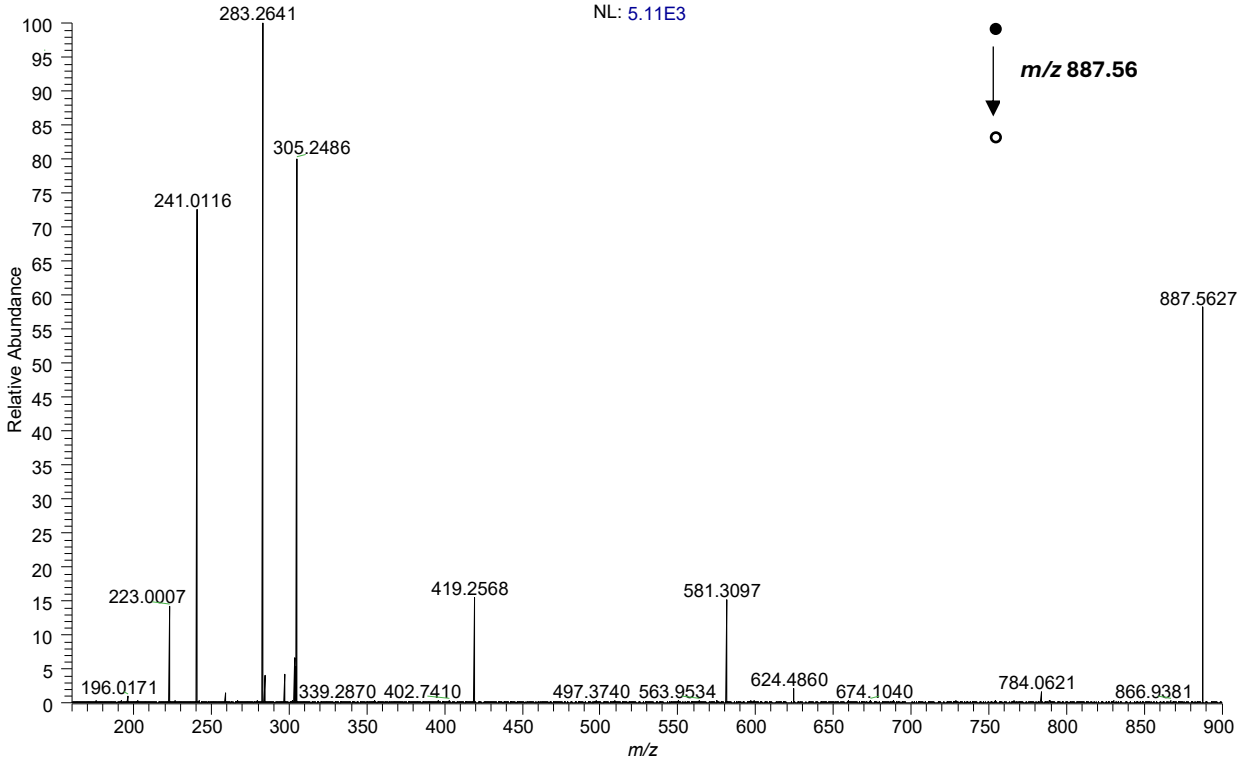


| Product ions (*m/z*) | Exact mass | Species | Formula (-) | Mass error (ppm) |
|---|---|---|---|---|
| 305.2486 | 305.2480 | FA 20:3 | $C_{20}H_{33}O_2$ | 1.96 |
| 283.2641 | 283.2637 | FA 20:4 | $C_{18}H_{35}O_2$ | 1.41 |
| 241.0116 | 241.0113 | IP -$H_2O$ | $C_6H_{10}O_8P$ | 1.24 |
| 581.3097 | 581.3091 | PI 18:0 -$H_2O$ | $C_{27}H_{50}O_{11}P$ | 1.03 |
| 419.2568 | 419.2562 | PA 18:0 -$H_2O$ | $C_{21}H_{40}O_6P$ | 1.43 |

# PI(18:0_20:2)- *m/z* 889.5806 $[M-H]^-$

# $C_{47}H_{86}O_{13}P$

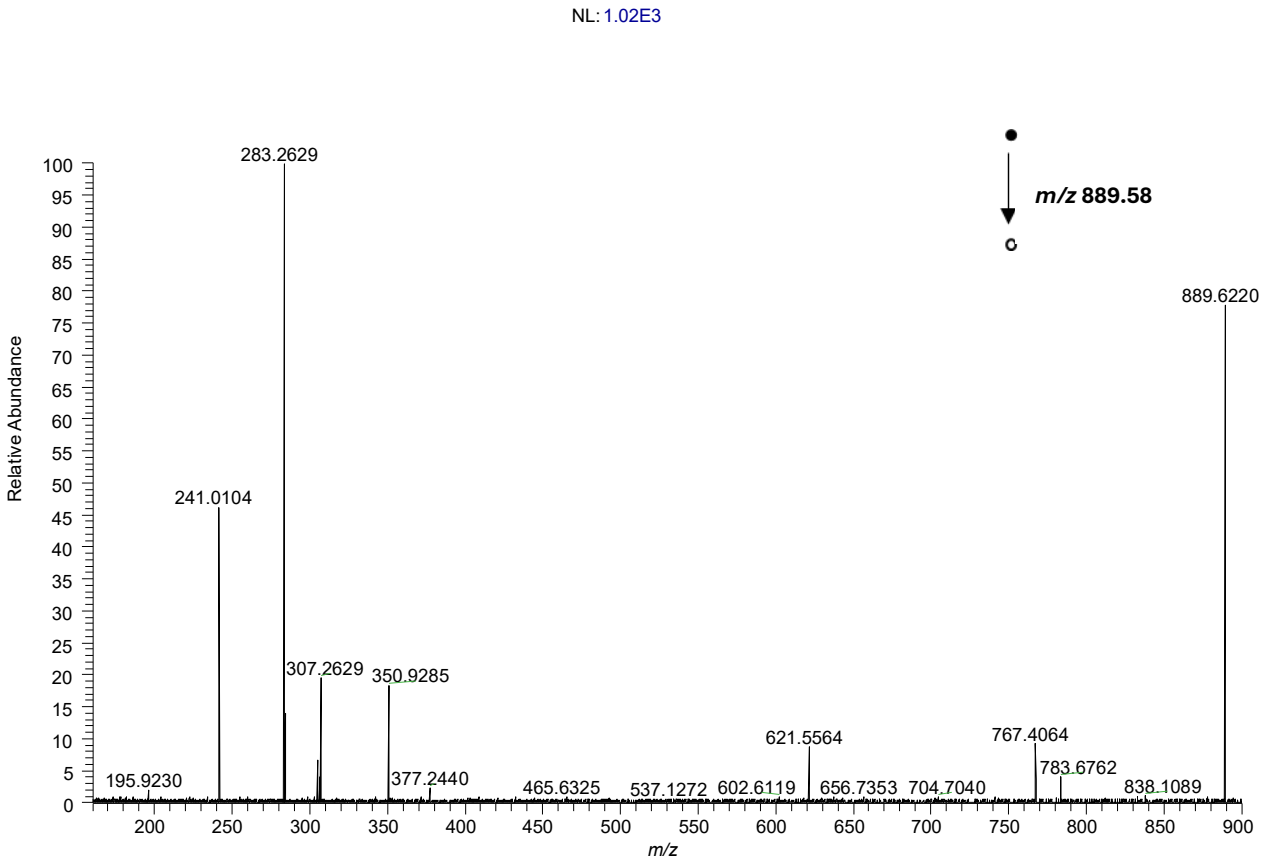


| Product ions (*m/z*) | Exact mass | Species | Formula (-) | Mass error (ppm) |
|---|---|---|---|---|
| 307.2629 | 307.2637 | FA 20:2 | $C_{20}H_{35}O_2$ | -2.60 |
| 283.2629 | 283.2637 | FA 18:0 | $C_{18}H_{35}O_2$ | -2.82 |
| 241.0104 | 241.0113 | IP -$H_2O$ | $C_6H_{10}O_8P$ | -3.73 |

# PI(18:0_22:6)-*m/z* 909.5493 $[M-H]^-$

# $C_{49}H_{82}O_{13}P$

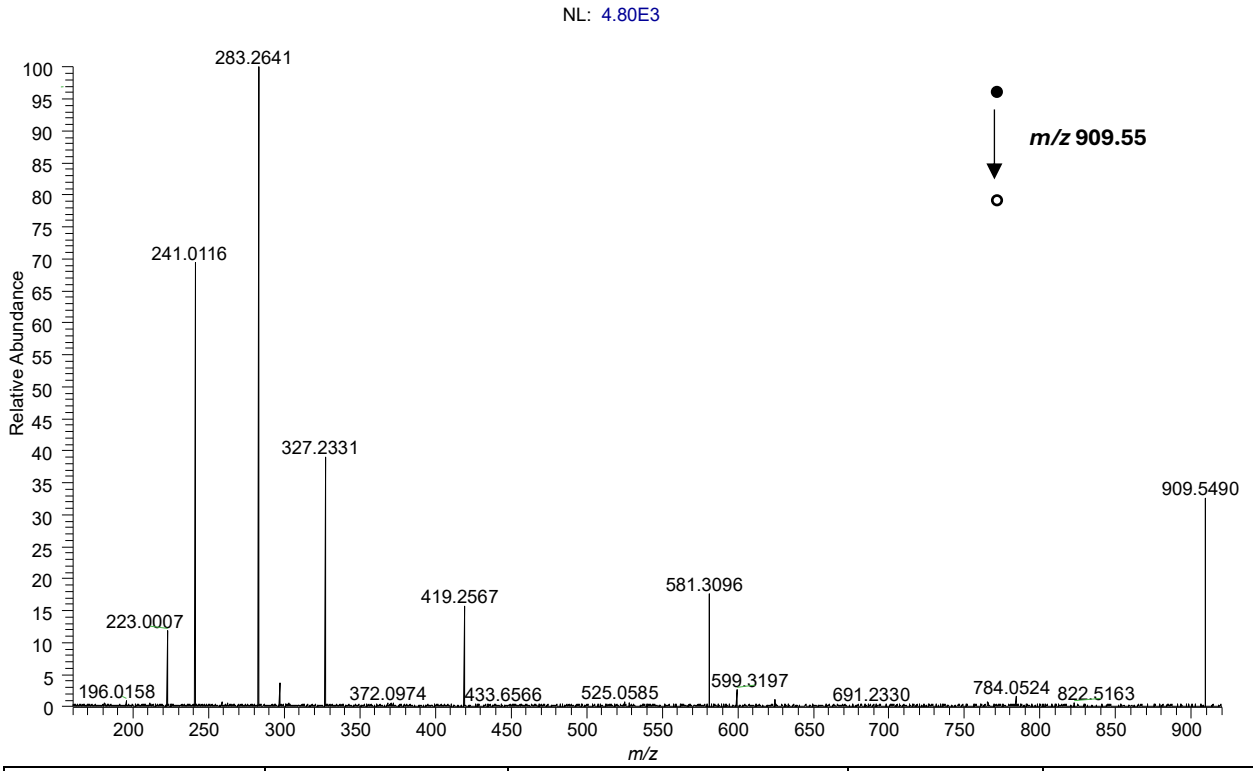


| Product ions (*m/z*) | Exact mass | Species | Formula (-) | Mass error (ppm) |
|---|---|---|---|---|
| 327.2331 | 327.2324 | FA 22:6 | $C_{22}H_{31}O_2$ | 2.14 |
| 283.2641 | 283.2637 | FA 18:0 | $C_{18}H_{35}O_2$ | 1.41 |
| 241.0116 | 241.0113 | IP -$H_2O$ | $C_6H_{10}O_8P$ | 1.24 |
| 581.3096 | 581.3091 | PI 18:0 -$H_2O$ | $C_{27}H_{50}O_{11}P$ | 0.86 |
| 419.2567 | 419.2562 | PA 18:0 -$H_2O$ | $C_{21}H_{40}O_6P$ | 1.19 |

# PI(18:0_22:5)- *m/z* 911.5649 $[M-H]^-$

# $C_{49}H_{84}O_{13}P$

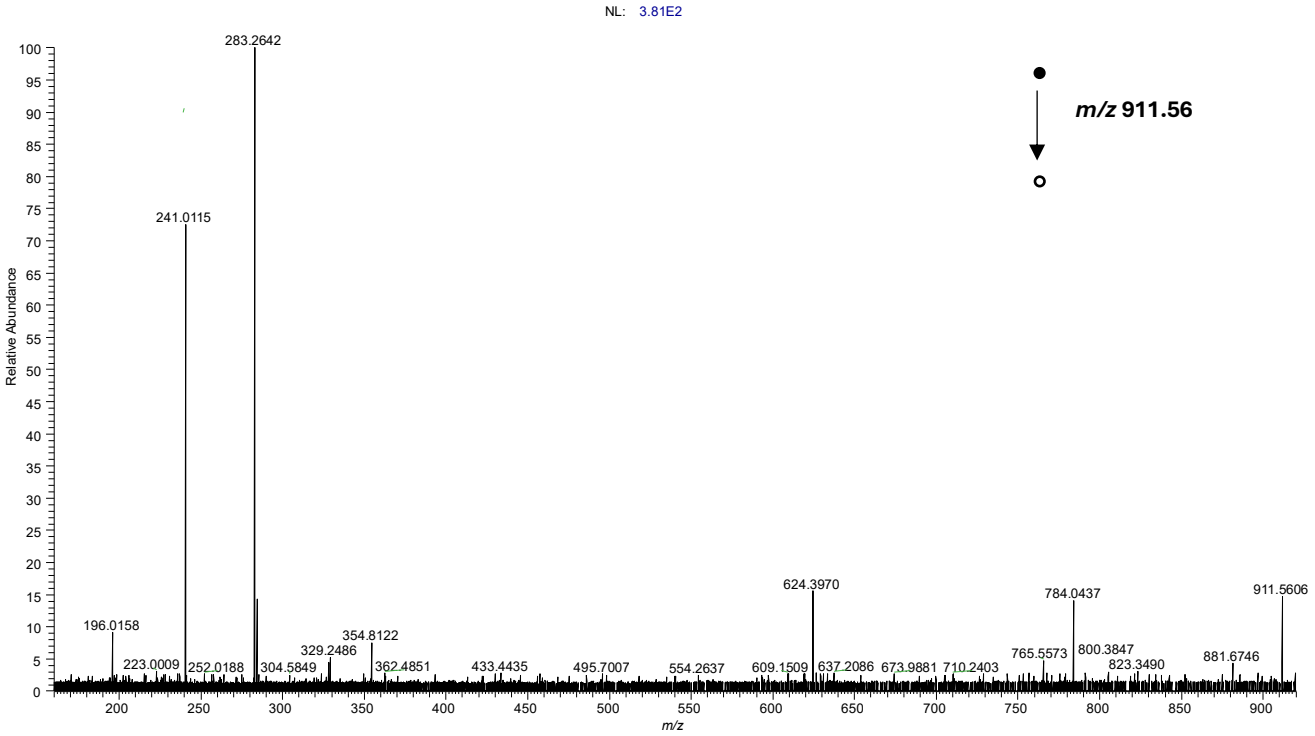


| Product ions (*m/z*) | Exact mass | Species | Formula (-) | Mass error (ppm) |
|---|---|---|---|---|
| 329.2486 | 329.2480 | FA 22:5 | $C_{22}H_{33}O_2$ | 1.82 |
| 283.2642 | 283.2637 | FA 18:0 | $C_{18}H_{35}O_2$ | 1.76 |
| 241.0115 | 241.0113 | IP-$H_2O$ | $C_6H_{10}O_8P$ | 0.83 |

# PI(18:0_22:4)- *m/z* 913.5806 $[M-H]^-$

# $C_{49}H_{86}O_{13}P$

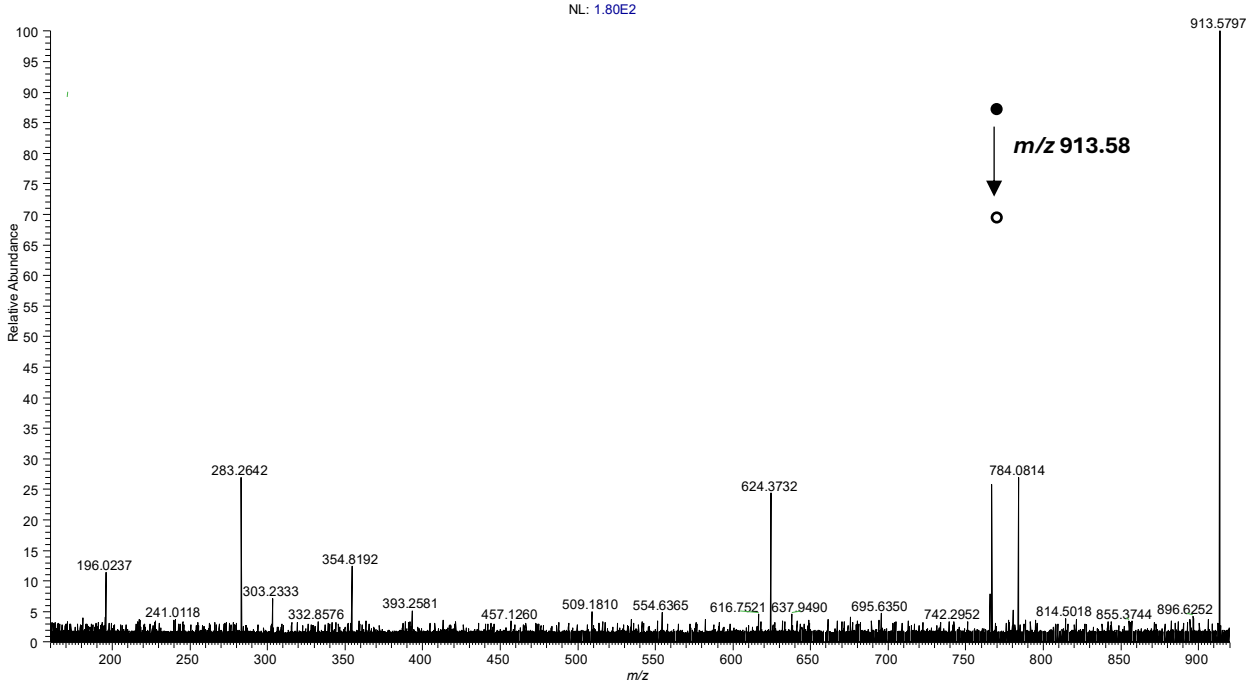


| Product ions (*m/z*) | Exact mass | Species | Formula (-) | Mass error (ppm) |
|---|---|---|---|---|
| 283.2642 | 283.2637 | FA 18:0 | $C_{18}H_{35}O_2$ | 1.76 |
| 241.0118 | 241.0113 | IP -$H_2O$ | $C_6H_{10}O_8P$ | 2.07 |

# PIP(18:0_20:4)- *m/z* 965.5156 $[M-H]^-$

# $C_{47}H_{83}O_{16}P_2$

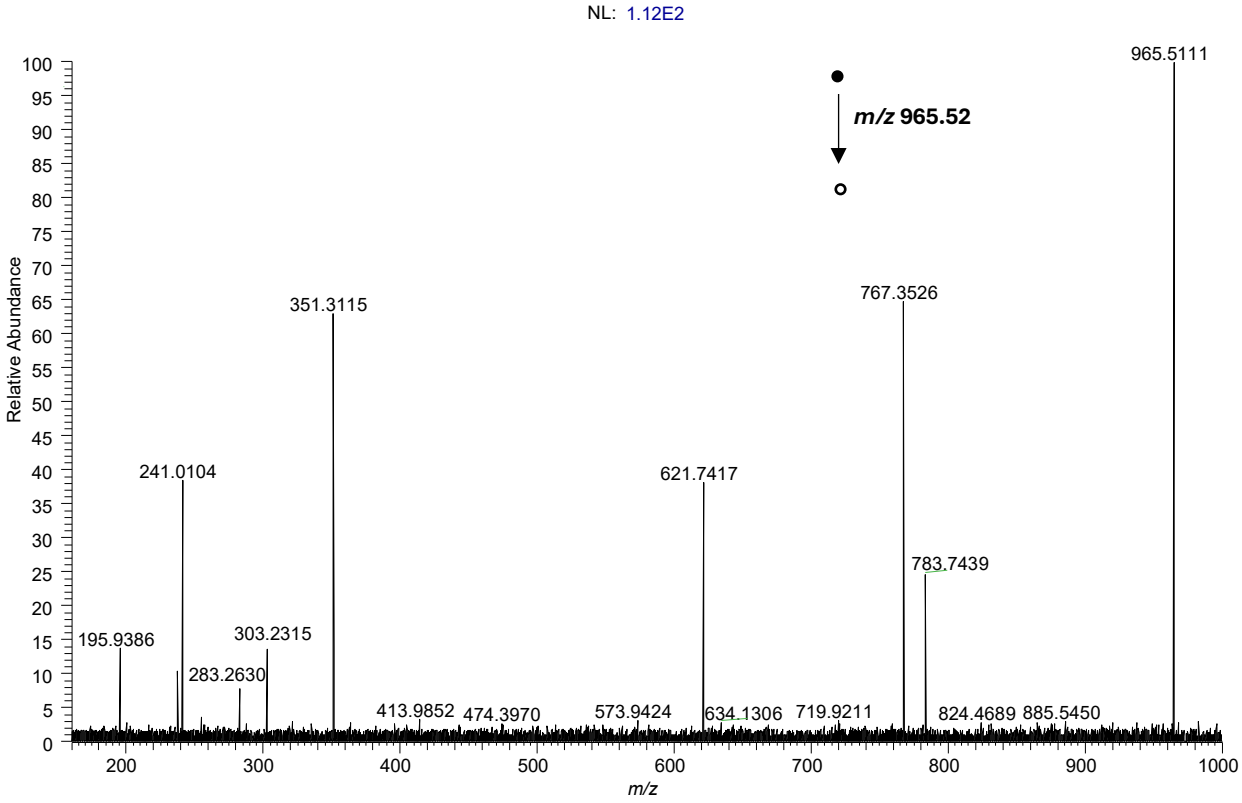


| Product ions (*m/z*) | Exact mass | Species | Formula (-) | Mass error (ppm) |
|---|---|---|---|---|
| 303.2315 | 303.2324 | FA 20:4 | $C_{20}H_{31}O_2$ | -2.96 |
| 283.2630 | 283.2637 | FA 18:0 | $C_{18}H_{35}O_2$ | -2.47 |
| 241.0104 | 241.0113 | IP -$H_2O$ | $C_6H_{10}O_8P$ | -3.73 |

Appendix B. Supplementary materials for Chapter 3.

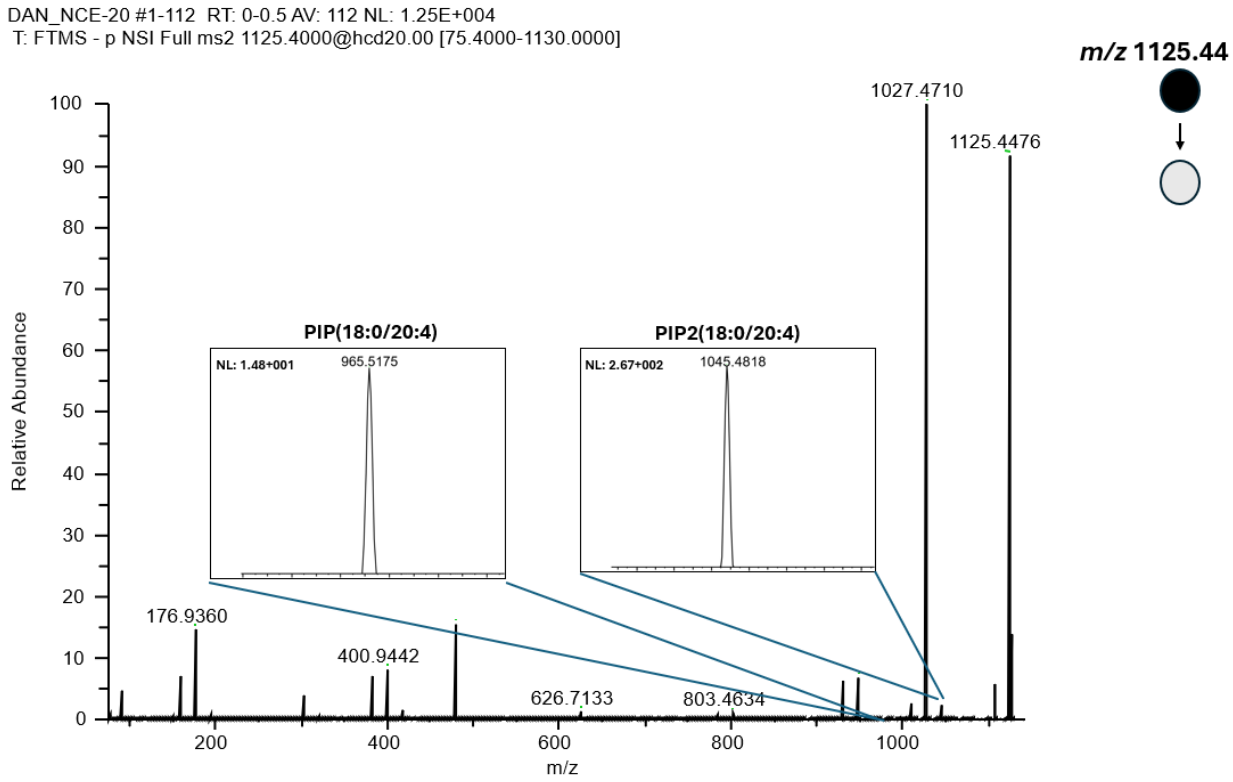


**Figure B.1:** MALDI-MS/MS spectrum of $[PIP3-H]^-$ at NCE 20%, utilizing DAN as the MALDI matrix.